Tóm tắt

Luận án trình bày nghiên cứu chi tiết về hoạt động của detector Cherenkov VATLY, bản sao của một trong 1660 detector mặt đất tại Đài thiên văn Pierre Auger. Đề tài nghiên cứu tập trung vào sự đáp ứng của detector đối với các tín hiệu nhỏ tới một phần mười tín hiệu được tạo ra bởi hạt muon đi xuyên detector theo phương thẳng đứng (VEM), mở rộng vùng hoạt động của detector lên đến 10^4. Nghiên cứu sử dụng phương pháp tìm kiếm thực nghiệm sự phân rã của hạt muon dừng trong khối nước của detector, trong đó chỉ có một vài phần trăm thông lượng hạt là phát ra đủ ánh sáng Cherenkov để có thể được ghi nhận trước khi bị dừng hoàn toàn. Sau đó, mỗi muon phân rã thành một electron (hay positron) có năng lượng trung bình khoảng 35 MeV. Thí nghiệm được thiết kế phù hợp cho việc phát hiện các tín hiệu được tạo ra bởi cả muon dừng và electron được sinh ra. Những cặp tín hiệu như vậy đã được phát hiện trong các điều kiện thí nghiệm khác nhau, cả biên độ tín hiệu lẫn khoảng thời gian giữa hai tín hiệu cùng được xác định. Một hodoscope nhấp nháy được đặt trên và dưới detector Cherenkov để chuẩn thang đo cho hệ thống. Một số lượng lớn mẫu số liệu đã được thu thập cho thấy bằng chứng rất rõ ràng về sự phân rã muon với phổ thời gian như đã dự kiến. Biên độ tín hiệu của hạt electron được thấy chỉ bằng một phần của một VEM , và chỉ phần đuôi phổ phân bố là được ghi nhận. Phân bố của muon đòi hỏi phải có thêm sự đóng góp của thành phần mềm electron/photon, xuất hiện đặc biệt quan trọng trong thí nghiệm này do detector Cherenkov có thể tích ghi đo lớn. Một mô hình để tìm hiểu về cơ chế vật lý và tiến trình ghi nhận đã được xây dựng giải thích rõ ràng phổ phân bố điện tích và thời gian đã thu được. Nó cũng cho phép đánh giá số quang điện tử trên một VEM là 13,0 ± 0,9 và năng lượng trung bình của muon là 4,0 ± 0,4 GeV. Hiệu suất ghi nhận hạt electron ngụ ý một kích thước mưa rào electron hiệu dụng là ~36 ± 6 cm, bằng kích thước của chiều dài bức xạ trong môi trường nước. Điểm cuối của phổ phân bố điện tích electron, tương ứng với động năng 53 MeV, được đo là E_{end} = 0,275 ± 0,018 VEM phù hợp với dự kiến. Tốc độ sự kiện được đo phù hợp với dự kiến. Tốc độ xuất hiện sự kiện muon kép trong cùng một mưa rào là 7,0 ± 0,5 Hz. Một chương trình mô phỏng cơ chế thu nhận ánh sáng đã được

viết thể hiện sự phụ thuộc của các góc tới nhỏ vào hiệu suất ghi nhận, điều này phù hợp với quan sát. Ngoài ra, nghiên cứu này đã đóng góp những thông tin hữu ích về các hoạt động chi tiết của những detector Cherenkov lớn nói chung, và của mảng detector mặt đất tại Đài thiên văn Pierre nói riêng. Nghiên cứu đã góp phần vào việc đào tạo sinh viên ngành vật lí hạt thực nghiệm và vật lí hạt nhân bằng cách cung cấp cho họ một công cụ đặc biệt thích hợp với công việc.

Abstract

A detailed study of the performance of the VATLY Cherenkov detector, a replica of one of the 1660 detectors of the ground array of the Pierre Auger Observatory, is presented. The emphasis is on the response to low signals down to a tenth of the signal produced by a vertical feed-through muon (VEM), implying a dynamical range in excess of 10^4. The method is to look for decays of muons stopping in the water volume of the detector, of which only a few produce sufficient Cherenkov light to be detected before stopping. The subsequent muon decay produces an electron (or positron) that carries an average energy of only ~35 MeV. The experimental set-up detects the signals produced by both the stopping muon and the decay electron. Such pairs have been detected under various experimental conditions and the amplitude of the electron signal has been recorded together with the time separating the two signals. A scintillator hodoscope that brackets the Cherenkov detector from above and below provides a precise calibration. A large sample of data has been collected that give very clear evidence for muon decays with the expected time dependence. The amplitude of the electron signal is observed at the level of a fraction of a VEM, and only the upper part of its distribution can be detected. The muon distribution requires the additional contribution of a soft electron/photon component, which appears particularly important in the present experimental set-up due to the large sensitive volume of the Cherenkov detector. A model of the physics mechanism at play and of the detection process has been constructed, giving good descriptions of the measured charge and time distributions. This allows for obtaining useful evaluations of the number of photoelectrons per VEM, 13.0±0.9, and of the mean muon energy, 4.0 ±0.4 GeV. The detection efficiency of electrons implies an effective electron shower size, ~36±6 cm, at the scale of the radiation length in water. The end point of the electron charge distribution, corresponding to a kinetic energy of 53 MeV, is measured to be E_{end}=0.275±0.018 VEM in agreement with expectation. The measured event rates are found in good agreement with predictions and the occurrence of muon pairs from a same shower is measured with a rate of 7.0±0.5 Hz. A simulation of

the light collection mechanism suggests the presence of a small zenith angle dependence of its efficiency, which is found consistent with observation. At the same time as this study contributes useful information to the detailed performance of large Cherenkov detectors in general, and particularly of the ground array of the Pierre Auger Observatory, it contributes to the training of students of experimental particle and nuclear physics by making available to them a tool particularly well suited to the task.

Acknowledgements

My deep gratitude goes first to Prof. Pierre Darriulat, supervisor of this thesis, for countless discussions, enormous help during my doctoral studies and continuous support. Without him this work would not have been possible.

I would like to thank Dr. Dang Quang Thieu for guidance and assistance with the hardware. I also thank my colleagues, Dr. Pham Ngoc Diep, Dr. Pham Thi Tuyet Nhung and Dr. Pham Ngoc Dong for their friendly collaboration.

The work accomplished by the Auger Collaboration inspired the studies presented here: much of my work owes a lot to their experience. I express my deep gratitude to our colleagues in the Pierre Auger Collaboration and to the friends of VATLY for their constant interest and support.

I thank INST/VAEI, IOP, NAFOSTED, the French CNRS, the Rencontres du Vietnam, the Odon Vallet fellowships and the World Laboratory for financial support.

This thesis is dedicated to my family – Nguyễn Văn Trương, Bùi Thị Sửu, Nguyễn Thành Dương, Bùi Thị Thái, Nguyễn Khánh Huyền and Nguyễn Thanh Hà.

Table of content

1. Introduction

1.1 Generalities on cosmic rays

Cosmic rays [1] are ionised nuclei that travel in space up to extremely high energies of the order of 10^{20} eV=16 Joules. There are very few of them but their contribution to the energy density of the Universe is similar to that of the Cosmic Microwave Background or of the visible light or of the magnetic fields, namely ~1 eV/cm^3. Their power law energy spectrum (Figure 1.1), spanning 32 decades (12 decades in energy), is of the approximate form $E^{-2.7}$.

The Pierre Auger Observatory (PAO) [2] studies the high energy part of the spectrum, where an extragalactic component can be found. The water Cherenkov detector of the Vietnam Auger Training LaboratorY (VATLY), which is being studied in the present thesis, is a replica of those used in the PAO. Indeed VATLY is associated with the PAO and much of its research is related to PAO data. However, the present study uses data collected in Hanoi, at sea level, which correspond to the low energy part of the spectrum. Its main aim is to study the detector, its properties and its response to various sources, in particular to low signals.

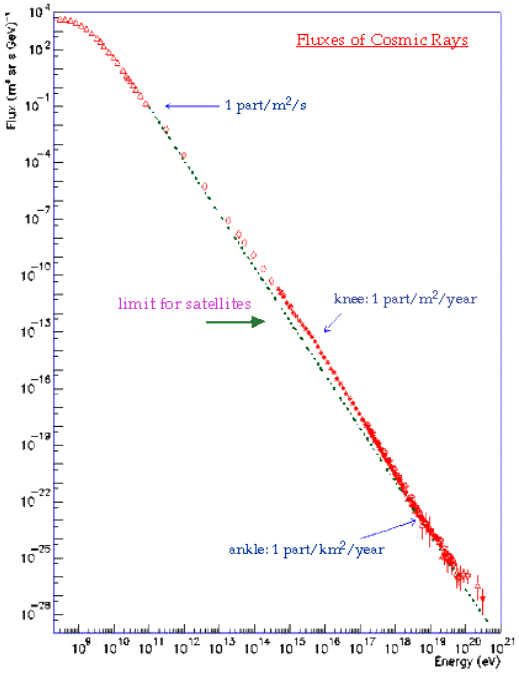

Figure 1.1 The cosmic ray energy spectrum displaying its main features.

Because of the close relation between VATLY and the PAO, we devote the next sub-section (1.2) to a brief description of the PAO and of the physics questions that it addresses. The main characteristics of low energy cosmic rays, as used here, are briefly reviewed in sub-section 1.3 and the water Cherenkov detectors used in both VATLY and the PAO are described in sub-section 1.4. Sub-section 1.5 introduces the present work.

At lower energies, cosmic rays are found to be ionised nuclei with relative abundances similar to those measured on average in the Universe: protons dominate, followed by helium nuclei and by a spectrum of strongly bound light nuclei, mostly iron. Spallation reactions occurring in the interactions of cosmic rays with interstellar matter tend to fill the valleys of the original spectrum.

Most of the lower energy cosmic rays are galactic and have their sources in the shells of young Super Nova Remnants (SNR) in the Milky Way, the acceleration mechanism being well described by diffusive shock acceleration across the shock front [3]. This is a collisionless process, with magnetic fields causing the random walk progression of the particle being accelerated, implying many successive traversals of the shock front. Each shock traversal increases the particle energy by a constant fraction, proportional to the relative velocity of the upstream medium with respect to the downstream one. Turbulences around the shock result in strong magnetic field amplification increasing significantly the efficiency of the acceleration process. Diffusive shock acceleration has the property to generate a power energy spectrum with an index between 2 and 3.

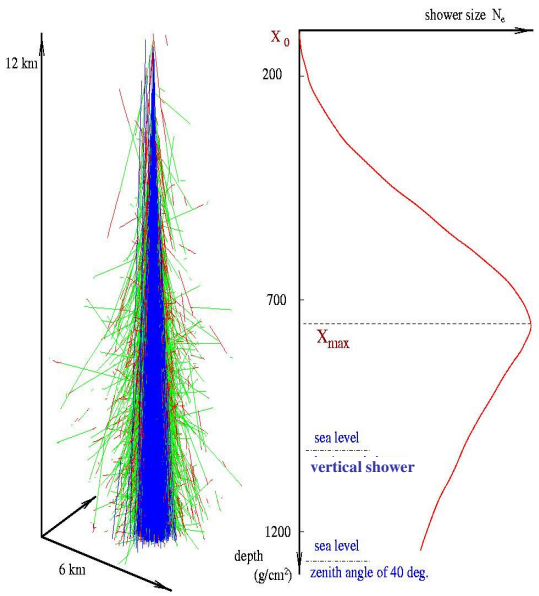

Figure 1.2 Development of an extensive air shower in the atmosphere.

When a primary cosmic ray enters the Earth atmosphere, it interacts with it and produces a large number of mesons, which, in turn, interact with the atmosphere, and so on until the primary energy is exhausted in ionisation losses. The result is a cascade of interactions (Figure 1.2) producing an extensive air shower (EAS). Its longitudinal profile evolves slowly with energy, in proportion to its logarithm, while its energy content, in the form of ionisation losses, is proportional to energy.

A major fraction of the mesons produced are pions, either neutral or charged. The former decay promptly into two photons and are therefore lost for

the development of the hadronic cascade. They generate instead electromagnetic showers consisting mostly of electrons, positrons and photons, developing longitudinally at the scale of a radiation length, twice as short as the interaction length which governs the development of the hadronic cascade. The charged pions have a chance to decay into a muon-neutrino pair if their decay length, 56 m/GeV, is short enough in comparison with the interaction length. As a result, the muon to electron/photon ratio increases with depth.

Indeed, at sea level, most cosmic rays are muons with momenta in the few GeV/c range. Their rate is of the order of $1/cm^2/mn$ and depends on latitude. The reason is the shielding action of the geomagnetic field: when a low momentum cosmic ray aims at the Earth, it will be bent out by this field and will not reach the atmosphere. These results in a momentum cut-off called rigidity cut-off. It is of the order of 4 GeV/c in Europe and Northern America. If the geomagnetic field were a perfect south-north dipole, it would be zero at the poles and maximal at the equator. In fact it is maximal in a region that covers from Sri Lanka to Vietnam, where it reaches 17 GeV/c. Near the poles, it is indeed very low and allows solar wind particles to enter the atmosphere, causing auroras. The geomagnetic field has only little effect on the secondary shower particles: it acts on the primary cosmic ray. On ground, it affects mostly the cosmic ray flux, not much the energy spectrum.

1.2 The Pierre Auger Observatory

The Pierre Auger Observatory (PAO) is a hybrid detector covering $3'000\ km^2$ in the Argentinean Pampas where showers are detected from the fluorescence they produce in the atmosphere and by their impact on a ground detector array (Figure 1.3). Construction of the baseline design was completed in June 2008. With stable data taking starting in January 2004, the world's largest data set of cosmic ray observations had been already collected during the construction phase of the Observatory.

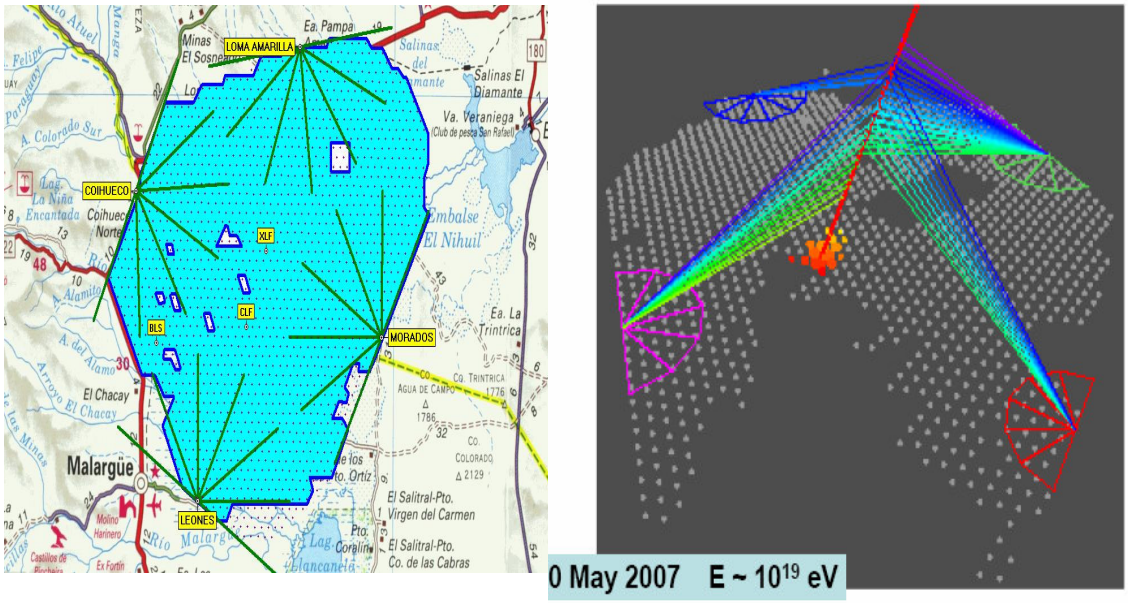

Figure 1.3 Left: Plan view of the PAO, covering some 60×50 km^2. SD tanks are shown as dots and the lines of sight of the 24 FD telescopes as green lines.
Right: The first four-fold hybrid event (when the array was not yet complete).

Around 30 EeV, the UHECR flux is about 0.2 km^{-2}century^{-1}sr^{-1}EeV^{-1} and drops rapidly at higher energies, requiring a very large coverage; but the showers contain billions of particles when reaching ground and cover several square kilometres, allowing for a thin sampling. Only 5 ppm of the PAO area are covered by detectors. These include 1'660 Cherenkov detectors making up the surface detector (SD, Figure 1.4), and 24 fluorescence telescopes making up the fluorescence detector (FD, Figure 1.5). Data are transferred by radio to an acquisition centre which filters them and sends them out for subsequent dispatching to the laboratories associated with this research, including VATLY in Ha Noi.

The SD samples the footprint of the showers on ground. It is made of a triangular array of water Cherenkov counters having a mesh size of 1.5 km located on flat ground at an altitude of 1'400 metres above sea level. The VATLY Cherenkov detector is a replica of one of these.

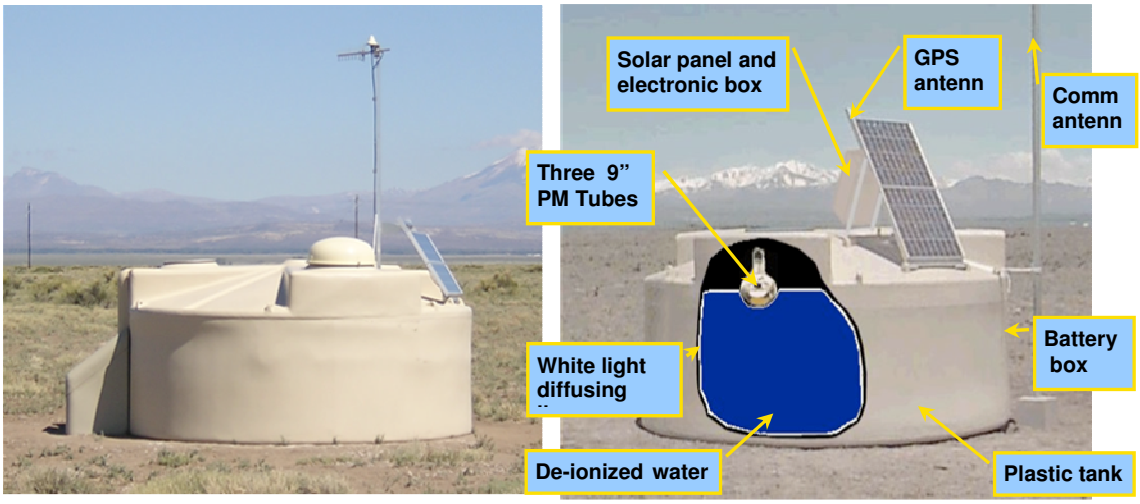

Figure 1.4 Picture of a Cherenkov tank on site (left panel) and exploded view (right panel).

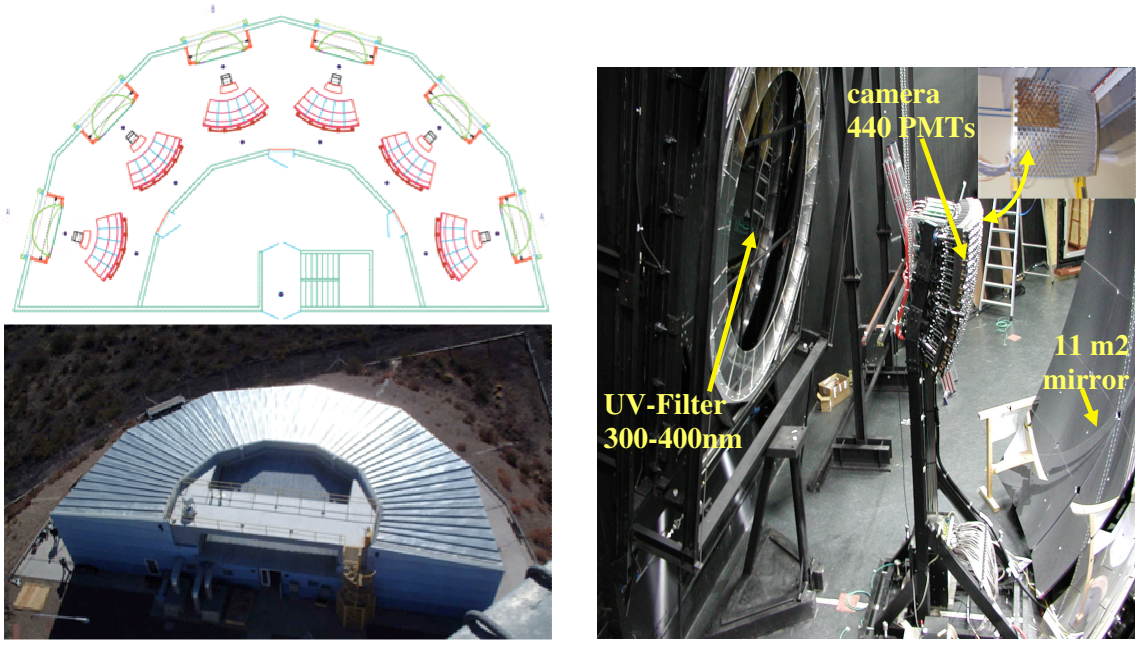

Figure 1.5 Left: A fluorescence station: schematic view (above) and its photograph (below). Right: Photograph of an eye.

When reaching ground, showers consist essentially of low energy electrons, positrons and photons as well as of muons having a kinetic energy of a few GeV. When shower particles are detected in at least three detectors, the measurement of the time at which they are hit allows for a precise measurement of the azimuth and zenith angle of the shower axis (accounting for the slight curvature of the shower front). The energy measurement implies the construction

of a standard function, called lateral distribution function (LDF), which gives the average signal measured in a Cherenkov detector as a function of shower energy, distance to the shower axis and zenith angle. The energy is essentially obtained from the normalization of the measured signals to the standard LDF. The final energy scale is calibrated using FD data in hybrid events as illustrated in Figure 1.6. Figure 1.7 summarizes the information gathered by the SD, showing both the footprint of the shower on ground and the fit to the LDF.

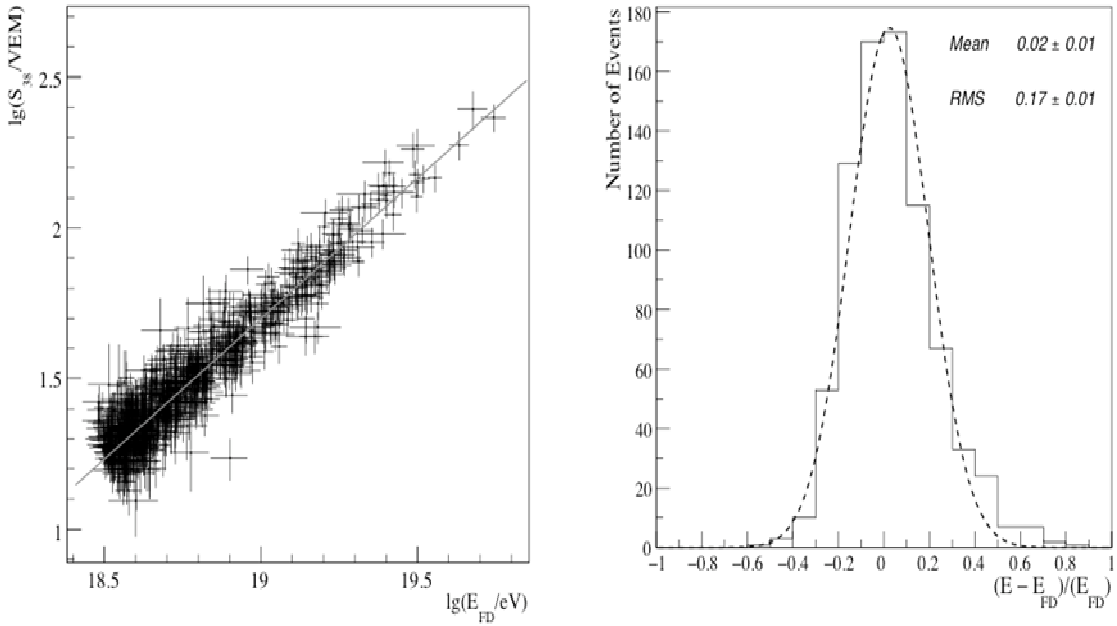

Figure 1.6 Hybrid events. Left: Correlation between the decimal logarithms of the energy measured in the FD (abscissa) and in the SD (ordinate). Right: Fractional difference between the FD and SD energies, E_{FD} and E.

Three major questions are being addressed by the PAO: Which is the energy distribution of UHECRs? Where do they come from? Which is their nature?

The PAO has already given two particularly important answers to these questions. One is the evidence for the so-called GZK cut-off [4], the other is the observation of a correlation between the direction of arrival of the highest energy UHECRs and nearby galaxies.

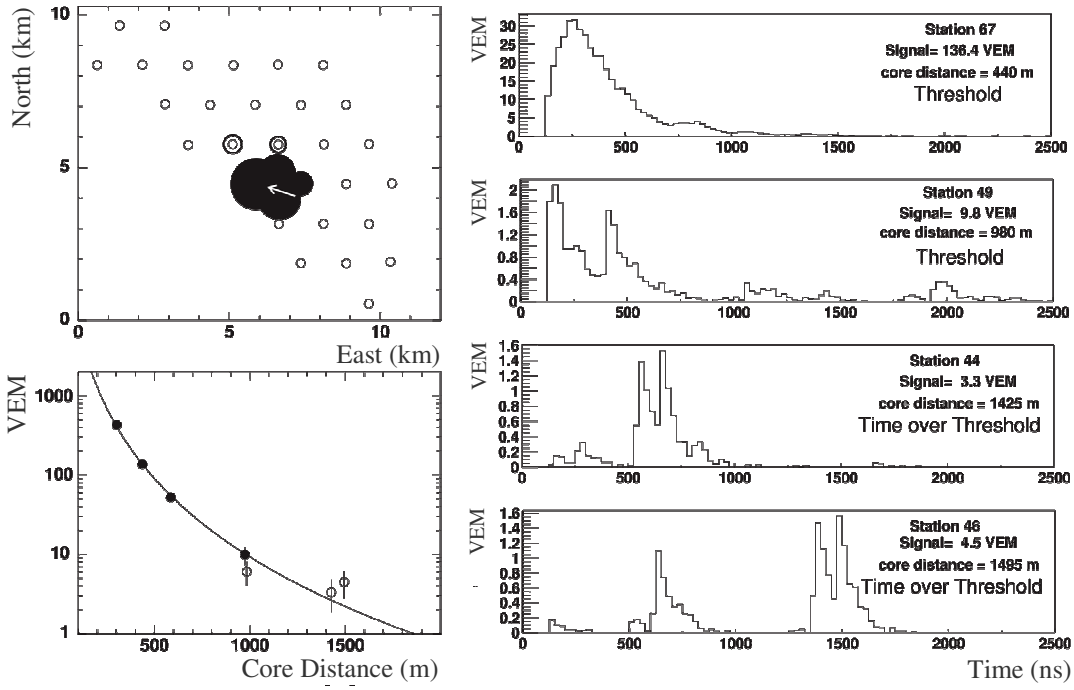

Figure 1.7 SD data of a typical event of about $5x10^{18}$ eV. Top left: Top view of triggered tanks. Lower left: LDF fit. Right: FADC traces from four detectors.

The Greisen-Zatsepin-Kuzmin (GZK) cut-off results from the interactions of cosmic rays with the cosmic microwave background (CMB), producing either electron-positron pairs or new mesons. Of these, the pion photoproduction threshold is of particular importance. Until recently, the existence of such a cut-off was uncertain but the Pierre Auger Observatory has given clear evidence for it (Figure 1.8). With a typical interaction length in the few 10 Mpc scale, cosmic rays coming from larger distances cannot make it to the Earth without interacting, and therefore loose energy: their flux is significantly damped and only nearby (<100 Mpc) sources can contribute to the UHECR spectrum.

The large UHECR statistics accessible to the PAO has revealed a correlation with extragalactic counterparts. Of relevance to this study is the fact that the nearby universe, in which detected UHECRs are confined by the GZK cut-off, is highly inhomogeneous. Selecting UHECR having an energy in excess of 6×10^{19} eV and comparing the direction in the sky where they come from with a catalogue of nearby (< 75 Mpc) galaxies, reveals a positive, but relatively weak correlation.

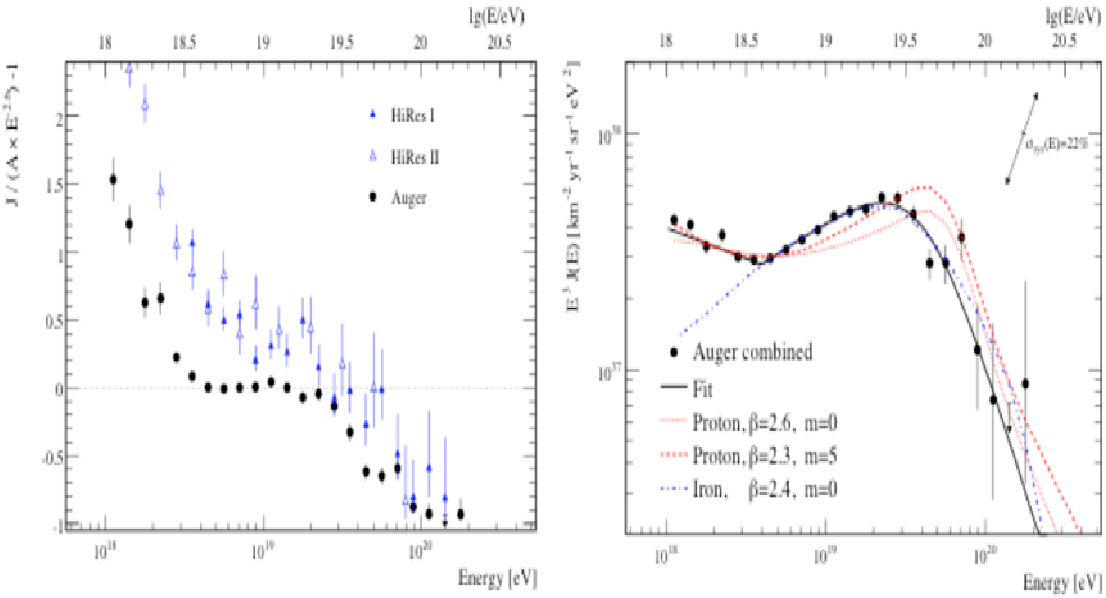

Figure 1.8 Left: Fractional difference between the combined energy spectrum of the PAO and a spectrum with an index of 2.6. Data from HiRes are shown for comparison. Right: Combined energy spectrum compared with several astrophysical models including a pure composition of protons (red lines) or iron (blue line).

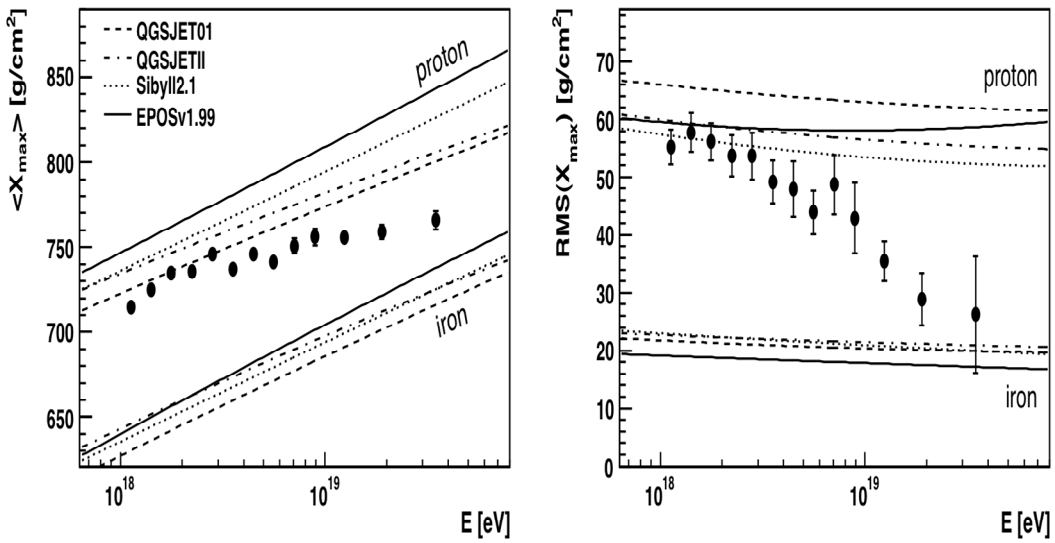

Figure 1.9 Energy dependence of $<X_{max}>$ and $Rms(X_{max})$ compared with the predictions of air shower simulations using different hadronic interaction models.

Of relevance to this result is the fact that, at the highest energies, the nature of the primaries drifts from light (mostly protons) to heavy (mostly Fe) nuclei [5], the latter being too strongly bent in the interstellar magnetic fields for the showers that they produce to point back to their sources. The main difference between showers induced by protons and by iron nuclei results from the very

different natures of their first interaction in the upper atmosphere. The proton shower starts to develop on average after having crossed one interaction length and the depth of its starting point fluctuates with a variance also equal to one interaction length. The iron shower may be seen as the superposition of 56 proton showers (protons and neutrons are equivalent at such energies), each carrying 1/56 of the nucleus energy. As a result it starts much earlier, and the location of its starting point fluctuates much less than in the proton case [6]. This is indeed what is observed from the FD measurement of the shower longitudinal profiles (Figure 1.9). Yet, the mass composition of UHECR primaries remains an open question requiring more data to be collected.

1.3 Cosmic rays in Hanoi

Hanoi is located 12 m above sea level at 21^{o} latitude N and 106^{o} longitude E where the geomagnetic rigidity cut-off reaches its world maximal value of ~17 GV. The cosmic ray flux has been measured at VATLY between 2001 and 2003 using scintillator detectors. Three successive measurements have been done: first of the vertical cosmic muon flux [7], second of the zenith angle distribution [8] and third of the east-west asymmetry [9]. We recall the main results in the present sub-section.

At sea level, the cosmic ray flux of charged particles is dominated by muons having a steep momentum spectrum with an average momentum of the order of 4 GeV/c; the main contamination is a ~3% proton component and very soft electrons and positrons. Neutral particles include slow neutrons and soft photons.

The vertical muon flux at zero zenith angle and integrated over all momenta was measured to be 71.5±2.8 $m^{-2}sr^{-1}s^{-1}$ in good agreement with a model description of the muon flux over the whole planet [10]. The data were taken during a period of low Sun activity; as we are now at maximal activity, fluxes lower by a few percent might be expected.

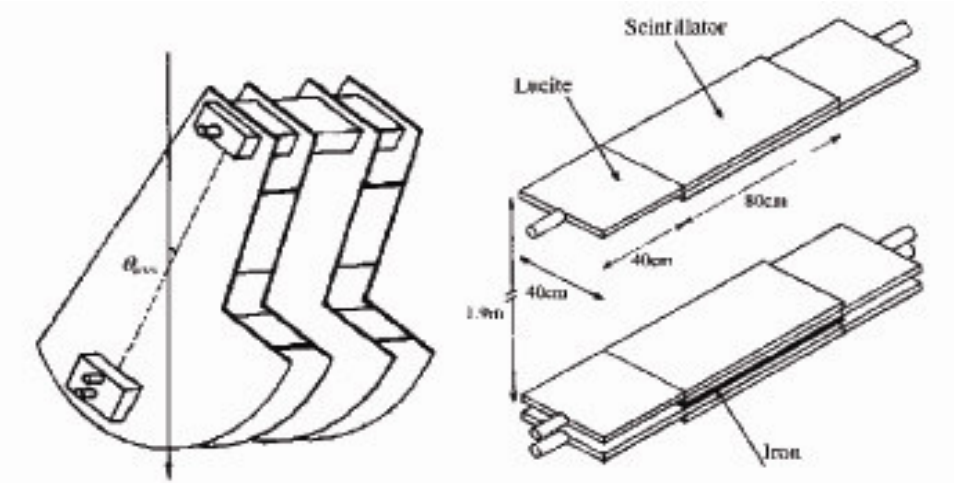

Figure 1.10 Schematic view of the telescope used in Hanoi to measure the angular dependence of the cosmic ray flux [8, 9].

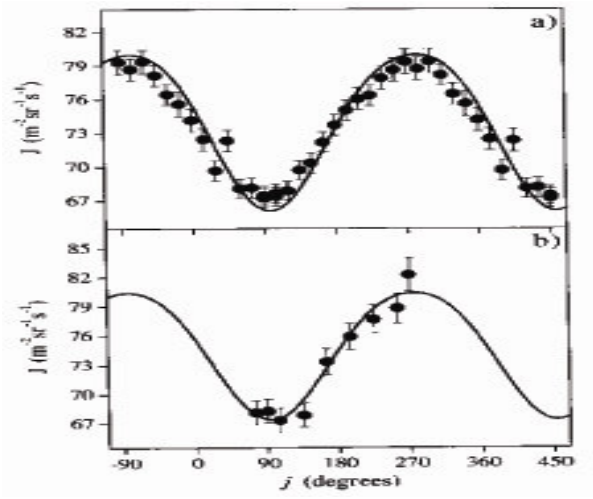

Figure 1.11 East-west asymmetry measured in Hanoi [9] at $\theta = 50^{o}$ (upper pannel) and $\theta = 65^{o}$ (lower pannel).

The zenith angle (θ) distribution of the flux is well described by a form $(\Phi_0 - a\sin^2\theta)\cos^2\theta$ with $\Phi_0 = 72.0 \pm 1.6$ $m^{-2}sr^{-1}s^{-1}$ and $a = 7.8 \pm 0.8$ $m^{-2}sr^{-1}s^{-1}$ again in excellent agreement with the model of Reference 10. As primary cosmic rays and atmospheric nuclei are both positively charged, a charge asymmetry exists among the constituents of atmospheric cosmic showers and therefore among the muons into which they may decay. The magnetic field being oriented toward south, it bends positive primary particles eastward, resulting in an east-west asymmetry of the flux that has been measured as a function of zenith angle using the telescope shown in Figure 1.10. The amplitude of the asymmetry is

measured to increase from zero at θ=0^o to nearly 20% at θ=60^o. The resulting azimuthal oscillations are displayed in Figure 1.11 for θ=50^o and θ=65^o respectively.

1.4 The VATLY Cherenkov detectors

A set of four Cherenkov detectors is installed on the roof of the VATLY Laboratory. Their design and performance have been described in detail in Reference 11. One of these, referred to as the main tank in the present work, is a replica of a standard PAO tank (of which 1'660 are operated in the PAO array in Argentina). As it is central to the present work, we briefly recall the main results that have been previously obtained.

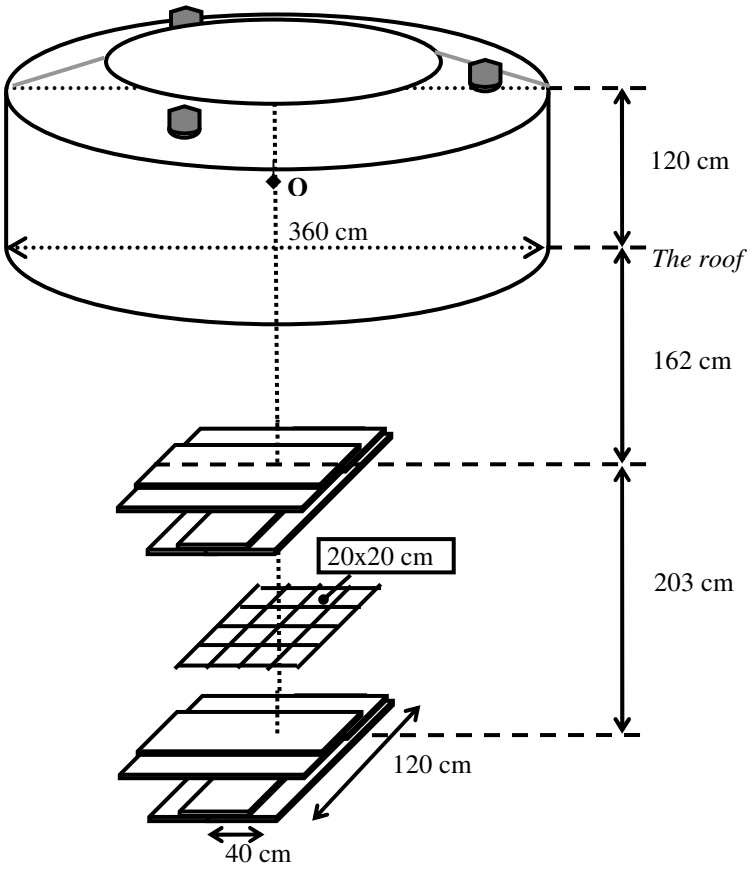

Figure 1.12 Geometry used for the study of the main tank response as a function of incidence angle [13].

The main tank has been constructed in Hanoi with the same geometry as that of the PAO tanks [12]: a cylinder of 3.6 m diameter (about 10 m^2 in area)

filled with clean water up to 1.2 m height. At variance with the PAO tank, which is made of resin, the VATLY tank is made of stainless steel. The water volume is seen by three down-looking PMTs at 120^{o} azimuthal intervals on a radius of 1.25 m. In a first phase, the tank was equipped with old 8" diameter PMTs (EMI D 340A), the inner walls were simply painted white and a rudimentary sand based filter was used to purify city water. Early studies [13] using a fragmented hodoscope trigger (Figure 1.12) have given evidence for a good proportionality of the response to track length, but the number of photo-electrons per Vertical Equivalent Muon (VEM) was ~10 times smaller than in the PAO [13]. The main tank was completely refurbished in 2006 [14] by replacing the old PMTs by new 9" PMTs from the PAO (Photonis XP 1805) and by coating the internal walls with aluminized mylar. An early attempt to use a Tyvek liner, as is done in the PAO, failed because the water was not sufficiently filtered and iron oxide deposited on the bottom of the liner and could not be washed away without damaging it. As a consequence, the VATLY PMTs are directly in contact with water, at variance with the PAO design where they see the water volume through a transparent window of the liner. The refurbishing operation included a complete redesign of the filtering station, with a maximal grain size of 1 μm compared with 10 μm in the first phase; its performance is satisfactory and the water quality is stable, although significantly inferior to that of the PAO. As shown in the next section (2.4.3) the number of photo-electrons per VEM is now ~2.3 times less than in the PAO, a factor more than 4 times larger than in the first phase. Photographs of the VATLY Cherenkov detectors are shown in Figure 1.13 and a plan view of the installation in Figure 1.14.

The front end preamplification of the PMT signals and the HV supplies and dividers use the same electronics as in the PAO but the data acquisition system differs: it is based on the NIM standard for the fast trigger logic and on CAMAC for data recording, with simple Analogue-to-digital (ADC) and Time-to-digital (TDC) converters rather than Flash ADCs as used in the PAO. The PMT signals are fed to the electronics via 20 m 50 Ω coaxial cables through a hole in the roof rather than being dispatched by radio as in the PAO.

Figure 1.13 Left: The main Cherenkov detector is seen surrounded by two of the three smaller ones, one of which is hidden behind the green tower. Right: Addition of a scintillator hodoscope to the main Cherenkov detector; the lower part of the hodoscope is located in the counting room below the roof.

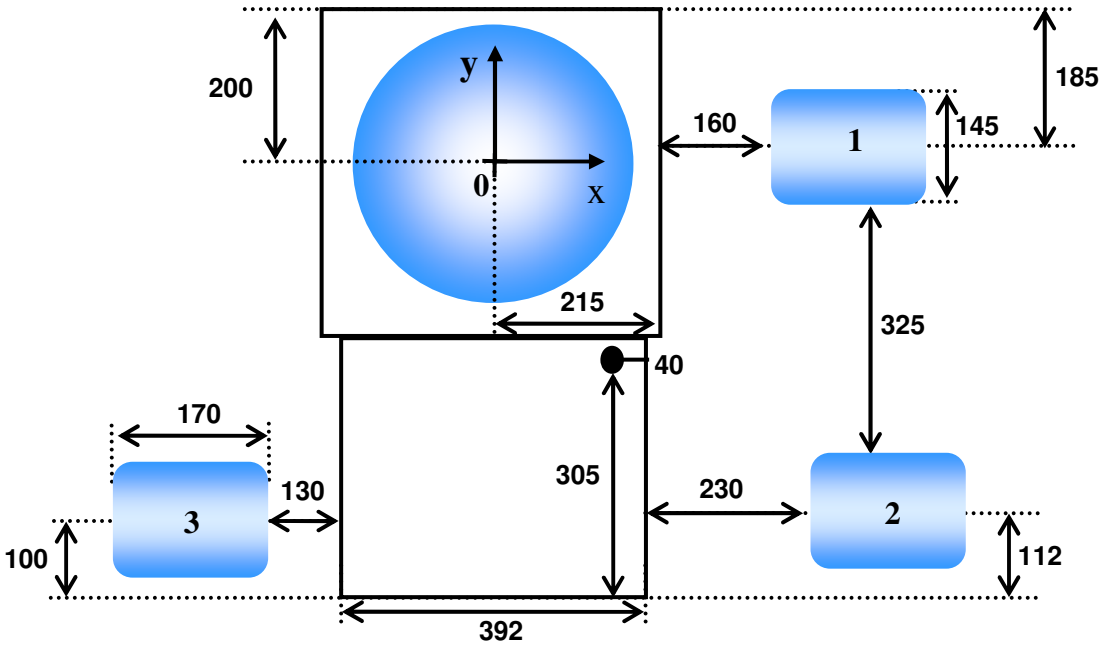

Figure 1.14 Plan view of the VATLY Cherenkov counters including three small (3'000 l) tanks used as a trigger and the large (12'000 l) main tank. All distances are measured in centimeters.

Three satellite tanks have been used to provide an unbiased trigger for the study of the main tank. They give a coincidence rate of 0.1 Hz with an effective acceptance of 22 m^2. The trigger selects vertical showers over an effective solid angle of the order of 0.4 sr. Such showers have energies in the 200 GeV range and a few permil probability of surviving at sea level with sufficient energy

density to be detected. Their cores have typical particle densities of 2.5 to 3 m^{-2} and typical radii of 2 m.

1.5 Overview of the present work

The present thesis reports a number of measurements that have been performed with the aim of gaining detailed information on the performance of the main VATLY tank and learning about important features of the surface detectors of the PAO concerning their response to low signals.

Section 2 reports on the response of the VATLY Cherenkov detector to feed-through muons. We have assembled for this purpose a trigger scintillation hodoscope, the design and performance of which are described in some detail. The analysis of the Cherenkov data includes the selection of a clean sample of relativistic feed-through muons and provides a calibration of the charge scale of the detector in terms of Vertical Equivalent Muons (VEM).

Section 3 is an introduction to the problem of detecting electrons from the decay of muons stopping in the water volume. The interest of this measurement is to test the performance of the main tank in the region of low amplitude signals, as electron signals are expected to be typically an order of magnitude smaller than feed-through muon signals. A simulation of the decay and detection processes allows for a general understanding of the problem and for estimates of the rates and amplitudes that can be expected.

Section 4 is an introduction to the measurement of auto-correlation distributions. Such distributions are one of the basic tools used in the present work to disentangle a possible decay electron signal from a possible multimuon signal (when two muons, from a same or different showers, are detected in the main tank). An analytical description of the distribution is worked out and a numerical simulation is presented that shows the separate effects of multimuons and decay electrons, at the same time providing guidance on how to disentangle them from real data.

Section 5 describes the experimental set-up being used for auto-correlation measurements, including a sophisticated electronics arrangement allowing to deal with high single rates, namely with low signal thresholds as required for electron detection. The auto-correlation distribution proper and the charge measurement are both described in some detail, together with comments on their performance.

Section 6 is dedicated to the analysis of the data that have been collected in several experimental conditions, including both auto-correlation and charge distributions. The results are described and interpreted in Section 7. Section 8 summarizes the main findings and concludes.

2. Response of the VATLY Cherenkov detector to feed-through muons

In order to obtain a calibration of the response of the VATLY Cherenkov detector, we use as reference vertical feed-through muons impacting in the central part of the tank. The same reference is used by the Pierre Auger Observatory (PAO): one speaks of Vertical Equivalent Muons (VEM) which are taken as charge units in all PAO measurements [15]. As atmospheric muons have momenta of the order of 4 GeV/c, most of them are relativistic (the muon mass being only 106 MeV/c^2) and therefore minimum ionizing: in their vast majority, they deposit ~2 MeV per centimetre of water irrespective of their momentum (to within a negligible logarithmic increase with energy). We have designed and constructed a scintillator hodoscope [16] bracketing the VATLY Cherenkov detector from above and below to provide a trigger on such relativistic feed-through muons. The requirement of a coincidence between the upper and lower scintillators guarantees that the muon has fed through not only the Cherenkov tank but also the laboratory roof and the lower scintillators. Moreover, a measurement of the time of flight between the upper and lower scintillators allows for rejecting the few lower momentum muons that just make it through the tank and roof and stop in the lower scintillators. The present section describes the design, construction, assembly and running-in of the scintillator hodoscope and its use in the calibration of the Cherenkov detector.

2.1 The trigger hodoscope

2.1.1 Description

The trigger hodoscope includes two scintillator plates on top of the Cherenkov detector and two below. Figure 2.1 shows the geometry of the ensemble. The upper set is made of two 80×40 cm^2 scintillator plates, 3 cm thick, glued to 40×40 cm^2 lucite plates. The lower set is made of a 80×40 cm^2 scintillator plate which overlaps a 120×40 cm^2 scintillator plate as above. Each

plate is viewed by a *2"* photomultiplier tube (PMT) via a 15 cm long cylindrical lucite light guide. The PMTs of a same pair are located at opposite ends in order to avoid detecting muons that cross the lucite light guides where they would produce Cherenkov light. All plastic scintillators are wrapped in aluminium and black polyethylene sheets kept together with black scotch tape. The upper plates are inserted in a light-tight wooden box that fits them tightly. They are protected from rain by a small steel roof (Figure 1.13, Right). The lower pair is located inside the laboratory under the roof.

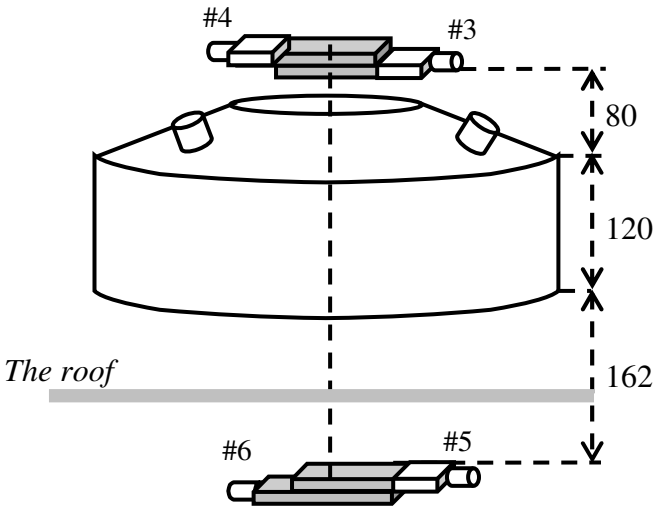

Figure 2.1 Schematic drawing of the set up (all distances are measured in cm).

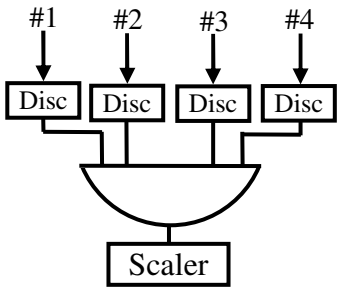

Figure 2.2 Electronic arrangement used to set up high voltages and delays.

2.1.2 High voltages and delays

The PMT high voltages and the timing of their signals have been adjusted using a rudimentary electronic arrangement (Figure 2.2). Each PMT signal is sent to a fast discriminator that produces a NIM pulse. Discriminators are set at a width of 15 ns and a threshold of 17 mV. Depending on the measurement to be

performed, a number (2, 3 or 4) of the above NIM signals are counted in coincidence using a four-fold coincidence unit, the output of which is sent to a scaler. Most atmospheric muons feeding through the Cherenkov counter are relativistic; hence the signals in the upper and lower pairs are separated by about 11 ns. The muon energy deposited in each plate by minimum ionizing particles is ~6 MeV/c. The dependence of the four-fold coincidence rate on each of the high voltages and each of the delays are displayed in Figures 2.3 and 2.4 respectively together with fits to simple analytical forms used to decide on the final settings, which are listed in Table 2.1.

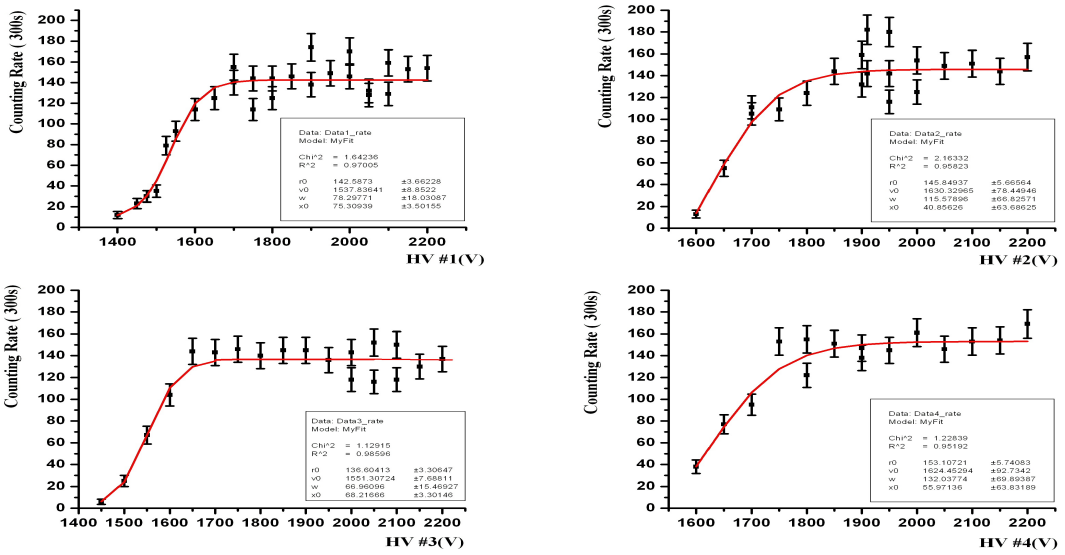

Figure 2.3 Dependence of the 4-fold coincidence rate on PMT high voltages

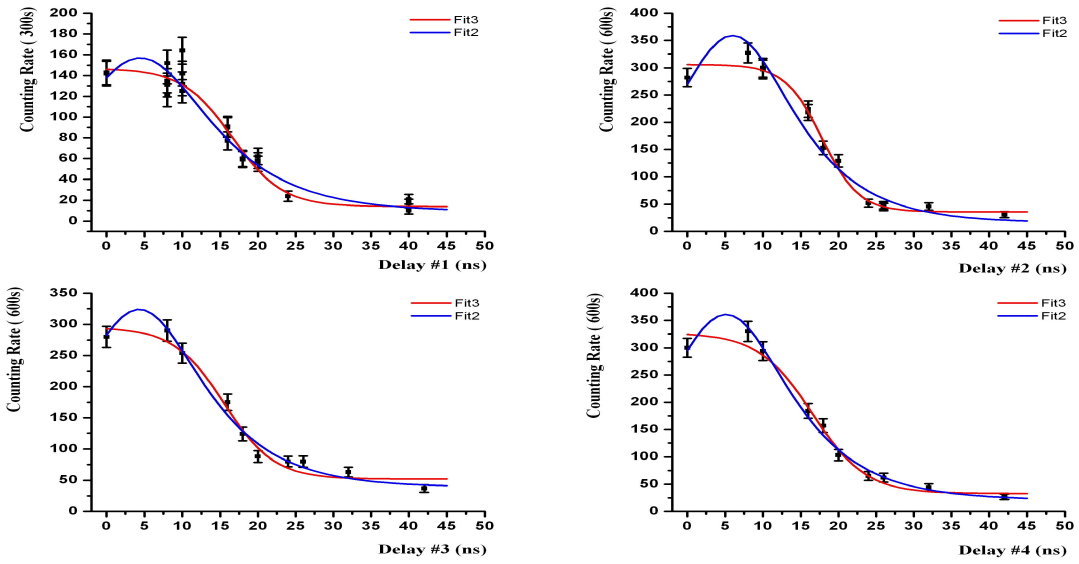

Figure 2.4 Dependence of the 4-fold coincidence rate on delays

Table 2.1 PMT high voltages and delays.

	PMT1	PMT2	PMT3	PMT4
V(V)	1765	1900	1790	1910
t(ns)	7	5	18	19

Using the final voltage and delay values listed in Table 2.1 and increasing the discriminator widths from 15 ns to 25 ns, the 3-fold and 4-fold coincidence rates are listed in Table 2.2 in units of $(600\ s)^{-1}$.

Table 2.2 Coincidence rates

Coincidence	Rate $(600\ s)^{-1}$
123	340 ± 18
124	470 ± 22
134	526 ± 23
234	466 ± 22
1234	287 ± 17
12	33110 ± 182
34	31960 ± 179

2.1.3 Rate

The 4-fold rate is 0.48 ± 0.03 Hz.

To a very good approximation, the triggering particles are vertical; the detector area is $0.80\times0.40=0.32\ m^2$ and its solid angle is $0.80\times0.40/3.7^2=0.023$ sr. Hence a detected flux $\Phi_{det}=0.48/0.023/0.32=65.0\pm3.8\ m^{-2}sr^{-1}s^{-1}$. A muon giving a 4-fold coincidence has to go through 185 g/cm^2 of material [7] between the two scintillator sets of the hodoscope (namely a 12000 l water tank, the laboratory roof and two other scintillator plates), corresponding to a 500 MeV/c momentum cut-off for muons while the muon flux at sea level (Hanoi) has a mean energy of 4 GeV. The correction for the sum of absorptions is done by the extrapolation of the above result using the data of Reference 7. Therefore the flux incident on the

upper scintillators is $\Phi = 70.3 \pm 4.1$ $m^{-2}sr^{-1}s^{-1}$ which is less than half a standard deviation away from the Reference 7 result.

2.2 Electronics

The scintillator hodoscope described above is used as a trigger to calibrate the response of the Cherenkov tank. The PMT high voltages have been increased by 100 V with respect to the values listed in the preceding section in order to be safely on plateau: they are set at 1'865 V, 2'000 V, 1'970 V and 2'010 V respectively. Discriminator widths have been set at 25 ns and thresholds at 17 mV. Each of the four hodoscope signals is resistively split into two equal pulses. One of these is sent after some delay to an Analogue-to-Digital Converter (ADC1) for measuring its charge. The other is sent to a discriminator that produces a NIM pulse used for building up the trigger and, after some delay, for stopping the Time-to-Digital Converters (TDC) that are started by the trigger pulse. A Timing-Unit (TU) is used to generate a dead time of 1 ms at the level of the trigger coincidence. In order to measure ADC pedestals, another TU is used as a clock giving a trigger with a frequency of the order of 1 Hz and a pattern unit (PU) tells which trigger (muon or pedestal clock) was active. The three Cherenkov dynode signals are amplified by a factor 10 and sent to ADC2. The final trigger pulse is used to open the ADC gates; it is broadened to 70 ns for ADC1 and to 150 ns for ADC2. A diagram of the trigger electronics is shown in Figure 2.5.

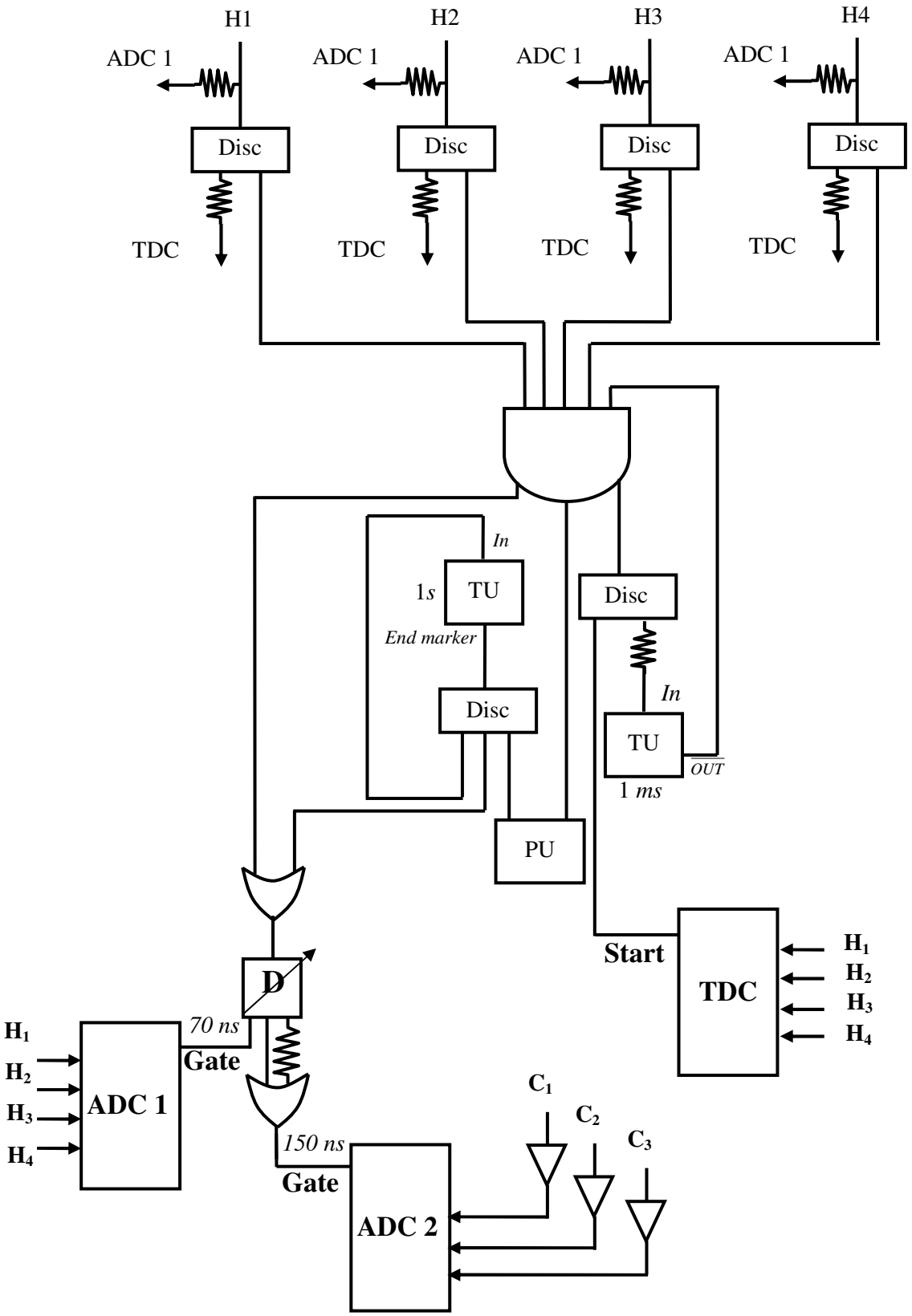

Figure 2.5 Schematic trigger electronic diagram used for the VEM measurement.

2.3. Analysis of hodoscope data

2.3.1 Charge distributions

ADC pedestals, recorded every second or so, are averaged over 250 successive clock triggers and used online for monitoring purpose. Typical distributions of these averages are displayed in Figure 2.6. The pedestals are usually quite stable but small variations are occasionally observed, usually associated with a change of input impedance of a contact in one of the connectors along the line bringing the signal from the PMT to the ADC. Moreover, an important VHF pick up is present on all signals, having its source in the television and mobile telephone emissions in the neighbourhood. But once they are averaged over the 70 ns fixed width ADC gate, their contribution is small enough not to significantly disturb the quality of the charge measurements.

Typical distributions of the pedestals around their means are shown in Figure 2.7. They have a typical rms value of 1 ADC channel. For convenience, for each individual run, the PMT signals are normalized off-line to a same average value of 100 ADC channels. Typical charge distributions are shown in Figure 2.8. Qualitatively, the shapes are Landau distributions typical of ionization losses in 3 cm of plastic scintillator. The rms to mean ratios are 69%, 57%, 64% and 64% for PMTs 1 to 4 respectively. Rejecting charges in excess of 100 ADC channels in one of the scintillator of a pair results in an only 5% decrease of the mean charge measured in the other scintillator and conversely when rejecting charges not exceeding 100 ADC channels. Such a positive correlation is expected if both scintillators of a pair are giving similar charge measurements for a given particle.

However, because of light absorption in the scintillator, one also expects an impact close to PMT1, and therefore far from PMT2, to give a larger charge in PMT1 than in PMT2. This effect would give a negative correlation which – if present – is hidden under the positive correlation mentioned earlier. In order to give evidence for it we can use the time information: an impact close to the PMT will give an earlier signal than an impact far from the PMT. Typically the

velocity of light in the scintillator is 3/4 of that in air and, because of reflections, light travels a factor $\sqrt{2}$ more than the actual distance between impact point and PMT. The maximum time difference, corresponding to 80 cm, is $80\times\sqrt{2}\times1.33/30 = 5$ ns.

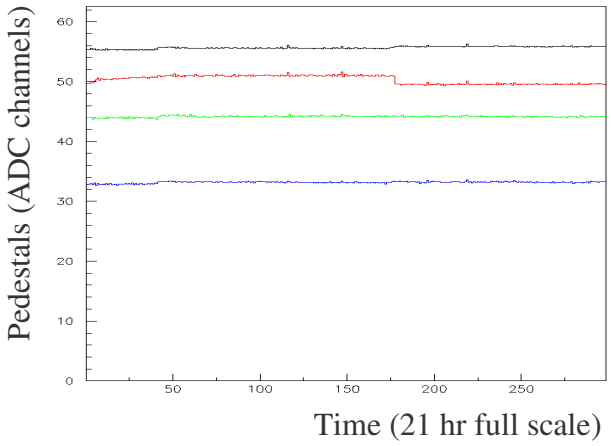

Figure 2.6 Typical time distributions of the hodoscope pedestals averaged over 250 successive clock triggers. Different colours (green, blue, red and black) correspond to PMTs 1, 2, 3 and 4 respectively. The figure covers a full run of 21 hours.

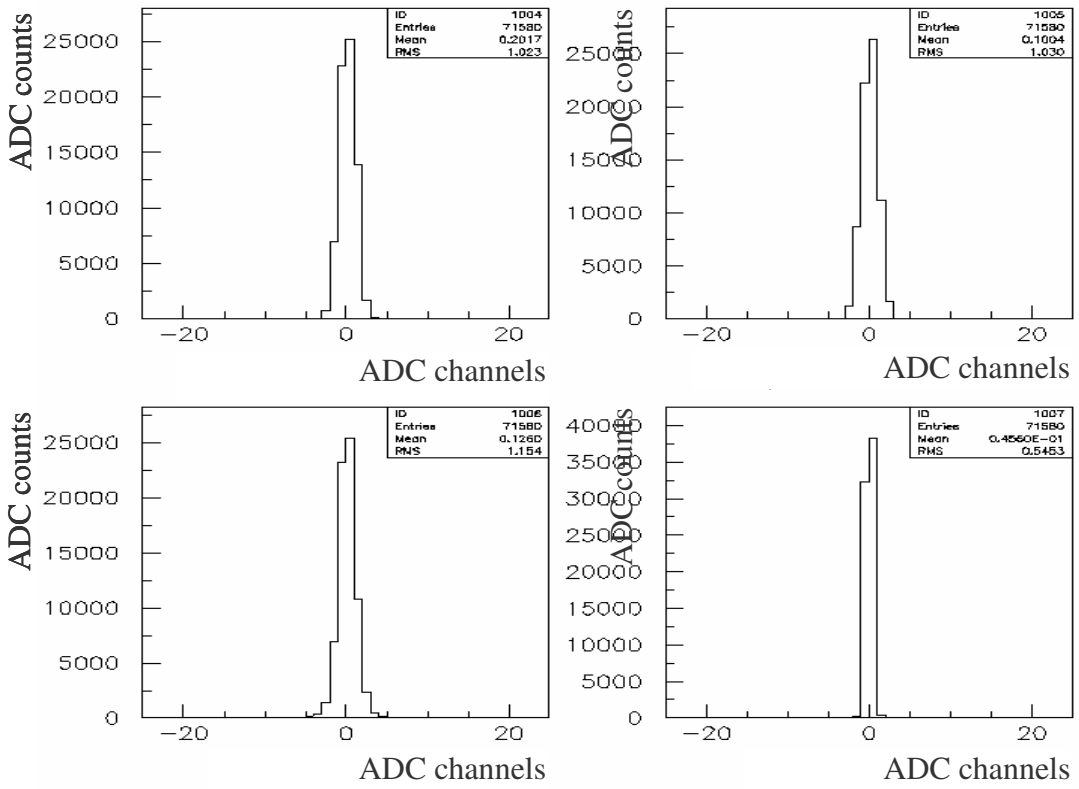

Figure 2.7 Distributions of the hodoscope pedestals around their averaged values (from left to right and top to bottom, PMTs 1 to 4).

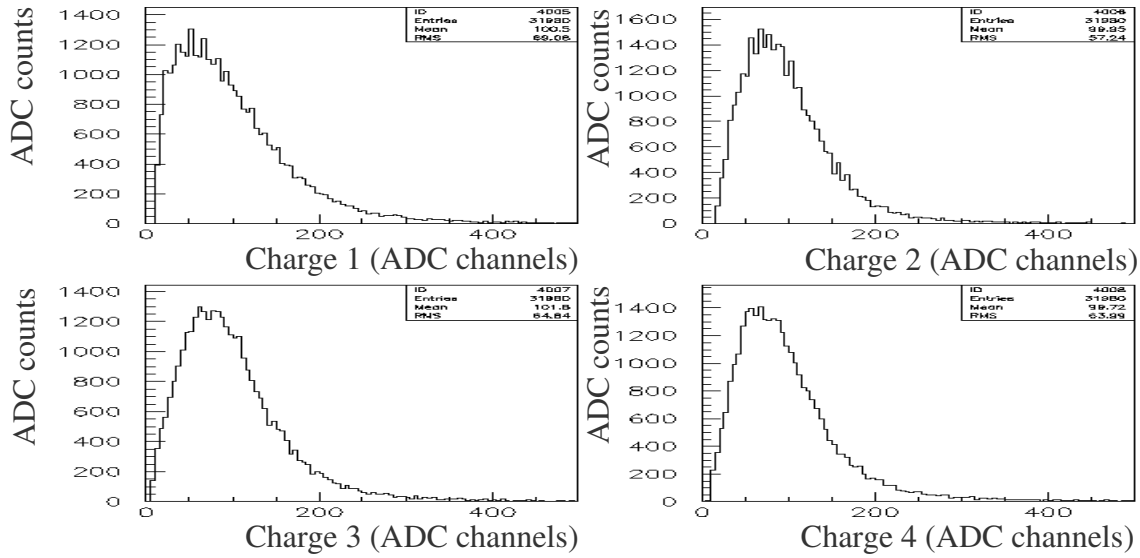

Figure 2.8 Typical charge distributions measured in the four hodoscope counters.

Figure 2.9 shows the correlation between the time difference t_2-t_1 in ordinate (7 TDC bins per ns) and the charge asymmetry $(q_2-q_1)/(q_2+q_1)$ in abscissa. Here, for both the upper and lower pair, the correlation is clearly negative as expected. Another effect contributing to it is time slewing: when a charge is small, the signal reaches the fixed discriminator level later than when a charge is large. Namely late times are associated with small charges both because of that latter effect (called time slewing) and because the light absorption in the scintillator is larger.

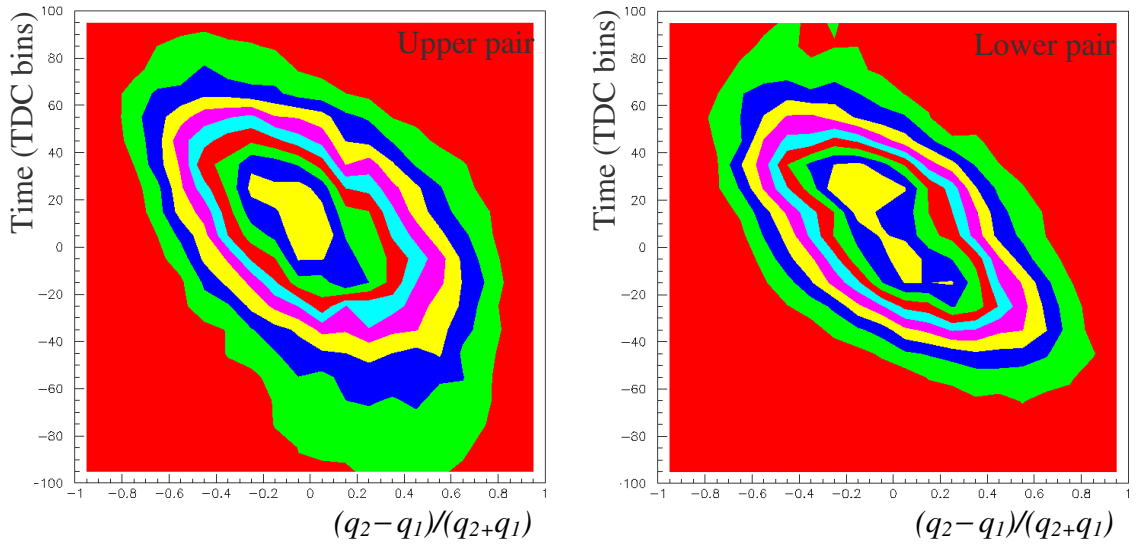

Figure 2.9 Correlation between the time difference (ordinate, in bins of 0.143 ns) and the charge asymmetry (abscissa) of the signals of a same pair.

Retaining as charge measurement the mean of the two charges of a pair and as time measurement the mean of the two times, these effects compensate and there is no need to correct for them. Typical distributions of the mean upper and lower charges are shown in Figure 2.10. The lines are the result of fits to a Landau distribution of the form $dN/dq=S_0\,exp\{-(y+e^{-y})/2\}$ with $y=(q-q_0)/\Delta q$. The values taken by q_0 and Δq are respectively 73 and 21 ADC channels for the upper pair and 74 and 20 ADC channels for the lower pair. The uncertainties on these parameters, as obtained from the fit, are respectively 0.4 and 0.2 channels in both cases.

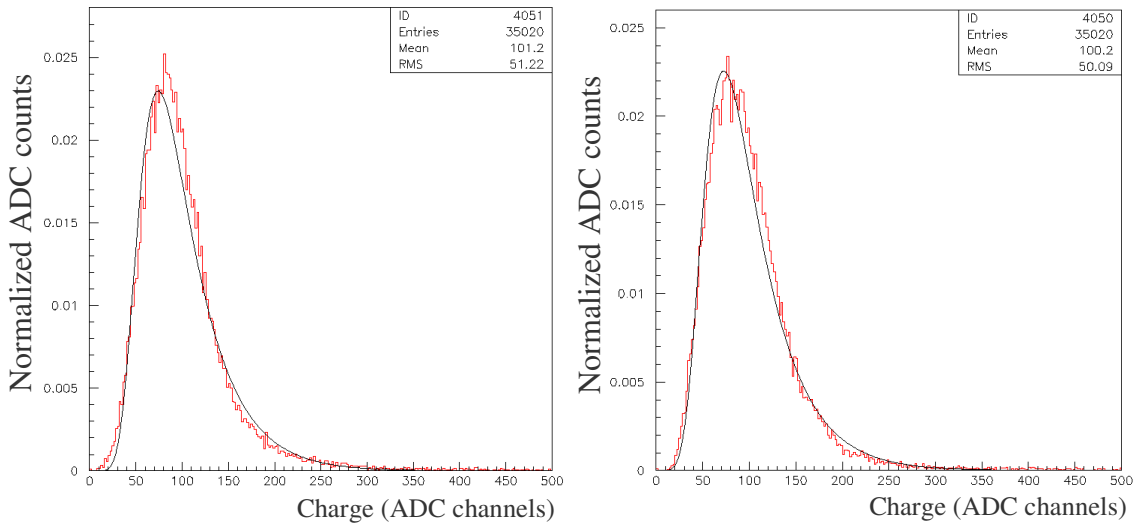

Figure 2.10 Typical upper and lower mean charge distributions and the corresponding Landau fits.

2.3.2 Time of flight

Figure 2.11 shows typical distributions of the arrival times of the signals in each of the hodoscope counters. The latest of the four signals defines the timing of the coincidence and, therefore, that of the TDC start: it is recorded at a fixed value in the associated TDC. As any other value is lower, a spike appears at the upper ends of the TDC distributions.

Figure 2.12 shows the distribution of the time of flight $\Delta t=t_3+t_4-t_1-t_2$. The distance between the two layers of the hodoscope is 3.62 m meaning a time of flight of about 11 ns for relativistic particles (corresponding to the zero of the

distributions in the figure). A muon having β=0.964, meaning $\gamma=(1-\beta^2)^{-1/2}$=3.76 and a momentum of 386 MeV/c, just makes it through the hodoscope. It gives a time of flight only 0.4 ns lower than relativistic muons, meaning 3 TDC bins. We expect relativistic feed-through muons to give lower time of flights and minimum ionizing charges; while low energy muons significantly slowing down in water should give larger times of flight and a higher down-to-up charge asymmetry. The correlation between these two quantities is shown in Figure 2.13.

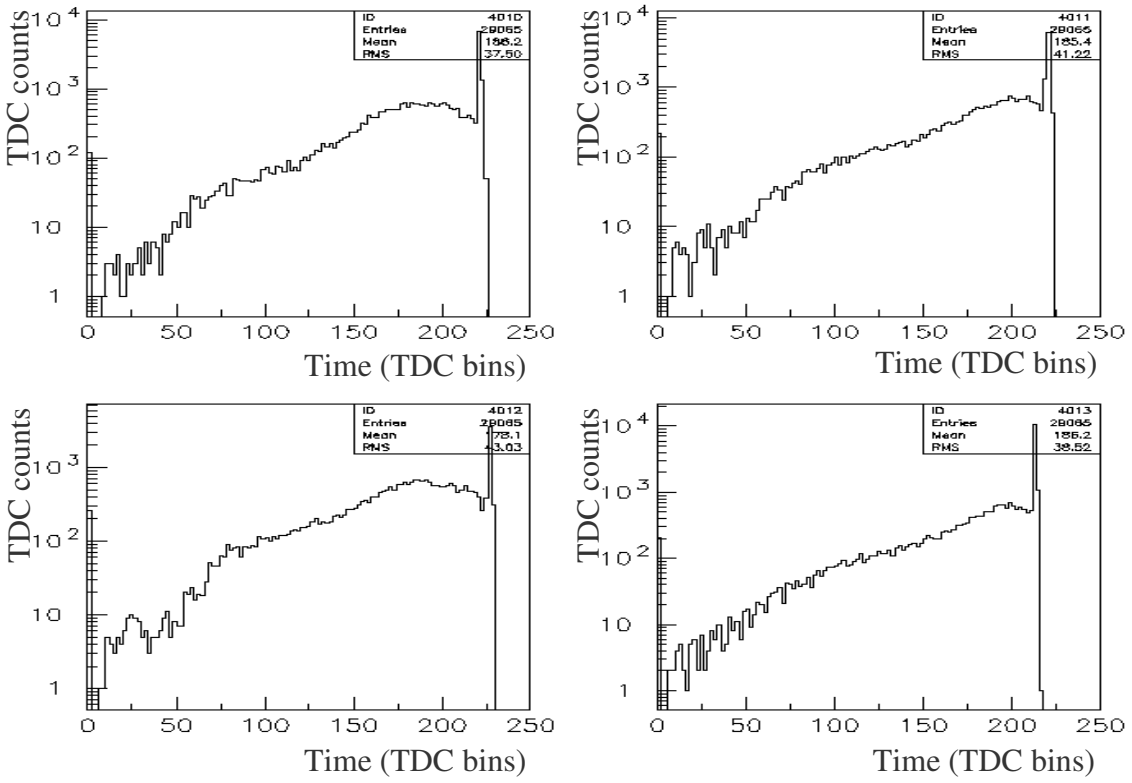

Figure 2.11 Time distributions measured in the hodoscope counters (7 TDC bins =1ns).

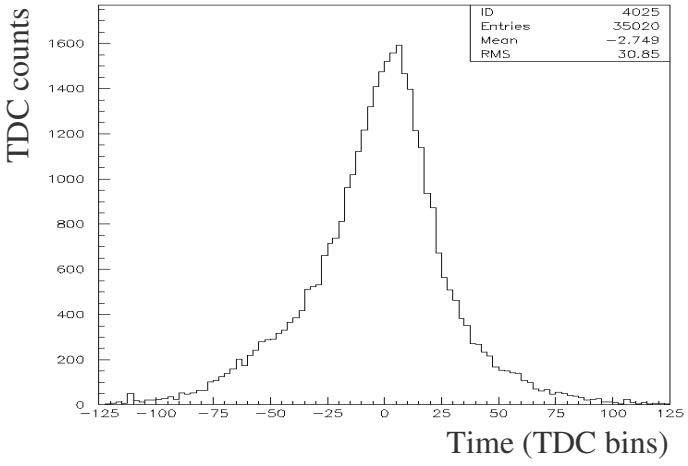

Figure 2.12 Typical time of flight distribution between the upper and lower hodoscope pairs (7 TDC bins=1 ns).

2.3.3 Event selection

The data displayed in Figure 2.13 do not show any sign of the positive correlation mentioned above: the effect is too small to be visible and time of flight cannot be used efficiently as a selection criterion. In order to improve the quality of the charge and time measurements in the hodoscope, we retain only events where each of the four charge measurements and each of the four time measurements obey the following cuts: charges should be between 30 and 223 ADC channels; times should be between the spike and 100 TDC channels below the spike. Together, these cuts remove 45.6% of the triggers. The time of flight distribution (Figure 2.14, left) is now 36% narrower (rms of 19.7 channels, meaning 2.8 ns). The mean charge distribution averaged over the four counters (Figure 2.14, right) is also significantly narrower. While the rms to width ratio was 50% in each of the upper and lower pairs before cuts (Figure 2.10), it is now 23% compared with $50/\sqrt{2}=35\%$.

However, good Landau fits can no longer be obtained, giving evidence for a spurious broadening of the signal. A good fit is obtained by smearing the Landau distribution (q_0=86 and Δq=7) with a Gaussian having an rms of 18 (units being ADC channels, namely ~1% of the mean) meaning relative contributions to the width of typically 14% of physics origin and 18% of instrumental origin.

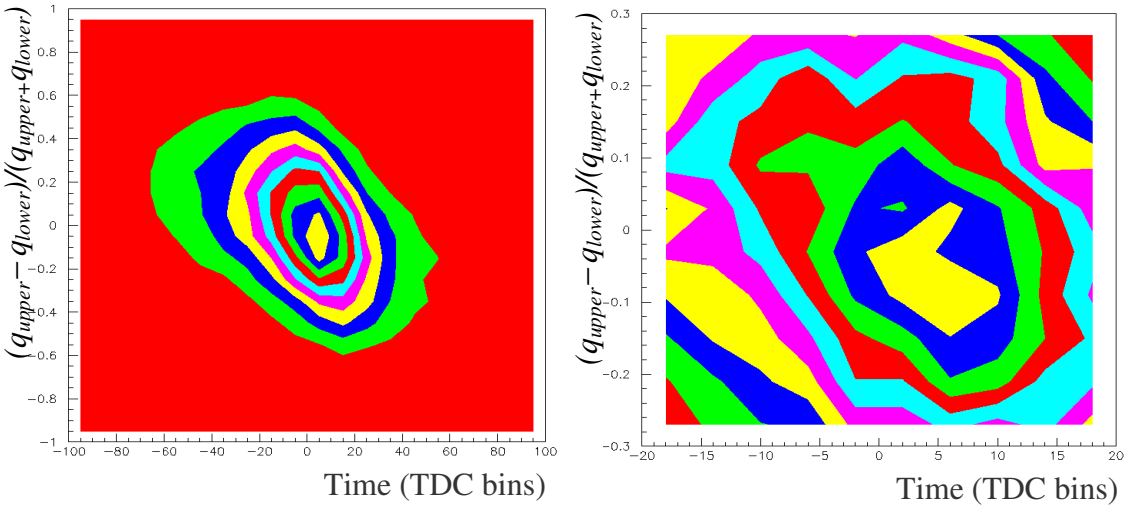

Figure 2.13 Typical correlation between time of flight (abscissa) and mean charge asymmetry (ordinate). The right panel shows the central part of the left panel.

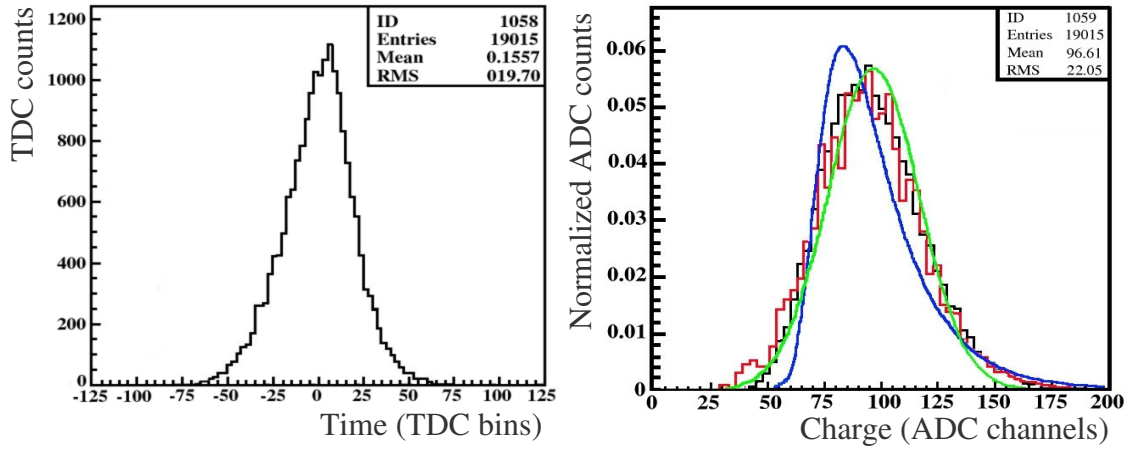

Figure 2.14 Time of flight (left panel) and mean charge (right panel) distributions after application of the cuts (see text). Fits to the charge distribution are pure Landau (blue), pure Gaussian (green) and smeared Landau (red).

2.3.4 Stability

In the preceding sections, a particular run was chosen as typical illustration. In the present section we comment on the stability of the hodoscope data. Table 2.3 lists the values taken over 10 runs by the following parameters after application of the cuts: the mean and rms values of the time of flight, the mean and rms values of the mean charge, the four PMT pedestals and the four PMT normalization constants.

Table 2.3 Hodoscope stability data

Run number (N_{run})	File name	ToF (TDC bins)		Charge (ADC channels)		Pedestals (ADC channels)				Scale			
		Mean	Rms	Mean	Rms								
1	*2402*	*–0.2*	*19.2*	*96.6*	*21.9*	*28*	*21*	*29*	*46*	*0.89*	*0.90*	*1.35*	*0.84*
2	*0203*	*–0.47*	*19.5*	*96.2*	*22.1*	*36*	*32*	*38*	*52*	*0.85*	*0.81*	*1.39*	*0.88*
3	*0303*	*0.09*	*19.4*	*96.6*	*22.1*	*40*	*36*	*46*	*55*	*0.89*	*0.82*	*1.39*	*0.88*
4	*0803*	*0.45*	*19.5*	*96.5*	*21.9*	*43*	*39*	*48*	*58*	*0.98*	*0.83*	*1.30*	*0.88*
5	*1203*	*0.07*	*19.6*	*96.5*	*21.9*	*44*	*34*	*50*	*55*	*0.97*	*0.83*	*1.24*	*0.89*
6	*1703*	*0.16*	*19.7*	*96.6*	*22.1*	*44*	*33*	*50*	*56*	*0.95*	*0.83*	*1.33*	*0.88*
7	*1803*	*0.61*	*19.6*	*96.5*	*21.9*	*44*	*33*	*50*	*56*	*0.99*	*0.83*	*1.29*	*0.90*
8	*2203*	*–0.02*	*19.8*	*96.0*	*21.7*	*46*	*33*	*50*	*55*	*1.01*	*0.82*	*1.25*	*0.89*
9	*2503*	*0.30*	*19.8*	*96.5*	*22.0*	*44*	*33*	*49*	*54*	*0.98*	*0.80*	*1.34*	*0.88*
10	*2603*	*0.50*	*19.6*	*96.4*	*21.7*	*44*	*33*	*49*	*54*	*1.00*	*0.80*	*1.33*	*0.88*

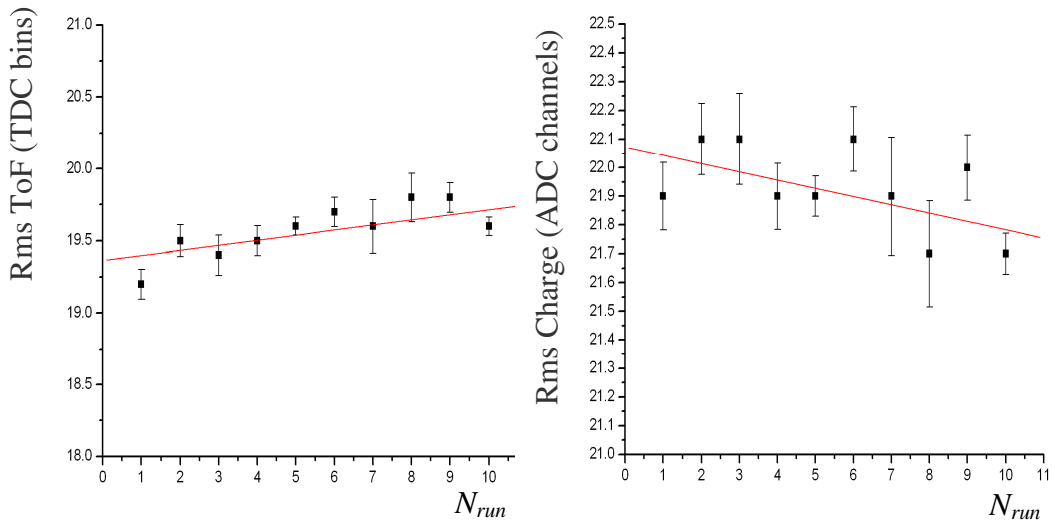

Figure 2.15 Dependence on run number of the rms values of the time of flight (left) and charge (right) distributions.

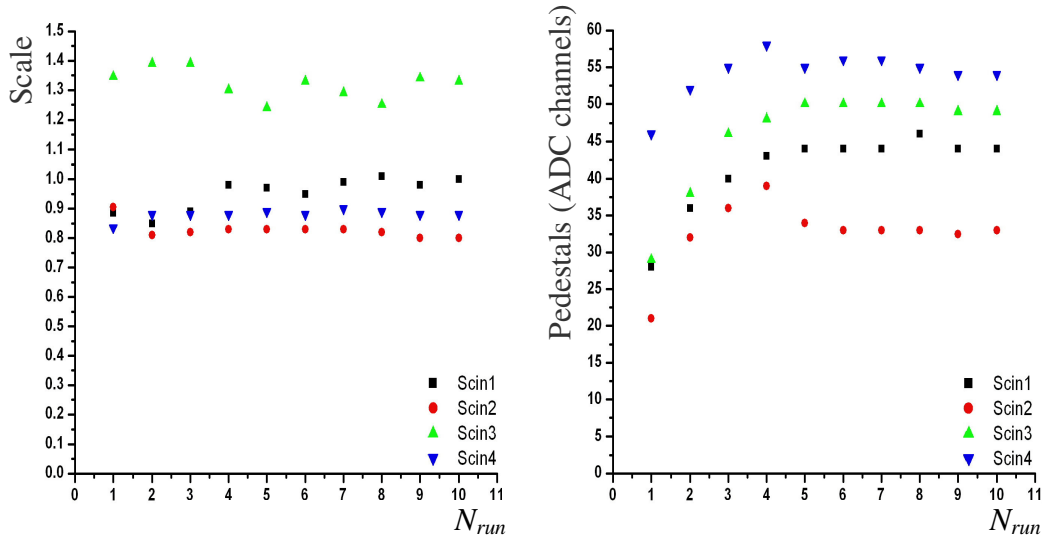

Figure 2.16 Dependence on run number of the normalization constants (left) and of the ADC pedestals (right) for the four hodoscope PMTs.

The dependence on run number of the rms values of the time of flight and mean charge distributions are illustrated in Figure 2.15 and that of the pedestals and normalization constants in Figure 2.16. Linear fits to the data of Figure 2.15 give for the time of flight $Rms=(19.4\pm0.1)+(0.04\pm0.01)\times N_{run}$ and for the mean charge $Rms=(22.1\pm0.1)-(0.03\pm0.01)\times N_{run}$. The variation is therefore barely significant.

2.4 Analysis of Cherenkov data

We set the high voltages of the PMTs of the Cherenkov counter as 1’390 V, 1’430 V and 1’283 V respectively in order to have, on average, 400 channels of signal above pedestal. The pedestals are continuously monitored as a function of time (Figure 2.17).

Pedestals are averaged over 250 successive measurements and these average values are retained as pedestals for the successive 250 measurements. The distribution of such average values over a typical run shows occasional spikes (upper panels of Figure 2.17). The distributions of individual pedestal measurements referred to the current average pedestal value (obtained from the preceding set of 250 measurements) have larger rms values than in the hodoscope case because of amplification. They reach 6, 4 and 8 ADC channels in PMT 1, 2 and 3 respectively. In early runs, PMT 1 and PMT 3 were seen to display important tails in their charge distributions but changing a leaky capacitor in a base and introducing silica gel in their environment solved the problem.

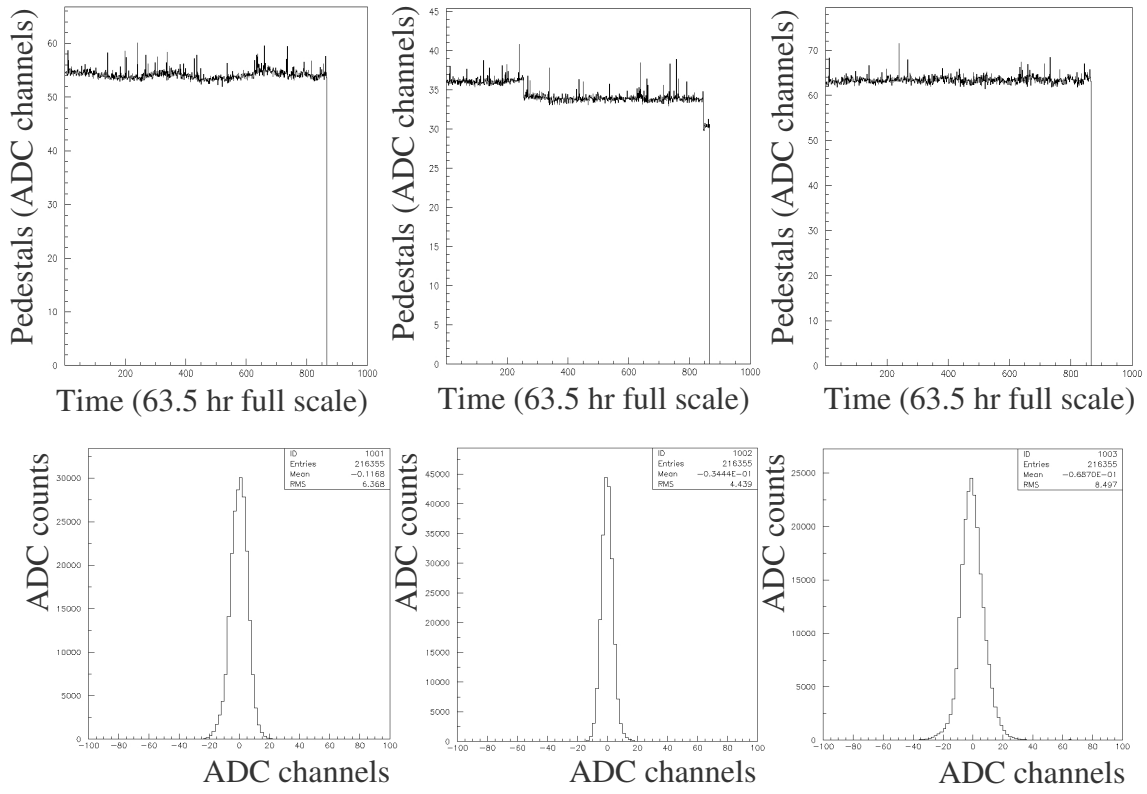

Figure 2.17 Upper panels: typical evolution of pedestals 1 to 3 during a run. Lower panels: typical pedestal distributions during the same run.

2.4.1 Response of the Cherenkov counter to a hodoscope trigger

Any particle (or set of particles) giving a hodoscope trigger must cross its upper and lower scintillator plates, and therefore have a total track length of at least 1.2 m in water. To the extent that its (their) velocity is above Cherenkov threshold, it (they) should give a Cherenkov signal. In particular, relativistic muons crossing the hodoscope are expected to account for most of hodoscope triggers and have a track length in water very close to 1.2 m: they should give signals having a narrow distribution around their mean. PMT gains have been adjusted for this mean value to be ~400 ADC channels. Figure 2.18 shows the corresponding charge distributions for each of the three PMTs and for the mean signal. As can be seen from the figure, all entries have a non zero charge. The rms values are 146, 128 and 139 ADC channels, which, quadratically combined, give 80 channels instead of 99 observed, giving evidence for correlations between the three measurements.

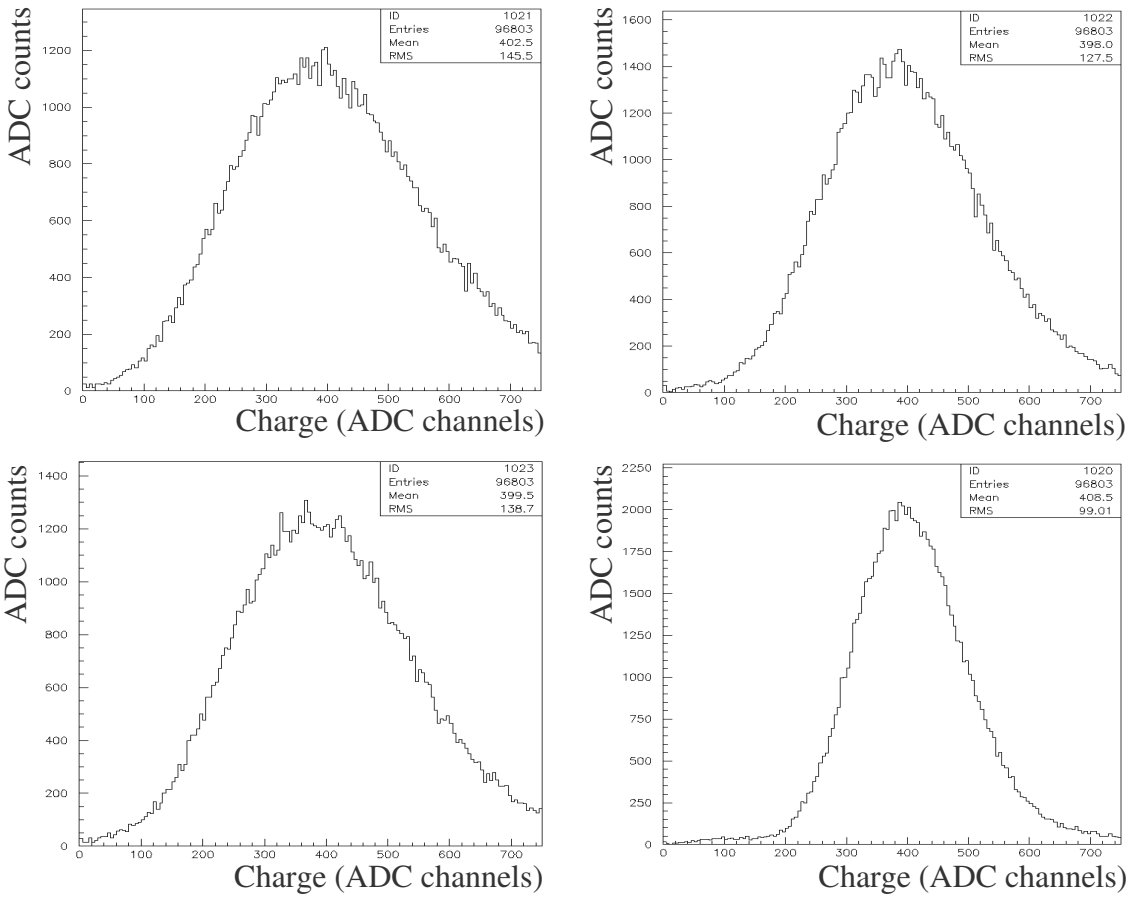

Figure 2.18 Charge distribution of individual PMTs and their average (last panel).

2.4.2 Selection of good muons

In all what follows, we define “good muons” as feed-through muons having a hodoscope charge between 30 and 220 ADC channels and a time of flight (defined as in Figures 2.12 and 2.14, *i.e.* after subtraction of ~11 ns) from −50 to 50 TDC bins. Typical charge distributions of individual PMTs and their mean are shown in Figure 2.19 for such “good muons”. The relative width of the mean charge distribution is now 22.5% compared with 24.2% before selection. It corresponds to 20±1 photoelectrons per VEM. The selection retains ~ 43% of the total number of triggers. The resulting VEM value is obtained from a Gaussian fit to the mean charge distributions averaged over four runs (Table 2.4). The result is 414±10 ADC channels.

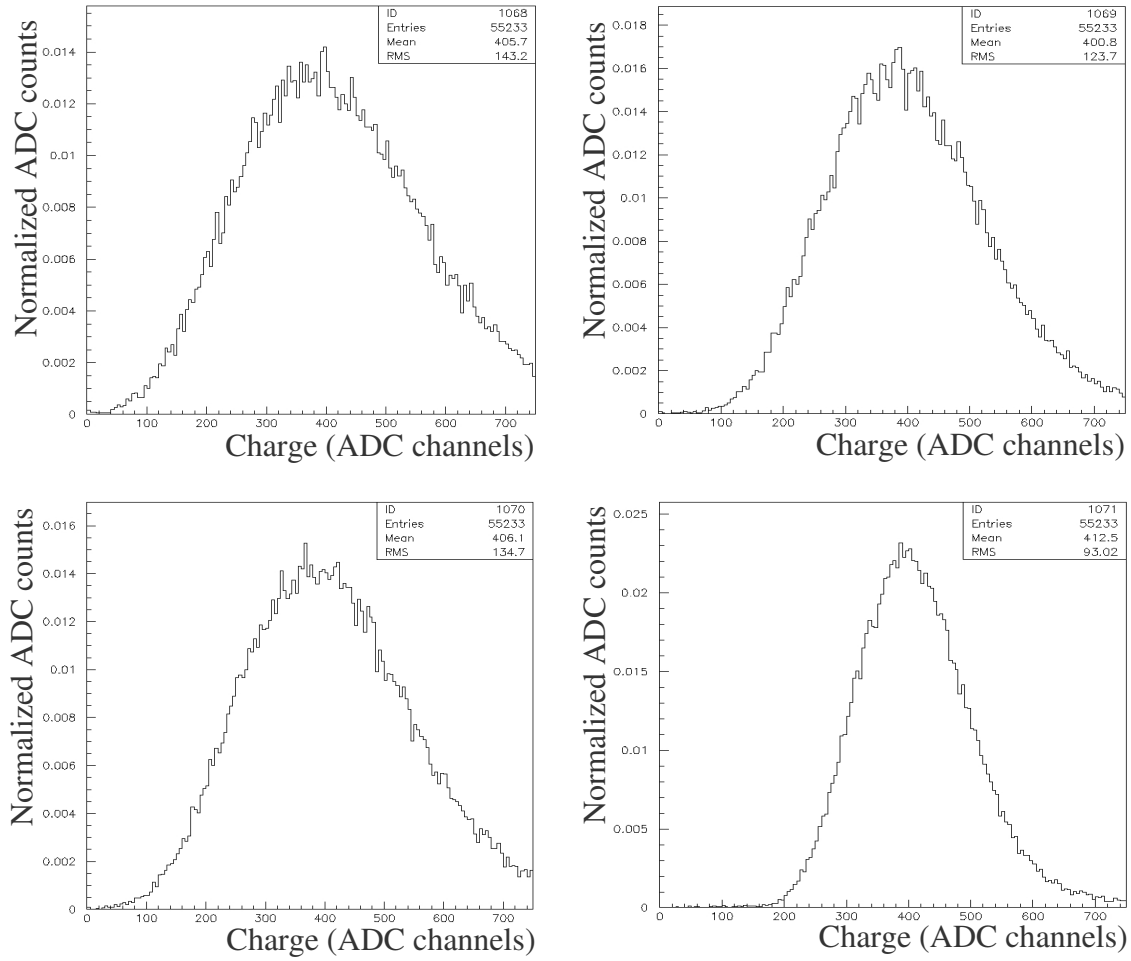

Figure 2.19 Charge distribution of individual PMTs and their average (last panel) after selection of “good muons”.

Table 2.4 VEM values obtained for four separate runs

File name	Before cut (fitted value)			After cut (fitted value)		
	Number of events	Mean (ADC channels)	Rms (ADC channels)	Number of events	Mean (ADC channels)	Rms (ADC channels)
2106	31955	419	93	18078	422	92
2206	96803	398	87	55233	399	89
2506	96135	419	92	55504	415	87
2806	31120	425	98	17718	421	96

2.4.3 Conclusion

The study of the Cherenkov response to relativistic vertical muons has shown a number of features that may be briefly summarized as follows:

– The value of the relative width of the charge distribution measured for "good" vertical muons, 22.5%, can be compared with that measured in the PAO, ~15%, implying that we have $(22.5/15)^2$=2.3 times less photoelectrons in VATLY than in the PAO. This results from both the lower water purity and the lesser quality of the wall diffusivity.

– 1 VEM corresponds to 414±10 raw ADC channels.

3. Muon decays in the VATLY Cherenkov tank

The present section uses simulations to evaluate what can be expected in terms of rates and charges from muons that stop and decay in the water volume of the VATLY Cherenkov detector. Both the stopping muon signal and the delayed signal from the decay electron need to be detected. A related study has been made by P.T. Nhung and P. Billoir using PAO data [17]. A measurement in the VATLY detector will provide useful information on its ability to detect very low charge signals.

3.1 Basic processes

The basic processes of relevance are the slowing down of muons in water due to ionization energy losses and the emission of Cherenkov photons. The largest possible track length in the Cherenkov tank is $l_{max}=\sqrt{1.2^2+3.6^2}$ ~3.8 m. Such a range corresponds to a muon momentum of ~0.8 to 0.9 GeV/c, meaning a kinetic energy T ~0.8 GeV. We can therefore assume that the differential energy loss is either at minimum or, in the lower energy range, inversely proportional to the muon kinetic energy [18]. We therefore adopt the following approximate formula for the differential energy loss:

$$TdT/dx \sim 138 \text{ MeV}^2\text{g}^{-1}\text{cm}^2 \text{ for } T<53 \text{ MeV}$$

$$dT/dx=1.8+0.8\{(331-T)/278\}^2 \text{ for } T>53 \text{ MeV}$$

At 53 MeV, dE/dx=2.6 MeV and at minimum (331 MeV) dE/dx=1.8 MeV.

The track length l of muons in water increases as a function of kinetic energy T as shown in Figure 3.1. We see from this figure that vertical muons start to feed through the tank (l>1.2 m) as soon as T exceeds 280 MeV.

The second basic process of relevance is the emission of Cherenkov radiation. The Cherenkov threshold is $\beta_0=1/n$=0.75 where n=1.34 is the refractive index of water. This corresponds to a kinetic energy,

$T_0=(E_0-mc^2)=54$ MeV, where $m=106$ MeV/c^2 is the muon mass, and $E_0=\gamma_0 mc^2=mc^2/\sqrt{1-\beta_0^2}$.

The half-aperture of the Cherenkov cone is $\theta=cos^{-1}(1/\beta n)$ and the density dN/dx of Cherenkov photons radiated by a muon having velocity β over a distance dx is proportional to $sin^2\theta=1-1/(\beta n)^2$. For $\beta=1$, θ ~41°. It is convenient to use VEM as unit: 1 VEM=120×80×(1−1/n^2) photons, where the number of photons per centimeter, dN_0/dx, has been taken equal to 80 in the wave length range of relevance. For three photomultipliers and a photocathode efficiency of 10%, this means 140 photoelectrons per VEM compared with ~100 in the PAO. Hence, in VEM units, dN/dx is independent of dN_0/dx:

$$dN/dx=\{1-1/(\beta n)^2\}/\{1-1/n^2\}/120=1.9\times10^{-2}\{1-1/(\beta n)^2\} \text{ VEMcm}^{-1}.$$

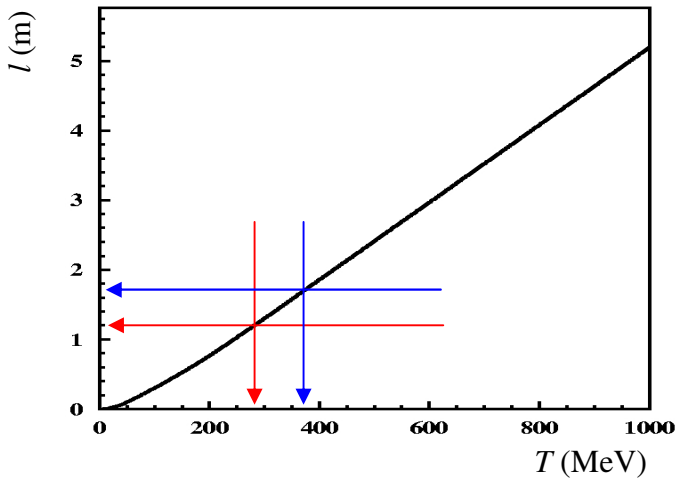

Figure 3.1 Muon track length in water (m) as a function of kinetic energy (MeV). Red arrows are for a muon that just stops in 1.2 m and blue arrows for a muon that just emits 1 VEM before stopping.

A muon having low enough a kinetic energy stops in the water tank. The number of photons it radiates depends only on the kinetic energy it has when entering the tank and so do its track length and the track length over which it radiated photons. In principle (but in practice it would require a much higher measurement accuracy than available here), measuring the signal produced by a stopping muon should therefore provide a measure of its initial kinetic energy.

This is illustrated in Figures 3.2 and 3.3 showing the dependence on kinetic energy of the total number of Cherenkov photons radiated by a muon before stopping. A 280 MeV muon that just stops in 1.2 m of water (red arrows in Figures 3.1 and 3.3) emits only ~2/3 of a VEM while a muon that just emits one VEM before stopping (blue arrows in Figures 3.1 and 3.3) has a kinetic energy of ~370 MeV and a track length of ~1.6 m. Of course, by definition, a relativistic muon emits 1VEM in 1.2 m of water.

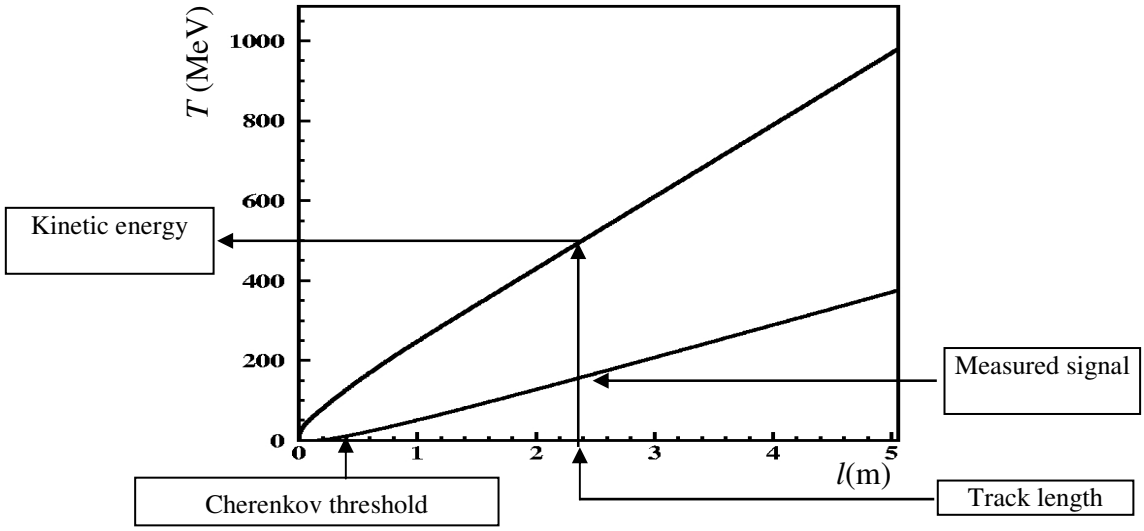

Figure 3.2 Dependence on track length of the initial kinetic energy of a stopping muon (upper curve and left hand scale) and of the number of Cherenkov photons radiated (lower curve, arbitrary units). The arrows illustrate how the initial kinetic energy can in principle be deduced from the muon signal.

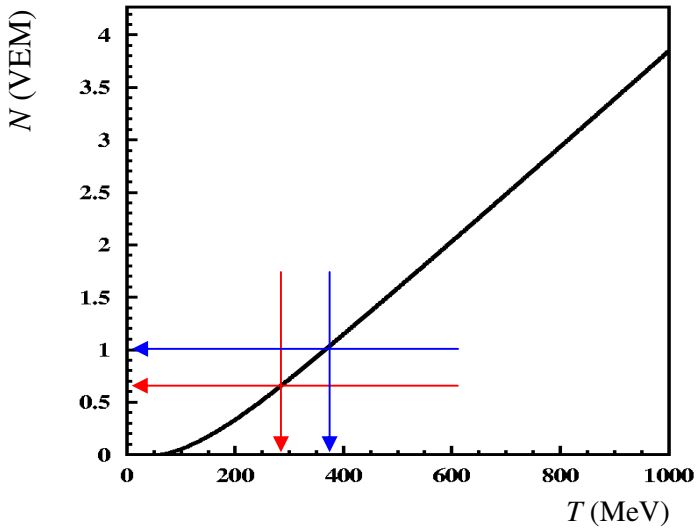

Figure 3.3 Total number of Cherenkov photons (measured in VEM units) radiated by a muon of kinetic energy T (MeV) in deep water. Red arrows are for a muon that just stops in 1.2 m and blue arrows for a muon that just emits 1 VEM before stopping.

3.2. Simulation of the detector and muon signal

We now use a toy Monte Carlo to simulate the response to muons. Muon trajectories are generated with an isotropic angular distribution, their distance to the centre of the water volume not exceeding $½l_{max}$. Each muon is given a weight $(1–0.108\sin^2\theta)\cos^2\theta$ in order to take account of the zenith angle dependence of the atmospheric muon flux in Hanoi [8].

The kinetic energy is generated with an exponential distribution of mean value E_{mean}. The length of the trajectory in the water volume is calculated and the number of radiated Cherenkov photons is evaluated as described in the preceding paragraph.We use a coordinate system having its origin O at the centre of the water volume, ***Oz*** vertical pointing upwards, ***Ox*** pointing west and ***Oy*** pointing south. The muon trajectories are taken as straight lines (multiple scattering is ignored) with unit vectors $\boldsymbol{u}=(u_x,u_y,u_z)=(\sin\theta\cos\varphi,\ \sin\theta\sin\varphi,\ \cos\theta)$. They are generated with uniform $\varphi \in [0,2\pi]$ and $\cos\theta \in [0,1]$ distributions. Those which cross the tank enter the water volume at A and leave it at B.

We define 5 families of trajectories (Figure 3.4): 1, missing the tank all together; 2, having A on the upper plate and B on the wall; 3, having A on the upper plate and B on the lower plate; 4, having both A and B on the wall; and 5, having A on the wall and B on the lower plate.

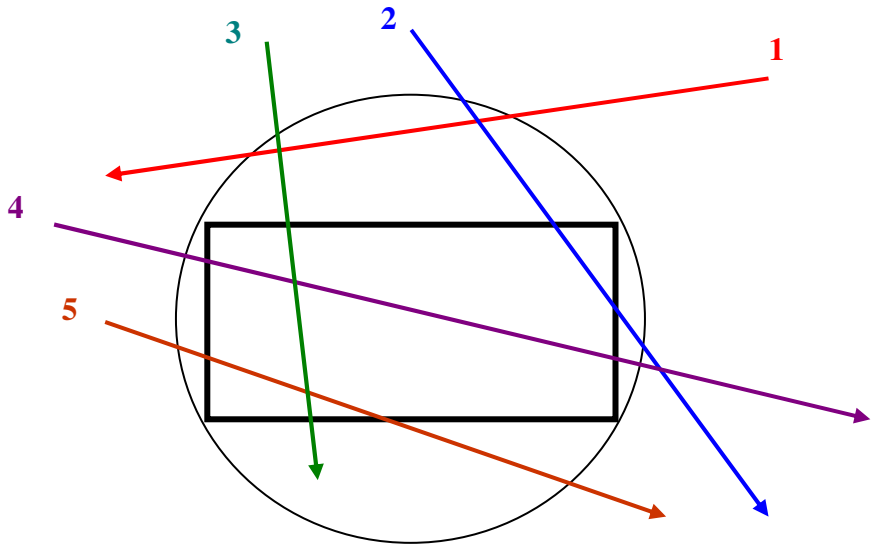

Figure 3.4 Definition of trajectory families.

Table 3.1 Properties of the five families of trajectories (E_{mean}=3 GeV).

Family	1 Missing	2+5 Wall-plate	3 Plate-Plate	4 Wall-wall
Abundance	9.7%	42.2%	47%	1.1%
Fraction stopping	–	5.3%	7.8%	9.2%
<VEM> feed-through	–	0.73	1.19	1.47
<VEM> stop	–	0.22	0.28	0.55
$<f>$	–	0.74	0.81	0.84

A muon may produce no detectable photon either because it misses the tank or because its kinetic energy is lower than the Cherenkov threshold. Moreover, it may or may not stop in the tank. If it does not, it does not produce any detectable decay electron. Table 3.1 gives the properties of the five families for E_{mean}=4 GeV and Figures 3.5 to 3.8 display the distributions of their track length and of the Cherenkov light emitted by the muon (in VEM), whether stopping or not in the water volume.

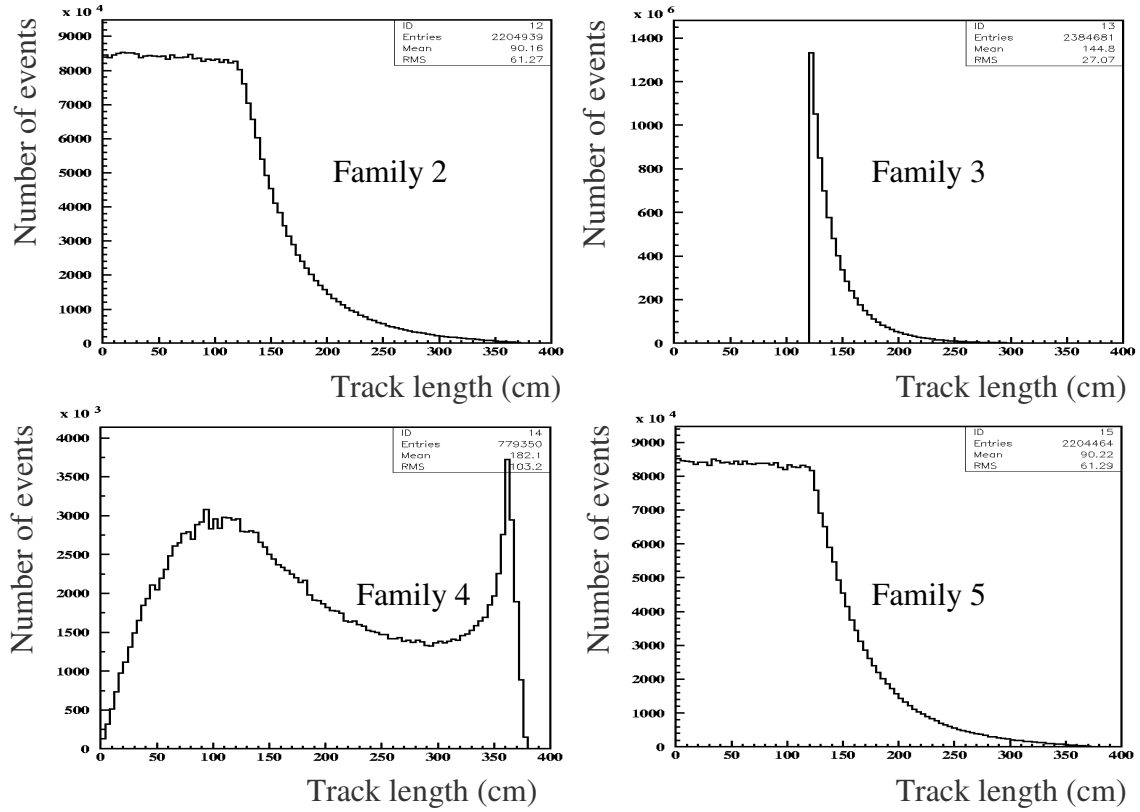

Figure 3.5 Track length distribution for families 2 to 5. Note the different vertical scales.

As shown in Figure 3.5, families 2 and 5 share identical properties. Indeed, they both have tracks joining the side wall to the upper or lower plate, and which of these two plates is implied is irrelevant as the problem is symmetric with respect to *O*. From now on, we shall therefore group families 2 and 5 together into a single one. Tracks of this family can have zero length when they hit a corner and are then expected to have a flat distribution as their impact scans the side wall vertically. This is indeed what is observed. Then, when their length exceeds 1.2 m, their distribution decreases and cancels at the maximum possible track length, l_{max}~3.8 m. Tracks of the third family, joining the upper to the lower plate, are always longer than 1.2 m and may also reach l_{max}, however this is relatively much less probable than in the former case. Finally, tracks of the fourth family must be close to horizontal if they are long, in which case they show the typical 1/cosine distribution corresponding to the projected density of a circle. If they are short, they may have all possible zenith angles and the decrease of the cosmic flux with zenith angle competes with geometry to produce a broad maximum at ~1 m track length. While the plate-wall and plate-plate configurations have comparable abundances, the wall-wall configuration is much less likely, only ~1% of the total.

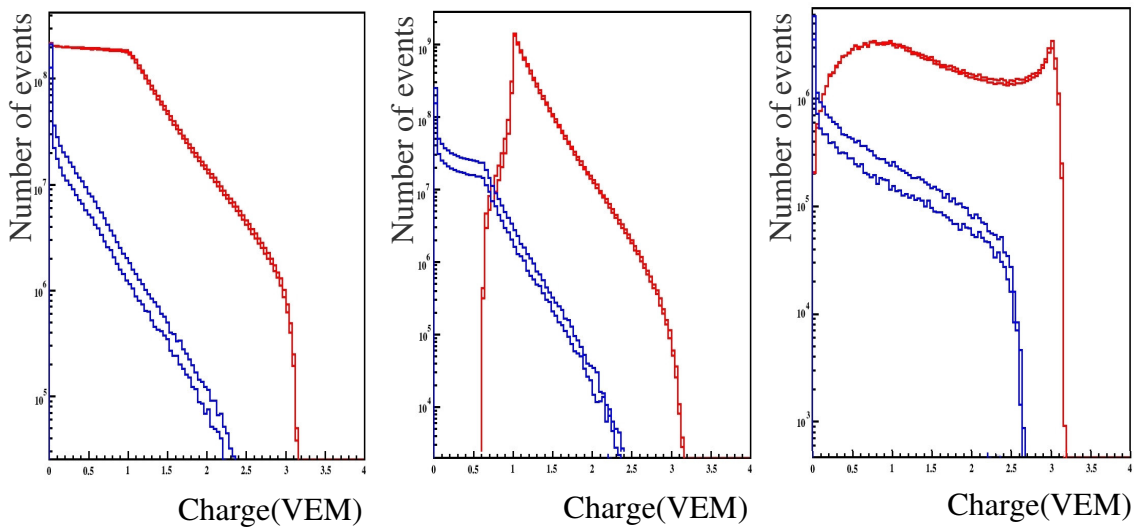

Figure 3.6 Charge distributions (VEM) for feed-through muons (red) and stopping muons (blue) respectively. The curves are for E_{mean}=3 and 5 GeV. Families 2+5, 3 and 4 are displayed from left to right. Note the vertical log scales.

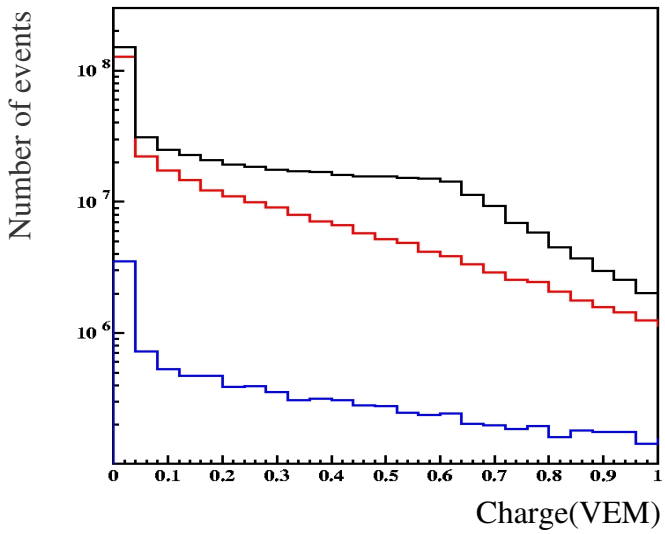

Figure 3.7 Charge distribution (VEM) for stopping muons and E_{mean}=5 GeV. Families 2+5, 3 and 4 are shown in red, black and blue respectively. The spikes at zero are from stopping muons having β below Cherenkov threshold.

The number of Cherenkov photons produced would correspond to the collected charge in the ADC if the detector were perfect. We calculate it in VEM units, using the considerations of the preceding paragraph. As it depends on the kinetic energy distribution, we assume an exponential distribution with mean E_{mean}=3, 4 or 5 GeV. The mean charges listed in Table 3.1 are for E_{mean}= 4 GeV. The fraction of stopping muons is ~6.5% on average, slightly larger for the plate-plate configuration than for the plate-wall configuration. As shown in Figure 3.6, the dependence on E_{mean} is weak, the larger E_{mean}, the less likely it is for the muon to have low enough energy to stop in the water volume. On average, the Cherenkov light emitted by a stopping muon corresponds to one quarter of a VEM. Figure 3.7 shows their distributions for E_{mean}= 5 GeV. The spikes at zero charge corresponds to track lengths smaller than the 11 cm during which a muon no longer radiates before finally stopping. Figure 3.8 illustrates further the influence of geometry on the stopping probability.

The expected total rate is ~1.4 kHz for feed-through muons and therefore ~20 Hz for coincidences of two feed-through muons in a 10 μs window. The total stopping muon rate is at the 100 Hz scale. Of these, only a fraction will be detected and an even smaller fraction will produce a detectable decay electron.

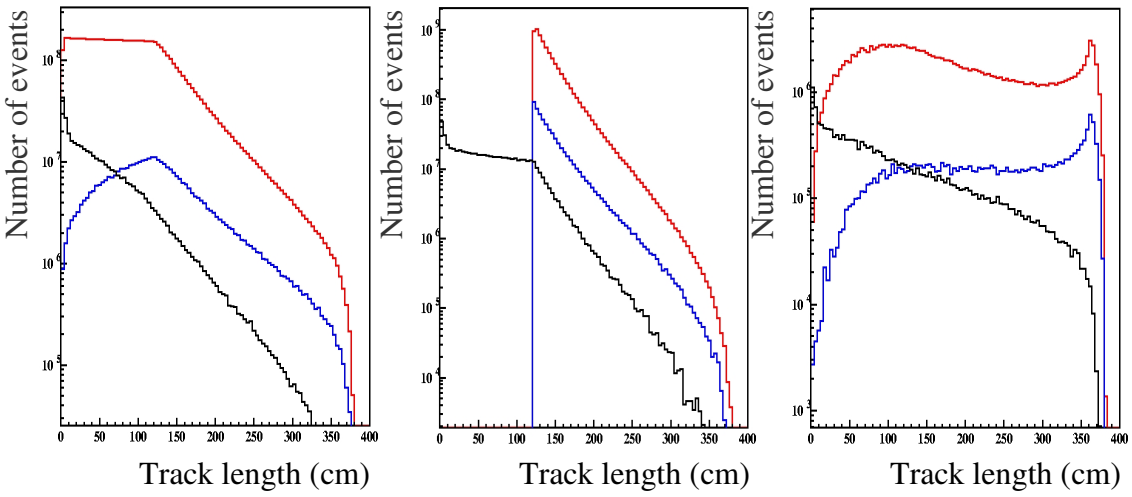

Figure 3.8 Track length distributions at E_{mean}= 4 GeV for feed-through muons (red) and stopping muons (black). The blue curves are, for stopping muons, distributions of the length of the trajectory between its intersections with the tank wall.

For the decay electron (meaning electron or positron) to be detected, the muon should not stop too close from the tank walls: when calculating the expected rate, one should consider a fiducial volume slightly smaller than the tank volume. Once averaged over muon polarization, the electron may be emitted forward or backward with equal probabilities and the bulk of the electron shower covers some 20 cm (one radiation length is 36 cm). The energy E carried by the decay electron, averaged over polarization and electron emission angle, has a distribution of the form $dN/dx=2(3x^2-2x^3)$ where $x=2E/M_\mu c^2$ varies between 0 and 1. The mean value of x is 0.7, meaning for E a mean value of 37 MeV. This is a very low energy and in practice, only the high energy tail of the shower energy distribution will be detected. In order to mimic the effect of the fiducial volume, one simply multiplies E by a factor $f=(1-½exp(-L_{upstream}/\Lambda)(1-½exp(-L_{downstream}/\Lambda)$ where $L_{upstream}$ and $L_{downstream}$ are the distances separating the stop point from the entrance and respectively exit points of the trajectory in the water volume, Λ defining the shower size and being commensurate with the radiation length. The f factor is unity when the muon stops far from the tank walls ($L_{upstream}$ and $L_{downstream} >> \Lambda$) and is equal to ½ when the muon stops close to the wall. Its distributions are illustrated in Figure 3.9 for E_{mean}=4 GeV and Λ=24 cm. As seen from Table 3.1, on average, f is of the order of three quarters. Muons producing

Cherenkov light stop far from the entrance point of the trajectory: the *f* factor has very little effect when applied to the entrance wall once the presence of a muon signal has been required. On the contrary, it has a significant effect on the exit wall end, in particular for muons producing larger Cherenkov signals. We note that the mean electron signal is known [17] to be around 0.12 VEM in PAO data.

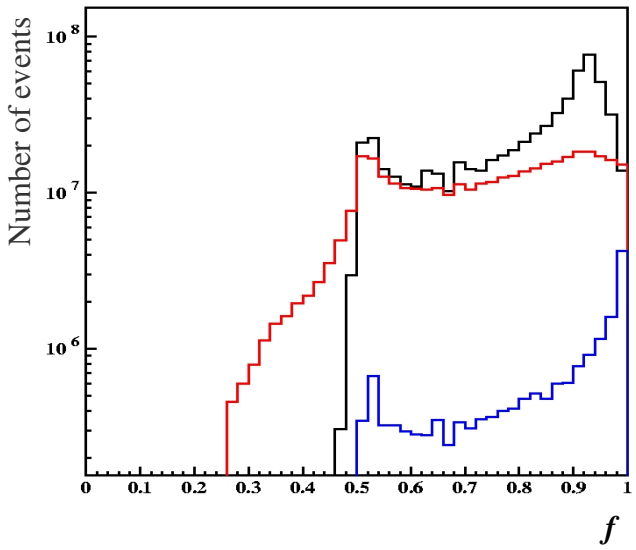

Figure 3.9 Distributions of the fiducial volume factor *f* for families 2+5 (red), 3 (black) and 4 (blue) respectively.

4. Auto-correlations: rates and time distributions

In the present section and the three sections that follow, we study auto-correlation spectra from the VATLY Cherenkov detector and, for comparison, from scintillator plates. The aim is double: first to obtain information on the detection of very low charge signals in the Cherenkov detector, second to measure the probability of having two muons from a same shower be simultaneously detected in the VATLY Cherenkov tank. The present section is an introduction to the subject and presents some general features of auto-correlation spectra.

4.1 The problem

We consider a detector producing an output signal S with a rate R. S is fed at both start and stop inputs of a Time-to-Amplitude Converter (TAC), the start signal being delayed by Δ_0 in order to avoid that a single S signal could both start and stop the TAC. Ideally, it should be sufficient to have Δ_0 exceed the width δ_0 of S. In practice, however, because of possible after-pulses associated with S (poor impedance matching, ringing, PMT after-pulsing, etc…) one will adjust $\Delta_0 > \delta_0$ in order to avoid measuring trivial instrumental correlations. When two consecutive pulses are separated by a time $t > \Delta_0$, the stop arrives a time $t-\Delta_0$ after the start and the TAC gives an output signal O called autocorrelation signal with amplitude proportional to $t-\Delta_0$. Its amplitude distribution is therefore a measure of the distribution of the time separation between the two consecutive pulses, $f(t)$. When analyzed in a multichannel analyser (analogue-to-digital converter) it produces an auto-correlation spectrum that reflects the distribution $f(t)$. When there is no stop within a time T_{range} after a start, the TAC produces no output and is ready to register a new start pulse.

4.2 No correlation

The simplest case is when there is no correlation between two successive signals *S*. For example, *S* may be produced by thermal noise in the detector or by a long-lived radioactive source. The probability to have *S* occur between *t* and *t+dt* is then a constant equal to *Rdt*. Taking the first pulse as origin of time, the probability to have the next pulse between *t* and *t+dt* is therefore the product of *Rdt* by the probability $lim_{n\to\infty}(1-Rt/n)^n=exp(-Rt)$ that there had been no stop signal beforehand. Hence $f(t)=Rexp(-Rt)$. The autocorrelation spectrum is a decaying exponential with time constant *1/R*.

Taking in account the delay Δ_0,

$f(t)=Rexp(-R[t-\Delta_0])=Rexp(R\Delta_0)exp(-Rt)$ for $t>\Delta_0$.

4.3 Cosmic rays

Cosmic rays on Earth are secondary particles produced in a cascade of interactions triggered by a primary particle (usually a proton) in the Earth atmosphere. Such cascades, called extensive air showers, hit ground in the form of numerous nearly isochronous particles. Their density decreases almost exponentially with the distance to the impact on ground of the shower core. Their time distribution decreases rapidly with a typical microsecond scale.

For a detector of area *A*, the probability of having two particles of the same shower hit the counter depends on energy and on the distance of the detector to the shower core but is proportional to *A* as long as *A* is much smaller than the area covered by the shower on ground. If the detector is small enough, this probability can be neglected: two successive signals *S* are always associated with different showers and we are in the case of Section 2 above. When the detector is large, we call *g(t)dt* the probability to have a second shower particle detected in the counter between *t* and *t+dt* after the arrival of the first particle. Their contribution to *R* is $R'\int g(t)dt$, the sum running from 0 to infinity, with $R'= R/(1+\int g(t)dt)$.

Using the time of the first pulse as origin, the probability to detect a second particle from the same shower, $g(t)dt$, competes with that of having a particle from another shower, Rdt. We may approximate $g(t)=g_0R_{sh}exp(-R_{sh}t)$, in which case $R'=R/(1+g_0)$. We shall assume that $g_0<<1$ and $R_{sh}>>R$.

The probability of having had no stop signal before time t is the product of $exp(-R[t-\Delta_0])$ by $1-\int g(t)dt$ where the sum is from Δ_0 to t, namely:

$$exp(-R[t-\Delta_0])\{1-g_0[exp(-R_{sh}\Delta_0)-exp(-R_{sh}t)]\}$$

$$= exp(R\Delta_0)\{Aexp(-Rt)+g_0exp(-[R+R_{sh}]t)\} \text{ with } A=1-g_0exp(-R_{sh}\Delta_0)$$

Hence $f(t)= exp(R\Delta_0)\{R+g_0R_{sh}exp(-R_{sh}t)\}\{Aexp(-Rt)+g_0exp(-[R+R_{sh}]t)\}$

$$= exp(R\Delta_0)\{ARexp(-Rt)+g_0(AR_{sh}+R)exp(-[R+R_{sh}]t)+g_0^2R_{sh}exp(-R+2R_{sh}]t)\}$$

$$\sim exp(R\Delta_0)\{ Rexp(-Rt)+g_0R^*exp(-R^*t)\} \text{ with } R^*=R+R_{sh}$$

The auto-correlation spectrum is the sum of two exponentials, one with decay time $1/R^*$ and the other with decay time $1/R$. The ratio of their amplitudes is g_0R^*/R. The effective decay rate depends on t: the spectrum is no longer a single exponential. Note that Δ_0 acts only as a threshold on t but not on the shape of the curve. The factor $exp(R\Delta_0)$ is only there for normalization (the probability for $t\rightarrow\infty$ must be unity).

4.4 Muon decays and muon captures

Let us assume that Δ_0 is large enough for g_0 to be negligible as well as after pulses. Then $f(t)=Rexp(-R[t-\Delta_0])$.

However, at sea level, most cosmic particles are muons, some of which may stop in the detector and decay or be captured. Those which stop and decay will produce an electron which might give a signal. Let f_{stop} be their fraction.

In vacuum, muons decay with a decay time $\tau_d=1/R_d=2.20$ μs. In matter, negative muons may be captured with a rate R_c. In such a case, decay and capture compete: if the muon has decayed, it no longer may be captured, and if it has been captured, it no longer may decay (at least for quite a while). The

disappearance rate of negative muons is therefore $R'=R_c+R_d$. Note that the capture rates in carbon and oxygen are respectively 0.038 and 0.103 per microsecond [19]. The μ^+ to μ^- ratio in Ha Noi is of the order of 1.25, meaning a fraction of negative muons ρ_-~0.44 [20]. The probability for an electron signal to occur between time t and $t+dt$ from the decay of a stopped muon having given a signal is therefore, η being the probability to detect the decay electron,

– in the case of a positive parent muon, $\eta R_d \exp(-R_d t)dt$

– in the case of a negative parent muon, $\eta R_d \exp(-R't)dt$

The probability to have an electron signal between t and $t+dt$ is therefore $f_{stop}\eta R_d\{(1-\rho_-)\exp(-R_d t)+\rho_- \exp(-R't)\}\, dt$, which reduces to $f_{stop}\eta R_d \exp(-R_d t)\, dt$ when there is no capture. The total electron rate is therefore

$$R_{el}=Rf_{stop}\eta\{(1-\rho_-)+\rho_- R_d/R'\}.$$

Consider first the no capture case, $R_{el}=R f_{stop}\eta$

$$f(t)=\exp(-R[t-\Delta_0])\{1-f_{stop}\eta R_d \int \exp[-R_d t]dt\}\{R+f_{stop}\eta R_d \exp(-R_d t)\}$$

where the sum extends from Δ_0 to t.

$$f(t)=\exp(-R[t-\Delta_0])\{1-f_{stop}\eta\{\exp[-R_d\Delta_0]-\exp[-R_d t]\}\}\{R+f_{stop}\eta R_d \exp(-R_d t)\}$$

$$=\exp(R\Delta_0)\{A\, R\exp(-Rt)+B\exp(-[R+R_d]t)\}$$

$$A=1-f_{stop}\eta\exp[-R_d\Delta_0] \sim 1\ ;\ B=f_{stop}\eta R+Af_{stop}\eta R_d \sim f_{stop}\eta(R_d+R)$$

$$f(t) \sim \exp(R\Delta_0)\{R\exp(-Rt)+f_{stop}\eta[R+R_d]\exp(-[R+R_d]t\}$$

Including capture, $f(t)=f_+(t)+f_-(t)$

$$f_+(t)=(1-\rho_-)\exp(R\Delta_0)\{R\exp(-Rt)+f_{stop}\eta[R+R_d]\exp(-[R+R_d]t\}$$

$$f_-(t)=\rho_-\exp(R\Delta_0)\{R\exp(-Rt)+f_{stop}\eta[R_d/R'][R+R']\exp(-[R+R']t\}$$

$$f(t)=\exp(R\Delta_0)\{R\exp(-Rt)+f_{stop}\eta(1-\rho_-)[R+R_d]\exp(-[R+R_d]t$$

$$+f_{stop}\eta\rho_-[R_d/R'][R+R']\exp(-[R+R']t\}$$

The auto-correlation spectrum is the sum of a muon term with decay time $1/R$ and of two electron terms, one with decay time $1/[R+R_d]$, the other with decay time $1/[R+R']$. The relative amplitudes of the electron terms are

$(1-\rho_-)f_{stop}\eta R_d/R$ and $\rho_- f_{stop}\eta R_d/R$ respectively.

4.5 Decays, captures and multimuons

Combining the effects discussed in the preceding sections, we obtain (no capture), writing $\varphi=f_{stop}\eta$:

$$f_+(t)=(1-\rho_-)\exp(R\Delta_0)\exp(-Rt)\{1+g_0\exp(-R_{sh}t)-g_0\exp(-R_{sh}\Delta_0)+\varphi\exp[-R_dt]$$

$$-\varphi\exp[-R_d\Delta_0]\}\{R+g_0R_{sh}\exp(-R_{sh}t)+\varphi R_d\exp(-R_dt)\}$$

$$\sim(1-\rho_-)\exp(R\Delta_0)\{R\exp(-Rt)+g_0[R+R_{sh}]\exp(-[R+R_{sh}]t)+\varphi[R+R_d]\exp(-[R+R_d]t)\}$$

$$f_-(t)=\rho_-\exp(R\Delta_0)\{R\exp(-Rt)+g_0[R+R_{sh}]\exp(-[R+R_{sh}]t+\varphi[R_d/R'][R+R']\exp(-[R+R'])t)\}$$

Writing $R_{sh}^*=R_{sh}+R$, $R_d^*=R_d+R$, $R'^*=R_d+R_c+R$, $\varphi_+=f_{stop}\eta(1-\rho_-)$

and $\varphi_-=f_{stop}\eta\rho_-R_d/(R_d+R_c)$

$$f(t)=\exp(R\Delta_0)\{R\exp(-Rt)+g_0R^*_{sh}\exp(-R^*_{sh}t)+\varphi_+R^*_d\exp(-R^*_dt)+\varphi_-R'^*\exp(-R'^*t)\}$$

To a good approximation, R_{sh}, R_d and R_c are much larger than R, and we may write:

$$f(t)=R\exp(-Rt)+g_0R_{sh}\exp(-R_{sh}t)+\varphi_+R_d\exp(-R_dt)+\varphi_-R'\exp(-R't)$$

Indeed, under such an approximation, the probability of having a stop in the TAC range is very small (most starts are not accompanied by a stop) and the probability of having two stops in the TAC range is negligible; $f(t)$ is then simply the sum of the independent contributions of four possible stops: a muon from a new shower, a muon from the same shower, a decay positron and a decay electron. The probability of having a stop in the TAC range is therefore obtained by integrating the associated terms in the expression of $f(t)$ between Δ_0 and

Δ_0+T_{range}. As $k\int_a^b exp(-kt)dt = exp(-ka)-exp(-kb)$

$k\int_{\Delta_0}^{\Delta_0+T_{range}} exp(-kt)dt = exp(-k\Delta_0)\left\{1-exp(-kT_{range})\right\}$ and we obtain for the probabilities, writing R_+ for R_d and R_- for R' :

$$P=P_R+g_0P_{sh}+f_{stop}\eta(1-\rho_-)P_++f_{stop}\eta\rho_-(R_+/R_-)P_- \text{ with}$$

$$P_R=1-exp(-RT_{range})$$

$$P_{sh}=exp(-R_{sh}\Delta_0)\{1-exp(-R_{sh}T_{range})\}$$

$$P_+=exp(-R_+\Delta_0)\{1-exp(-R_+T_{range})\}$$

$$P_-=exp(-R_-\Delta_0)\{1-exp(-R_-T_{range})\}$$

4.6 Simulation

In order to study the above relations, a toy Monte Carlo code has been written using as default input parameters (unit of time is microsecond): R_+=1/2.2; R_-=1/1.8 (carbon); R_{sh}=1; R=2×10^{-3}; g_0=0.2%; φ=0.5%; ρ_-=0.44; Δ_0=1; T_{range}=10. Fits of the generated TAC spectrum to a sum of exponentials are then used to recover the input parameters from the generated distributions.

In a first step, one sets g_0=0 and varies φ. One then fits the TAC spectrum according to the above expression, using as free parameters the overall normalisation constant, the decay time $1/R_+$ and φ. The other parameters are fixed to their correct value (i.e. R_{sh}, g_0, ρ_-, T_{range} and Δ_0) except for R which we may fix or keep free. The fit gives good results when the electron signal is strong enough but gives bad muon lifetimes when the electron signal is weak with respect to the statistical accuracy (Figure 4.1). For such weak signals, what happens is that $1/R_+$ and φ become strongly correlated as illustrated in Figure 4.2.

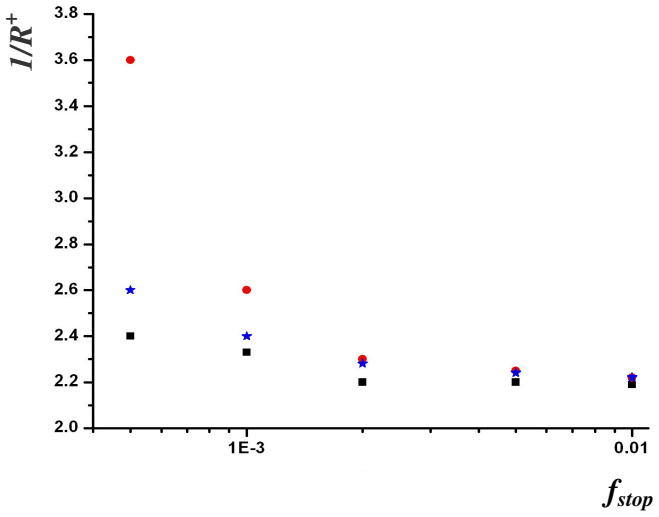

Figure 4.1 Best fit values of the mean muon decay time, $1/R_+$, as a function of $f_{stop}=\varphi/\eta$. For the lower statistics and leaving all parameters free (red circles), the best fit value of the muon decay time is too high unless the signal is very strong. For higher statistics and still leaving all parameters free (blue stars), the result is much improved. But even with the lower statistics fixing R to its input value (black squares) gives a good result.

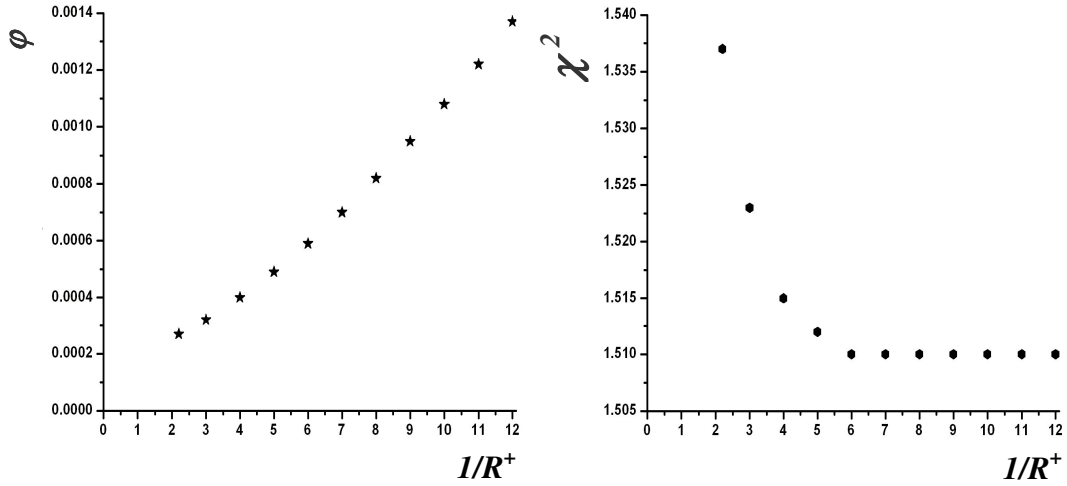

Figure 4.2 Example of a low signal case, φ=0.00025. The correlation between φ and $1/R_+$ as obtained from the fit is illustrated on the left panel. The associated very small variations of χ^2, less than 2%, are displayed on the right panel.

It is therefore important to fix as many parameters as possible in order to obtain reliable fit results. In practice, the values of R, R_+, R_- and ρ_- are known and can be fixed in the fit. This is studied in a second step where TAC spectra are generated with various values of $\varphi=f_{stop}\eta$ and g_0 and fitted to the sum of four

exponentials with R, R_+, R_- and ρ_- fixed. The free parameters are, in addition to an overall normalization factor, φ, g_0 and R_{sh}.

The results are illustrated in Figures 4.2 and 4.3.

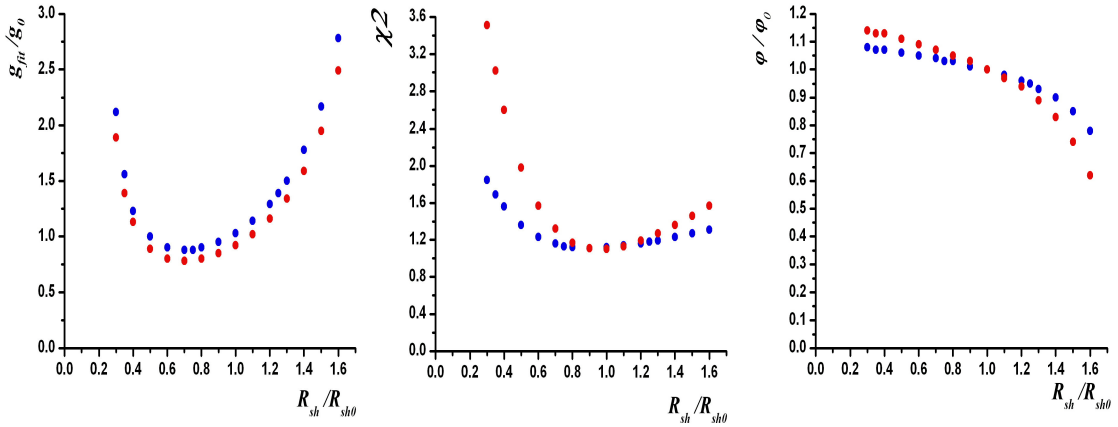

Figure 4.3 Example of fits of a time distribution generated with g_0=0.0005 (blue dots) or g_0=0.001 (red dots), $1/R_{sh}$=1 and φ=0.005. Left panel: dependence on $1/R_{sh}$ of the fitted value of g_0 when g_0, φ and the overall normalisation parameter are adjusted by the fit. Middle panel: same as left panel but showing φ instead of g_0. Right panel: dependence of the χ^2 on $1/R_{sh}$.

5. Auto-correlations: electronics and data acquisition

The recorded data include autocorrelation spectra and charge distributions. The autocorrelation spectra use a Time-to-Amplitude Converter (TAC), the output of which is sent to a Multi-Channel Analyzer (MCA). The charge distributions are measured in Analogue to Digital Converters (ADC) using a CAMAC data acquisition system.

A simple fast electronic circuit, using the NIM standard, is used as front end. It is common to the Cherenkov and scintillator configurations.

The signal studied is a coincidence between two photomultiplier tubes (PMT) signals. In the Cherenkov case, they are the dynode signals of PMTs 1 and 2, pre-amplified in the PMT bases; in the scintillator case, they are the anode signals of the two PMTs collecting separately the scintillation light. These are then amplified twice in succession using fast home made amplifiers having gain 10 each. The signals sent to the ADCs are passively split at the output of the first amplification stage. An additional split between the first and second amplification stages is used to halve the signal amplitude and the outputs of the second amplification stage are sent to fast discriminators, the output of which are used in coincidence to produce the main signal.

5.1 Auto-correlation measurement

The autocorrelation measurement uses the main signal as both start and stop signals of the TAC. However, care is taken to maintain a low rate at the TAC input in order to assure its proper behaviour. This is done by replacing the main signal by a coincidence between itself and another main signal occurring within a time window of W_1 μs following it. We call δt the time difference between the two signals. In practice, the main signal is triplicated using a fan-out NIM unit. One copy of it is used as input to a timing unit TU1 having a delay D_1 and width W_1. In principle, D_1 should simply exceed 50 ns in order to prevent an overlap with the input signal. In practice, however, a larger value is preferable in

order to be clear of possible undershoots, ringing or after-pulses associated with the main pulse. In the present set-up, values of D_1 vary from 0.5 μs to 5 μs. The output of TU1 is used as a gate to a discriminator having as input another copy of the main signal. The output of this discriminator (having a width of 50 ns) has therefore the same timing as the second signal and is used to start the TAC. It is delayed by δt μs with respect to the main signal. Other outputs of this discriminator are used as inputs to a CAMAC pattern unit and to the ADC gate (Figure 5.1). The third copy of the main signal (at the fan-out output), in anticoincidence with the TU1 output, is used as input to a second timing unit, TU2, having delay D_2 and width W_2. The anticoincidence prevents stopping the TAC with the same signal as that which starts it. The role of TU2 is to provide a stop signal to the TAC with proper fixed width W_2 (50 *ns*) and delay D_2 after the main signal, implying a delay $D_2–\delta t$ after the start signal. A detailed timing diagram is shown in Figure 5.2. With such logic, both the start and stop inputs of the TAC are activated only when the main signal is followed by another within a window $[D_1, D_1+W_1]$ with respect to the first, thus reducing the rate considerably. It must be noted, however, that it is the second of these signals that starts the TAC and the first that stops it, resulting in a time distribution inverted with respect to normal. The TAC output is sent to the MCA after passive division by a factor 4.

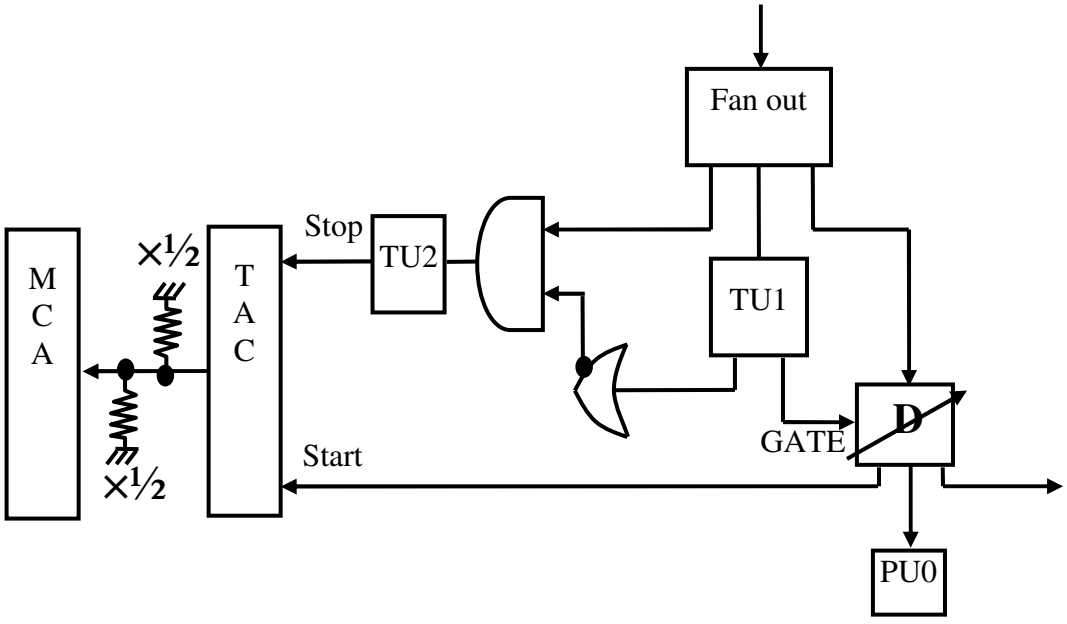

Figure 5.1 TAC logic diagram.

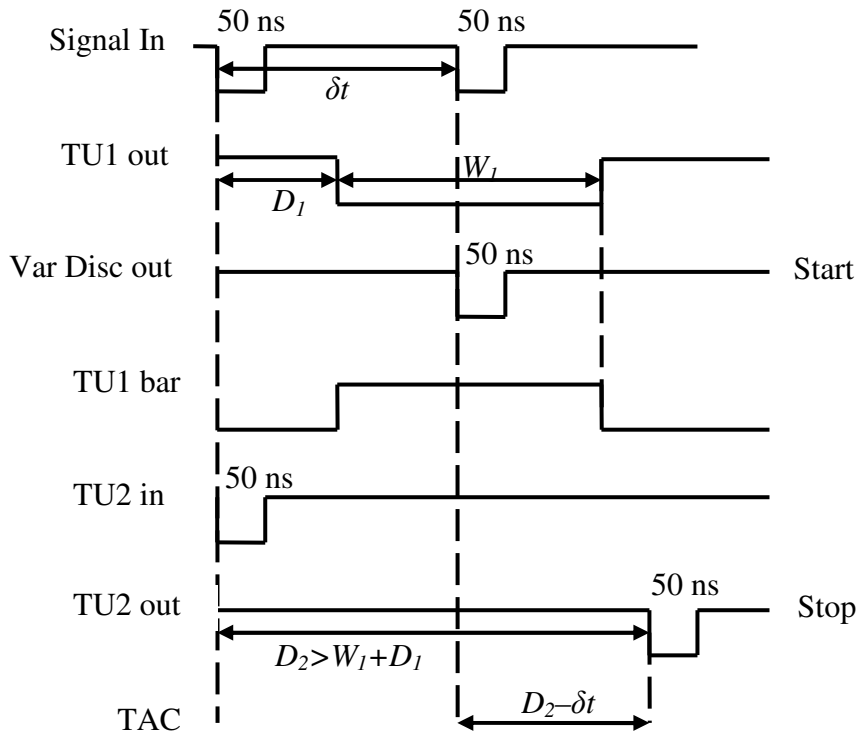

Figure 5.2 TAC timing diagram.

5.1.1 Timing considerations

As can be seen from Figure 5.2, the value of D_2 must exceed D_1+W_1. As the TAC is being used with a nominal range of 10 μs full scale, this implies that $D_1+W_1-\delta t<D_2-\delta t<10\ \mu s$.

We checked this on actual spectra, recording the values of the lower channel, C_{low} and that of the upper channel, C_{high} for different values of D_2, D_1 and W_1. The dependence of C_{high} on $D_2–D_1$ is displayed in Figure 5.3. It shows a linear dependence, as expected, up to the point where the TAC limit, 11.8 μs is reached. We also notice the presence of a spike that disappears as soon as $D_2–D_1 >\sim W_1$ (Figure 5.4). This is studied in detail in section 5.13. The dependence of C_{low} on $D_2–D_1–W_1$ (Figure 5.5) shows a linear dependence down to 120 channels. However, the number of channels stops changing and stays at ~120 for $D_2–D_1–W_1$ < ~0.6 μs. This means that there is a pedestal at ~120 channels and a threshold at ~0.6 μs. These results can be summarized as follows:

For $D_2–D_1–W_1<\sim 0.6\ \mu s$, $C_{low}=120$

$D_2–D_1–W_1>\sim 0.6\ \mu s$, $C_{low}=120+229(D_2–D_1–W_1-0.6)$

$D_2–D_1$<11.81 μs, C_{high}=2690+229($D_2–D_1–11.81$)

$D_2–D_1$>11.81 μs, C_{high}=2690

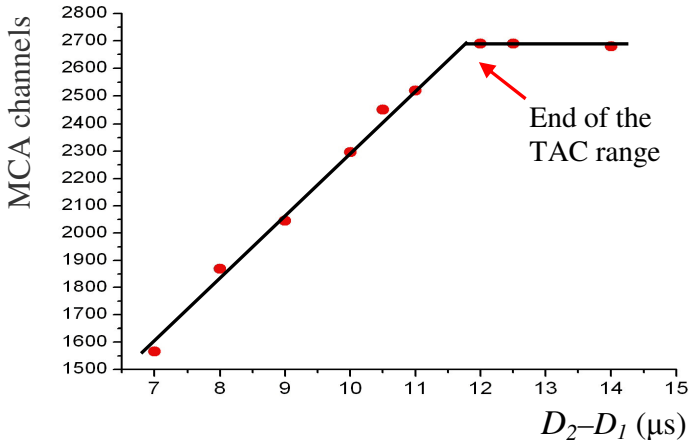

Figure 5.3 Dependence of the upper limit of scintillator spectra as a function of $D_2–D_1$ measured in μs. The fit gives an end point at 11.81 μs and channel 2690.

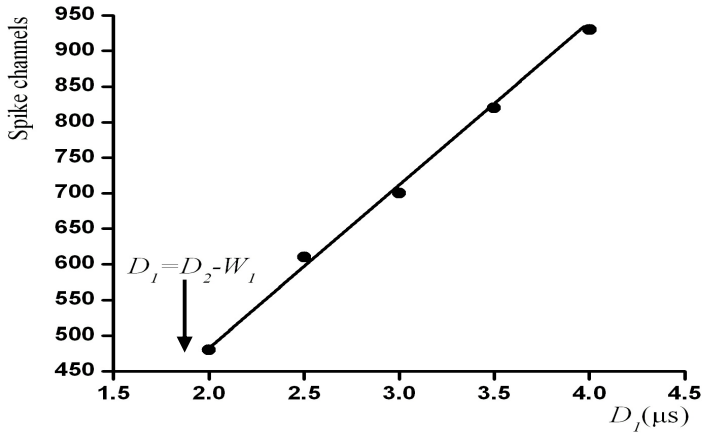

Figure 5.4 Dependence of the spike position on D_1.

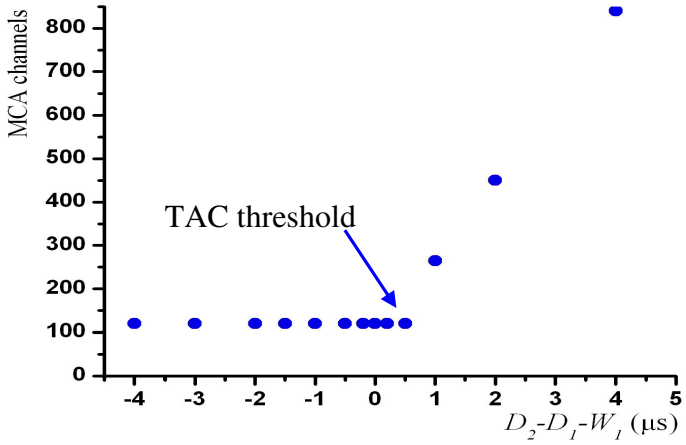

Figure 5.5 Dependence on $D_2–D_1–W_1$ (μs) of the lower limit of scintillator spectra. The best fit gives an end point at 0.60 μs and channel 120.

Here, we calculated the scale of 229 channels per microsecond by simply dividing $C_{high}–C_{low}$ =2690–120=2570 by 11.81–0.6=11.21 μs. Namely we assumed a linear relation between channel and time. This result can be extended to the general case, where we assume the pedestal C_{ped} to be run-dependent in an apparently random fashion. For a time difference δt between the stop and start signals, we measure a channel C such that:

If $D_2–D_1–W_1< 0.6$ μs, $C_{low}= C_{ped}$

$D_2–D_1–W_1> 0.6$ μs, $C_{low}= C_{ped} +229(D_2–D_1–W_1–0.6)$

$D_2–D_1<11.81$ μs, $C_{high}=2570+ C_{ped}+229(D_2–D_1–11.81)$

$D_2–D_1>11.81$ μs, $C_{high}=2570+ C_{ped}$

On the low side, we measure $Max(0, D_2–\delta t–0.60)$ and on the high side $Min(D_2–\delta t ,11.81)$.

For 0.6 μs $<D_2–\delta t<11.81$ μs,

$C=C_{ped}+229(D_2–\delta t–0.6)=C_{ped}+2570+229(D_2– \delta t –11.81)$

For 0.6 μs$>D_2–\delta t$, $C=C_{ped}$

For $D_2–\delta t>11.81$ μs, $C=2570+C_{ped}$

We assumed that the relation between channel and measured signal is linear with an average slope of 229 channels per microsecond, but in reality it is not. This non-linearity is studied below.

5.1.2 Calibration

In order to check the proper performance of the electronics and to calibrate the TAC and MCA, a special circuit has been assembled. Its diagram is shown in Figure 5.6. A NIM pulse generator operated at 1 kHz frequency is used as input to a timing unit used to delay the pulse by an adjustable quantity. The original and delayed pulses are OR'ed and sent to the input of the fan-out unit at the front end of the electronics that prepares the start and stop signals (Figure 5.1). Results of the calibration are shown in Figure 5.7 where

D_1 = 1.0 μs, W_1=10 μs and D_2 =11.5 μs. A second degree polynomial fit gives $\delta t =\delta t_0–N(1+N/20322)/259.1$ where δt is the delay between the two pulses

and N is the associated number of MCA channels. Namely, for N=2570 channels, the second term is 11.2 μs, in excellent agreement with 11.81–0.6=11.2 μs. We therefore retain, in the authorised range, 0.6 μs<D_2–δt<11.81 μs

$$\delta t = D_1 + W_1 + 0.5 - 0.6 - (C - C_{ped})(1 + (C - C_{ped})/20322)/259.1$$

In most data, W_1=10 μs. When such is the case, we may rewrite

$$\delta t = D_1 + 9.9 - (C - C_{ped})(1 + (C - C_{ped})/20322)/259.1.$$

Note that δt=9.9 μs for C–C_{ped}= 2300 channels; hence the procedure:

Measure the highest and lowest spectrum channels, C_{high} and C_{low}. Check that C_{high}–C_{low}=2300 to better than ~1%. Correct C_{high} and C_{low} by opposite amounts to have C_{high}–C_{low}=2300 exactly. Then equate C_{ped}=C_{low} and calculate δt using the relation $\delta t = D_1 + 9.9 - (C - C_{low})(1 + (C - C_{low})/20322)/259.1$.

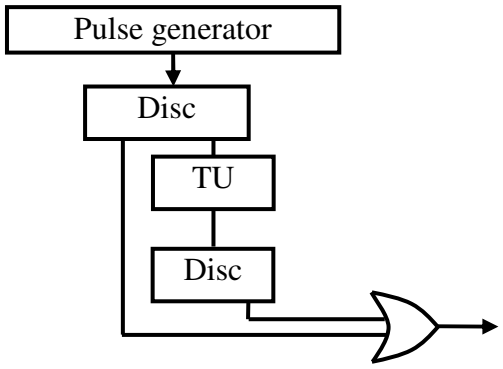

Figure 5.6 Logic diagram for the calibration.

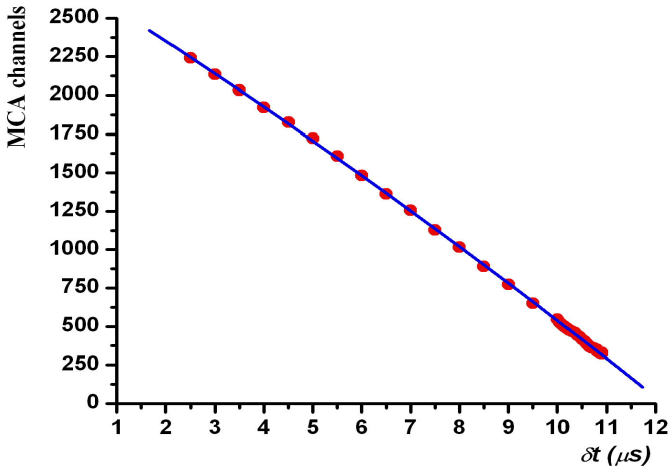

Figure 5.7 Calibration curve of the TAC+MCA system.

For $D_2=D_1+W_1+0.5$ and $W_1=10$, we can rewrite this result for different values of D_2 as follows:

$$\delta t=D_2-0.6-(C-C_{ped})(1+(C-C_{ped})/20322)/259.1$$

From the calibration data, we obtain an estimate of the uncertainty on the time measurement of 60 ns.

5.1.3 Spikes

At low threshold or for small D_1, the MCA spectrum displays two spikes in the region of δt=5 µs. An example is shown in Figure 5.8.

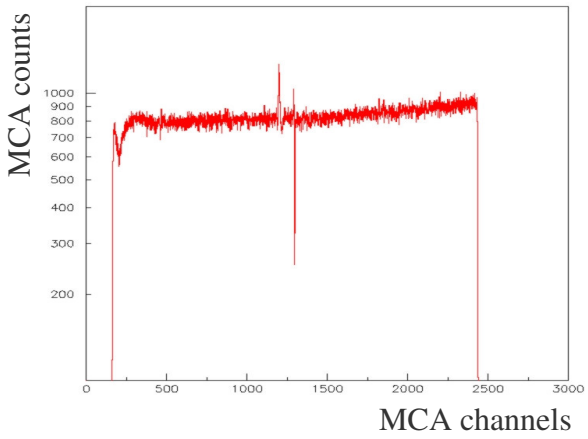

Figure 5.8 Cherenkov spectrum measured for D_1=5 µs. The abscissa had been shifted by 696 channels, so the spikes occur in reality around channel 1900 corresponding to δt ~5 µs.

A systematic survey shows that the occurrence of such spikes depends only on the value of D_1 but requires D_2 to be smaller or just slightly larger than D_1+W_1. This suggests that spikes are associated with configurations where a second pulse arrives between D_1+W_1 and D_2 after the first pulse as illustrated in Figure 5.9.

When $D_2<D_1+W_1$, one may have a pulse coming at δt in-between D_2 and D_1+W_1. This pulse will give a start. However, it comes after the stop and does not generate a TAC signal. Unless, for some reason, a stop is generated by the leading edge of TU1, i.e. after D_1. Then one has a stop at D_2+D_1 and measures

$D_2+D_1-\delta t$. For $\delta t<D_2$, one has the normal behaviour. Namely one measures $D_2-\delta t$. For $\delta t= D_2$ one measures 0 in the normal case and D_1 in the abnormal case. Therefore, as far as the spectrum is concerned, the situation is as follows:

$0<\delta t<D_1$ no TAC signal;

$D_1<\delta t<D_2$ one measures $D_2-\delta t$, going from D_2-D_1 to 0 (in fact to the MCA threshold);

$D_2<\delta t<D_1+W_1$ one measures $D_2+D_1-\delta t$, going from D_2-W_1 to D_1 under the condition that the leading edge of TU1 generates a D_2.

The spike occurs when $\delta t=D_2$.

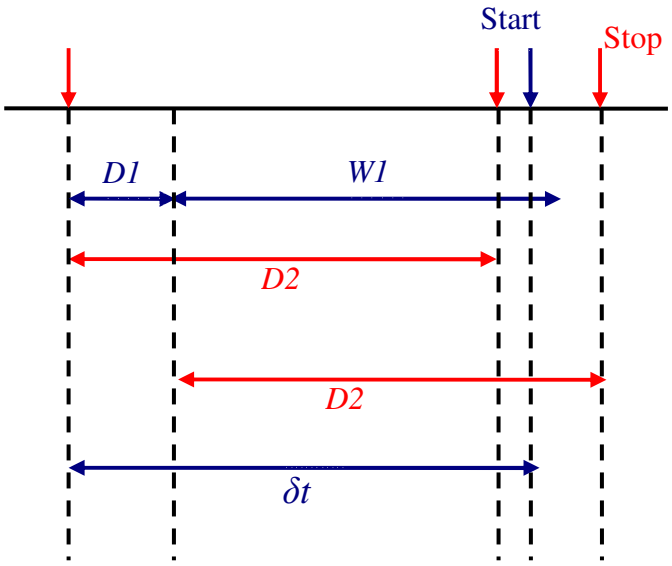

Figure 5.9 Configuration in which a spike may occur.

We tried to reproduce this situation with the double pulse generator but did not succeed, implying that the occurrence of spikes requires in addition some abnormal behaviour not reproduced by the double pulse generator.

We checked that the presence of such spikes is, however, harmless to the data analysis by remarking that, when they occur, it is in the region where the time spectrum is flat and, moreover, their area cancels. This is illustrated in Figure 5.10 where one sees that the spikes are essentially independent from threshold and in Figure 5.11 which shows that their area cancels: fits to a spectrum showing a spike give the same result whether the spike is included in or excluded from the fit.

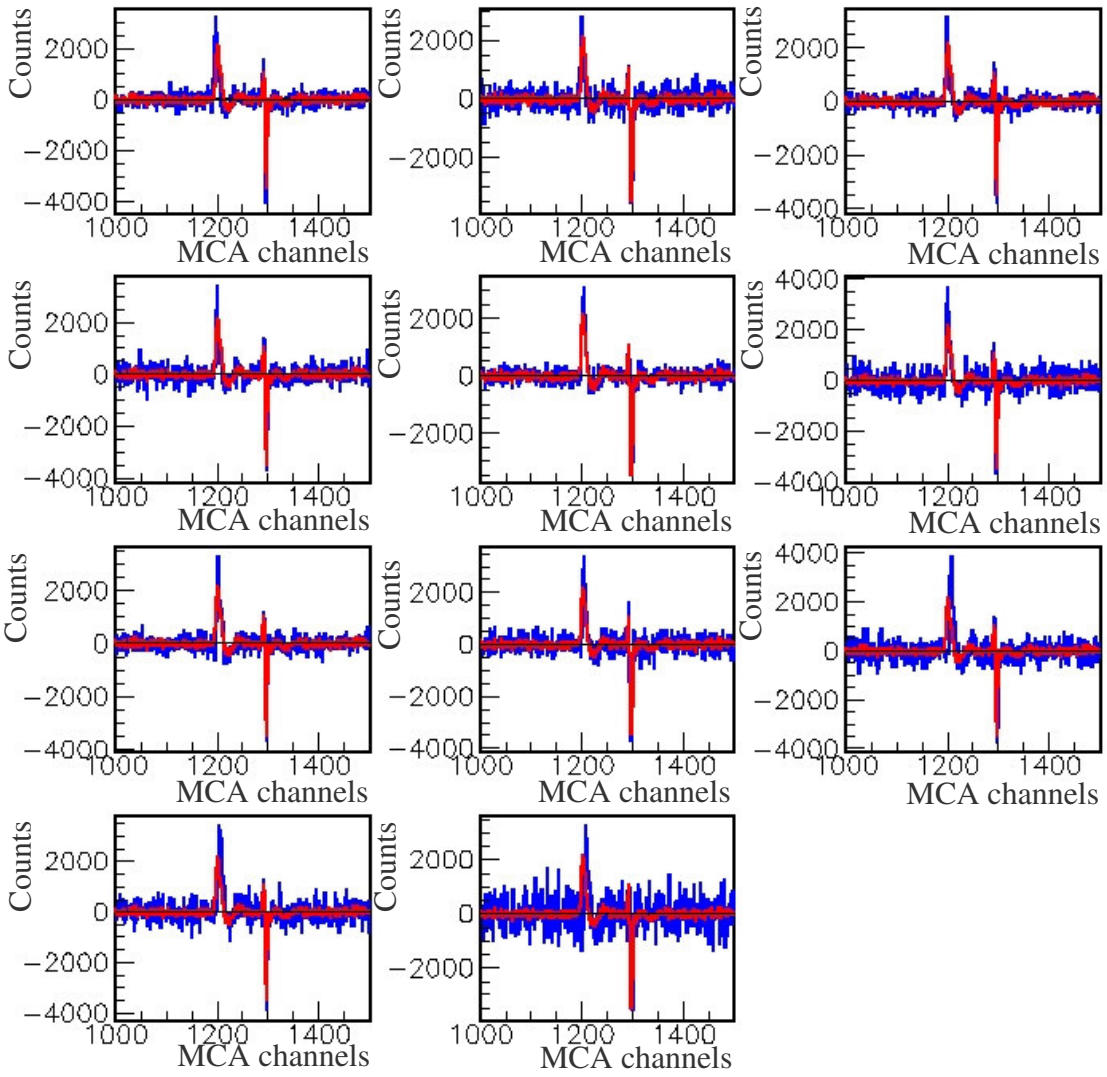

Figure 5.10 Eleven Cherenkov MCA spectra are shown (in blue) in the spike region for a common D_1 value but different thresholds (here D_2=15.5 μs, D_1=5.0 μs, W_1=10.0 μs). The red curve is their average distribution.

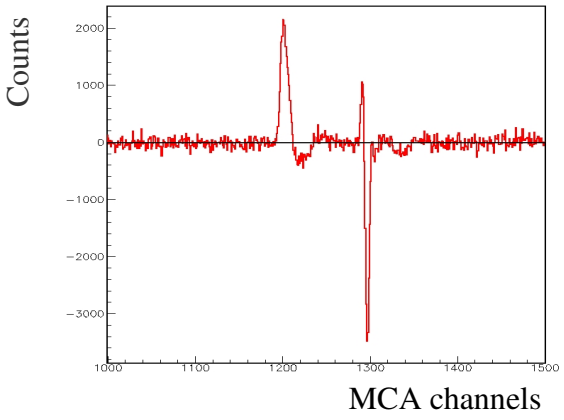

Figure 5.11 Average spike from the spectra displayed in Figure 5.10. Its area cancels to better than 1%.

5.2 Charge measurement

The charges of both the hodoscope scintillator signals and Cherenkov signals are recorded in a single ADC activated by three possible gates. The diagram of the associated electronics is shown in Figures 5.12 and 5.13. A first gate is generated by the start signal, namely the second signal of a correlated pair; a second gate is generated by a clock made of a fed-back timing unit and is used to measure pedestals; the third gate is generated by a coincidence between the four scintillator plates of the hodoscope. All three gates are converted to a common broad gate, an essential requirement in order to be able to have a common charge scale and to perform the VEM calibration properly. The timing of the gate with respect to the signals being analysed has been carefully adjusted to ensure that the signals are in all cases well contained within the gate. Pattern units are used to tell which trigger was active.

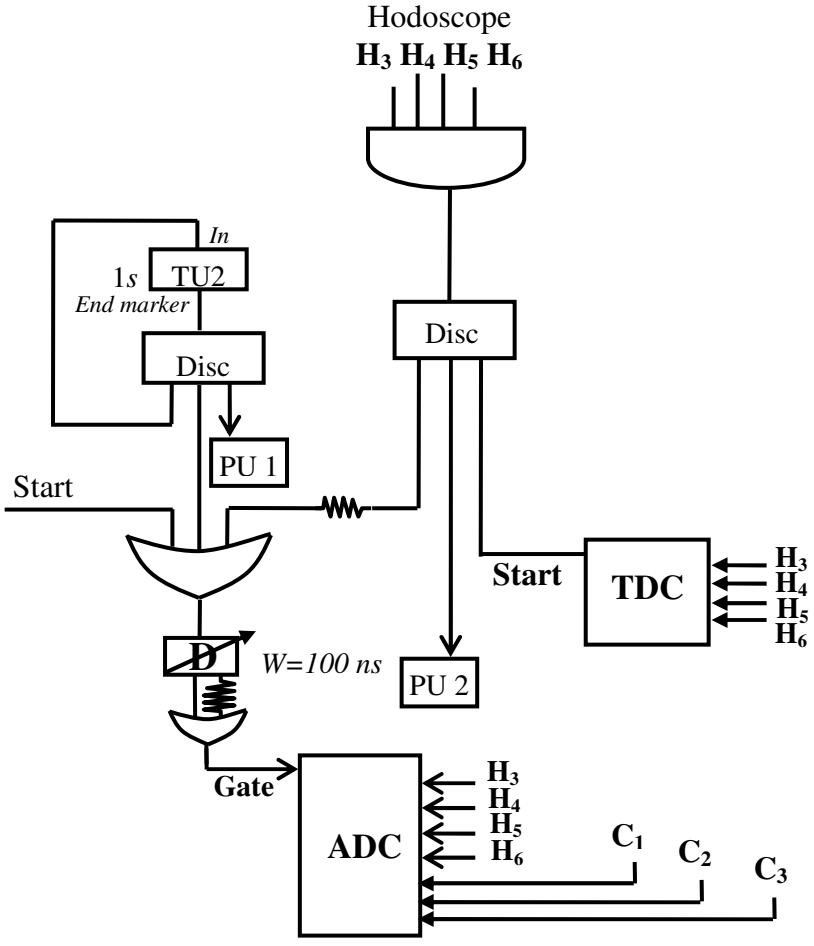

Figure 5.12 Diagram of the electronics used for the charge measurement.

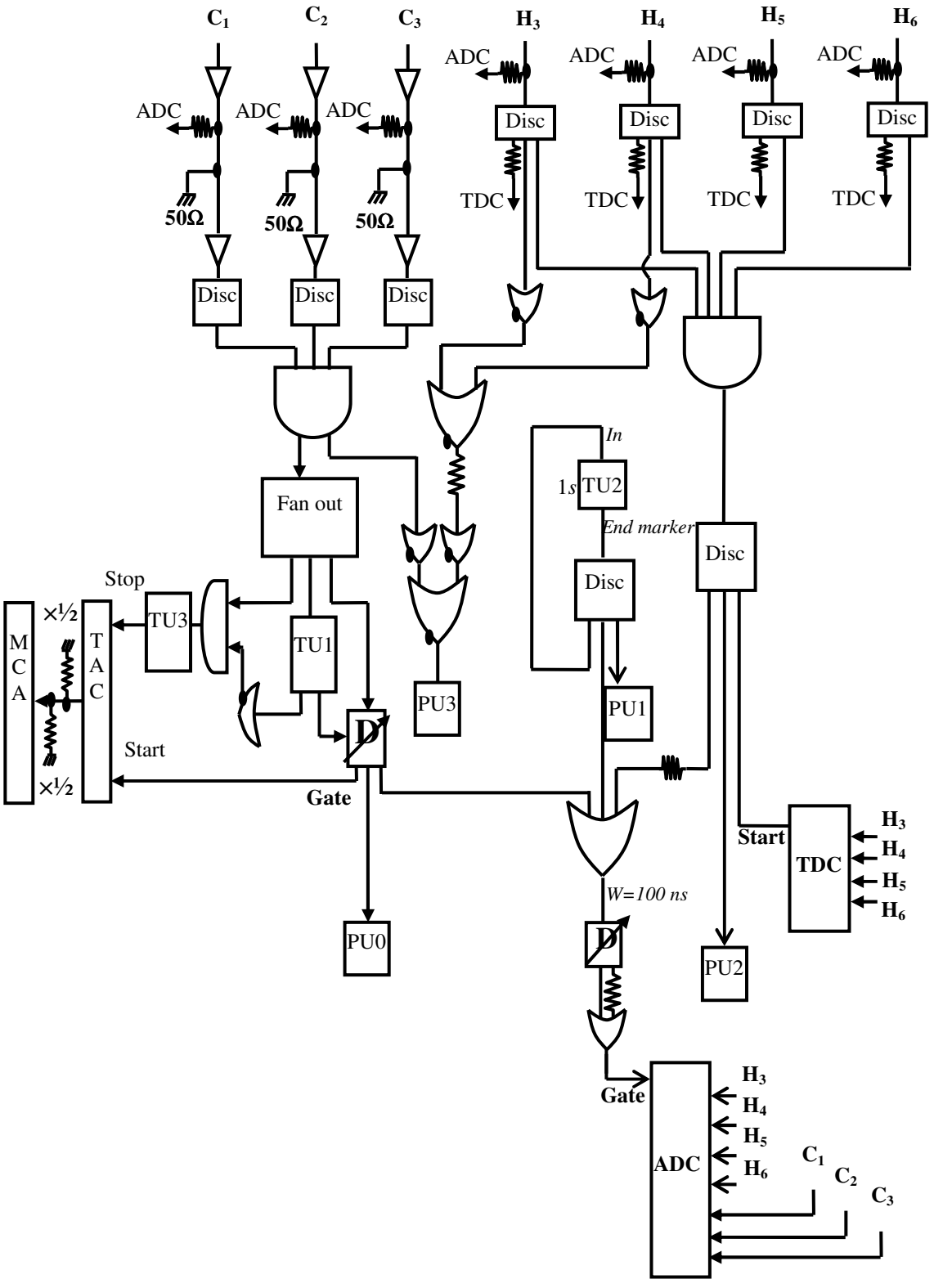

Figure 5.13 General diagram of the NIM logic electronics.

6. Auto-correlations: data analysis

The present section presents the result of the analysis of data collected using the experimental set-up described in the preceding sections, namely the main Cherenkov detector and its trigger hodoscope used for calibration. In addition, it includes the analysis of data collected using a simple scintillator detector assembled in order to provide a reference with which the main Cherenkov data can be compared. The scintillator detector has an area of 120×40 cm^2 and is described below (sub-section 6.1.3).

Multiple muon events (from a same shower) are expected to be less numerous in the scintillator case than in the Cherenkov case, in a ratio equal to that of the detector area, namely ~1/30. In the Cherenkov case, they may give a contribution that competes with the decay electrons. Indeed, while stopping muons give a large signal in the scintillator at the end of the Bragg curve and decay electrons deposit ~50 MeV on average, namely four times more than feed through muons, on the contrary, in the Cherenkov case, stopping muons stop emitting Cherenkov light before stopping and electrons are known to emit of the order of one tenth of the light emitted by feed-through muons. The scintillator geometry allows for ignoring muons from a same shower and gives a reference with which to compare the Cherenkov data.

6.1 TAC spectra

6.1.1 Introduction

Auto-correlation spectra have been measured over a time range T_{range}=10 μs while the rate R is of the order of 200 particles per m^2 per second, namely ~100 Hz in the scintillator detector case and ~2 kHz in the Cherenkov detector case, corresponding to decay times of 10 ms and 500 μs respectively: R contributes a nearly flat background. We expect muon rates of the order 2 kHz and detected electron rates of the order of 0.4 Hz in the Cherenkov case. In the scintillator case, the muon rate is at the 100 Hz level and the probability to have a

second muon in the TAC range is therefore ~10^{-4} while the probability to have a stopping muon is at the per mil level, an order of magnitude larger.

6.1.2 Cherenkov spectra

A total of 92 time spectra have been collected, of which 62 are of Cherenkov data. We first estimate the values c_1 and c_2 of the MCA low and high channels and evaluate the value of W_1 from relation $W_1=t_2-t_1$ where t is calculated from the corresponding channel c using the formula given in Section 5.1.2:

$$t=D_2-0.6-(c_2-c_1)(1+(c_2-c_1)/20322)/259.1$$

and display it in Figure 6.1. The distribution is very narrow with a mean value of 9.98 μs and an rms value of 0.06 μs. However, the observed spread is associated with different sequences of data collection, each peak corresponding to a same sequence. We conclude therefore that our measurements of c_1 and c_2 are reliable and retain for W_1 the value calculated rather than the nominal value of 10 μs. We retain for D_1 its nominal value. The uncertainty on D_1 must be at least equal to the 0.6% relative uncertainty measured for W_1 (half a graduation on the scope screen) but it also receives absolute contributions (pulse width, rise time, etc) at the scale of ~10 ns which are more important. We retain for it an estimate of 0.2 μs.

For each bin i of spectrum j we calculate a time δt corrected for the TAC non linearity as described in Section 5.1.2. We also correct the number of counts in each bin for non linearity as, at large channels (small δt), the number of microseconds per channel is larger than at small channels (large δt): we obtain this way a measurement of dS/dt accounting for the fact that the bin size is affected by the non linearity.

When spikes occur, they are replaced by linear interpolation between the ten lower and ten upper neighbour channels.

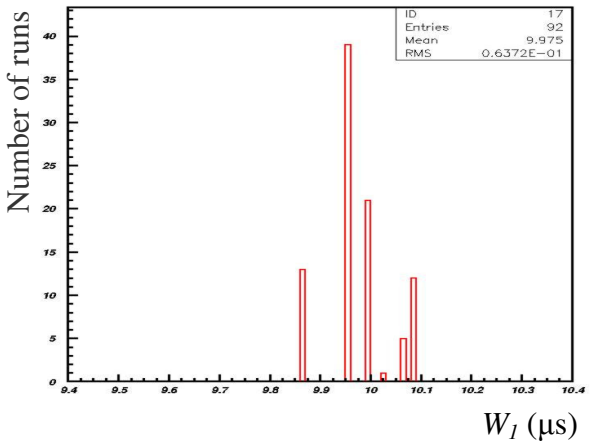

Figure 6.1 Distribution of the measured value of W_1 for Cherenkov runs where the nominal value is 10 μs. The mean value is 9.98 μs and the rms value is 0.06 μs.

We then fit together the 62 spectra to the sum of four exponentials. Each spectrum is fit between times dt_1 and dt_2, evaluated separately by eye for each spectrum to avoid end effects.

The sum of four exponentials read:

$$Rexp(-R\,\delta t)+g_0R_{sh}exp(-R_{sh}\delta t)+\varphi\rho_+R_+exp(-R_+\delta t)+\varphi\rho_-R_+exp(-R_-\delta t).$$

Here, $\rho_+=1-\rho_-$, ρ_- , R, R_+ and R_- are fixed to their known values. We recall their respective meanings: ρ_+ and ρ_- are the fractions of positive and negative muons, R is the cosmic muon rate, R_+ is the muon decay rate in vacuum and R_- is the disappearance rate of negative muons, including both decays and capture in water. The fitted parameters are g_0 and R_{sh} for the multimuon contribution and $\varphi=f_{stop}\eta$ for the electron contribution. While f_{stop}, the fraction of stopping muons is the same for all runs, η, the electron detection probability, depends on threshold. As seven different threshold values have been used, the total number of parameters to be adjusted is 9. The seven φ parameters correspond to thresholds of respectively 0.525, 0.7, 1.0, 1.5, 2.0, 2.5 and 3.0 threshold units. A threshold unit (t.u.) corresponds approximately to 100 mV.

We expect a muon rate of ~2 kHz and an electron rate at the scale of 0.5 Hz to 1 Hz at zero threshold and for full detection efficiency (see Table 3.1), meaning φ ~250 to 500 ppm. As we shall see below (Figure 6.6), φ~120 ppm at a threshold of 0.5 t.u. and the curve has not yet reached its turning point. Assuming

that a 0.5 t.u. threshold cuts 50 to 70% of the events, the value at zero threshold would be 240 to 400 ppm, meaning a reasonable detection efficiency.

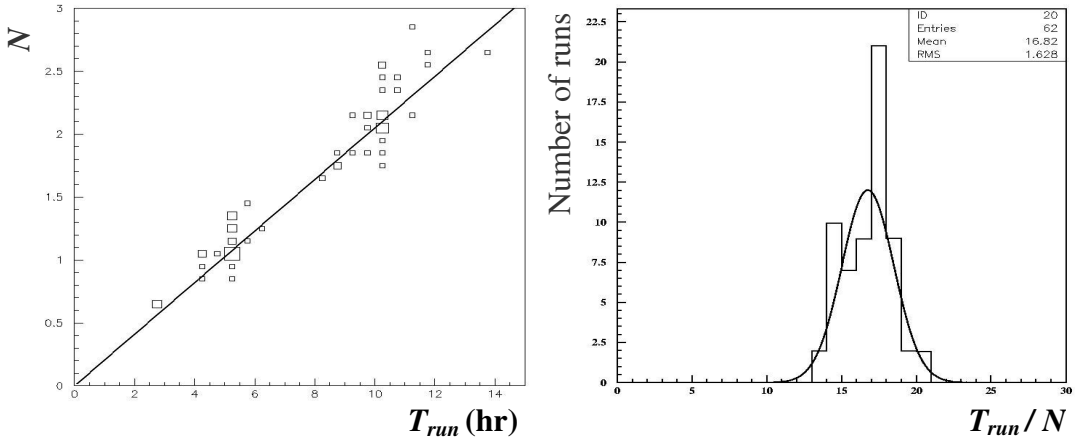

Figure 6.2 Correlation between the normalisation constant and the running time: 2-d plot (left) and distribution of their ratio (right).

The total number of events in each spectrum is normalized to a common value between data and model. The normalization constant, N, is in principle proportional to the duration of the measurement, T_{run}. A check of this relation is displayed on Figure 6.2. It is found to be obeyed to a precision better than 10%. Indeed, the value of R has been recorded at the beginning of each run with only such a precision. While excellent fits have been obtained when using the recorded values of R, slightly smaller χ^2 values could be achieved by using a threshold-dependent rate evaluated from the best fit N to T_{run} ratio:

$$R' = 57.9 - 38.0\, x_{thr} + 10.9\, x_{thr}^2 + 1.20\, x_{thr}^3 .$$

These values have therefore been used in the fit rather than the recorded R values.

The χ^2 of the fit is calculated using statistical errors exclusively. The results of the best fit are listed in Table 6.1 and illustrated in Figures 6.3 to 6.5. Moreover, we noted that the quality of the fit was improved by allowing for a drop in the muon detection efficiency for thresholds exceeding 2 t.u.. The best fit gives a muon detection efficiency of 38±3% at 2.5 t.u. and of 13±2% at 3 t.u..

The value of the best fit χ^2 is 1.020 per degree of freedom (of which there are 118'185), providing evidence for the quality of the fit and for negligible

systematic errors. Figure 6.3 shows the distribution of the ratio between measurements and model, with the best Gaussian fit having a σ of 5.3%.

Figure 6.4 illustrates the agreement between measurement and model for each threshold value separately. The measured electron contribution is compared with the model in Figure 6.5, showing very good agreement with the nominal muon life time. Figure 6.6 displays the dependence of φ on threshold. As expected, the sensitivity to electron detection drops to zero when the threshold reaches its higher values.

The best fit value of parameter g_0 is $(0.79\pm0.05)\times10^{-5}$ for a decline time of 1.13±0.04 μs.

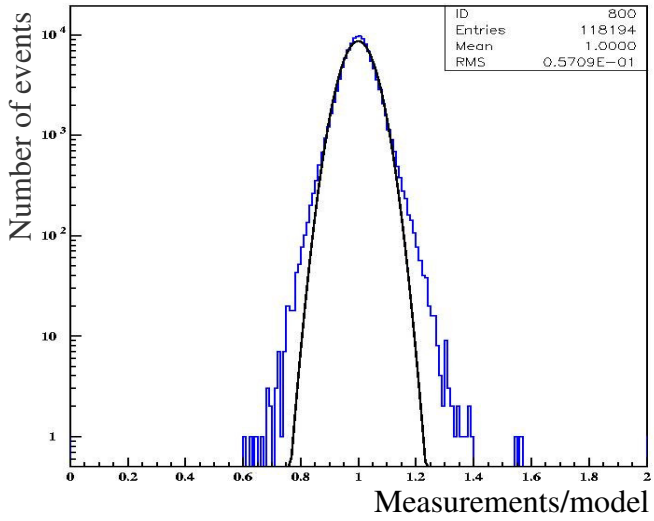

Figure 6.3 Distribution of the ratio between measurements and model for the best fit.

Table 6.1 Best fit results of the Cherenkov spectra to a form $Rexp(-R\,\delta t)+g_0R_{sh}exp(-R_{sh}\delta t)+\varphi\rho_+R_+exp(-R_+\delta t)+\varphi\rho_-R_+exp(-R_-\delta t)$.

χ^2/dof	1.020
$g_0\,(10^{-5})$	0.79± 0.05
$R_{sh}\,(\mu s^{-1})$	0.89±0.03
$\varphi_1\,(ppm)$	123±0.7
$\varphi_2\,(ppm)$	88±0.6
$\varphi_3\,(ppm)$	65±0.6
$\varphi_4\,(ppm)$	19±0.5
$\varphi_5\,(ppm)$	1.3±0.5
$\varphi_6\,(ppm)$	<0.01
$\varphi_7\,(ppm)$	<0.02

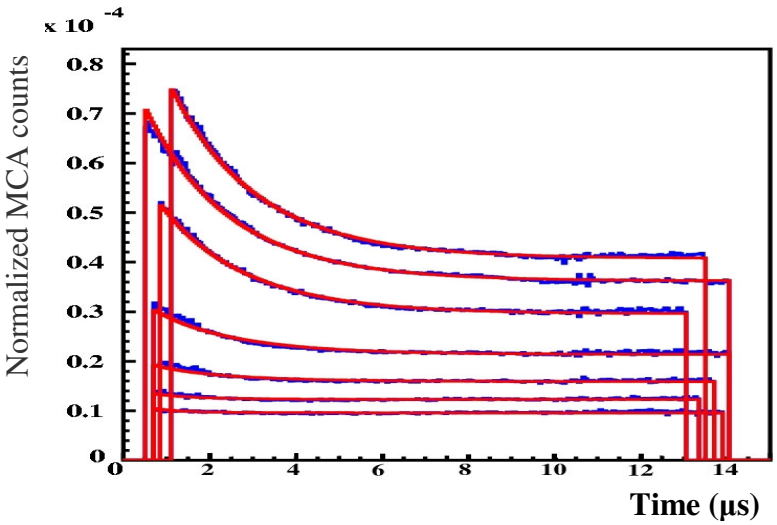

Figure 6.4 Measured Cherenkov autocorrelation spectra (blue) are compared with the result of the best fit (red) for different thresholds (0.525, 0.7, 1.0, 1.5, 2.0, 2.5, 3.0 t.u. from up to down). In most cases the blue curve is hidden behind the red curve.

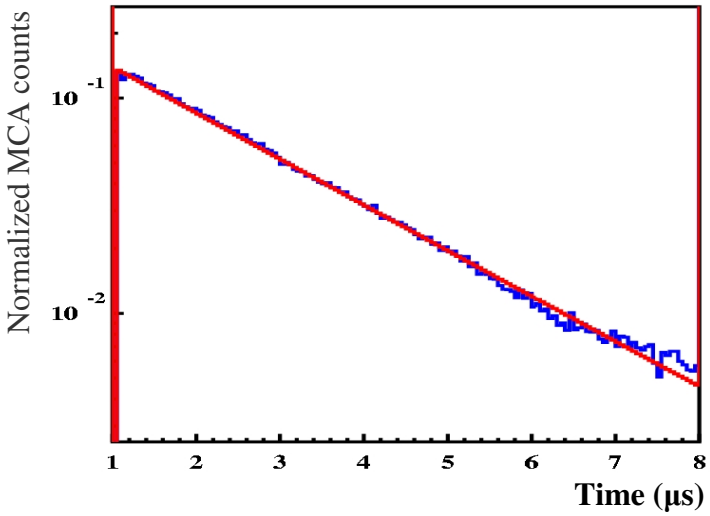

Figure 6.5 Measured electron contribution compared with the best fit model prediction. In most bins the blue curve is hidden behind the red curve.

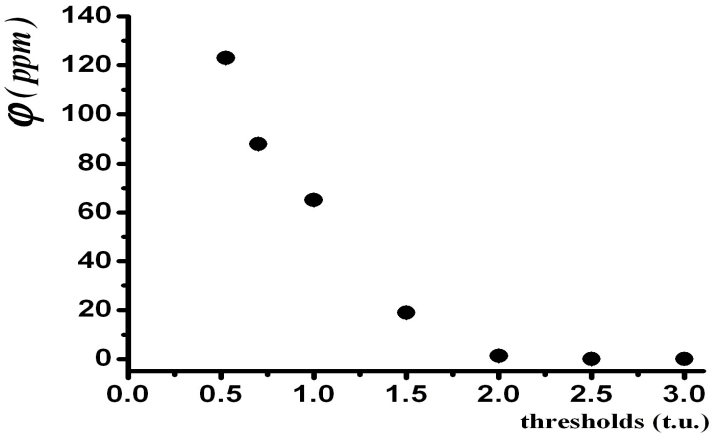

Figure 6.6 Dependence of φ on threshold. Error bars are smaller than the data points.

6.1.3 Scintillator detector

Two different arrangements have been used, one using a single scintillator plate, the other using two. In both cases the plates, 120×40×3 cm^3, are made of PVT (Polyvinyl Toluene, NE114). They were manufactured over forty years ago for an early neutrino experiment at CERN and were given to us as a gift. They are seen by 2" 12-dynode PMTs through simple lucite light guides glued on the plate sides. In the two-plate geometry, the plates are in optical contact via a thin film of vaseline oil and each plate is seen by a single PMT at opposite sides; in the single plate geometry, both PMTs are looking from a same side (Figure 6.7). As a result of ageing, the scintillators have short attenuation lengths and the amount of light detected depends on the distance to the PMTs. In the two-plate geometry, this implies a maximal efficiency in the middle of the plates and in the single plate geometry, a maximal efficiency at the closer end.

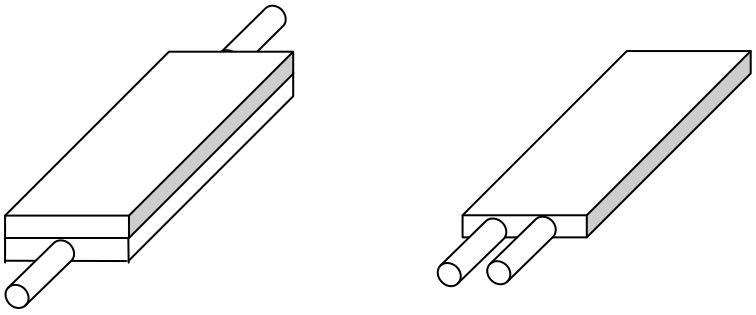

Figure 6.7 Scintillator detectors geometry: two-plate (left) and single plate (right).

Auto correlation spectra have been collected using different thresholds and D_1 values, but a common W_1 value of 10 μs. Fits have been made to a model neglecting the possible detection of a second muon from a same shower and the occurrence of muon capture, both effects being expected to be negligible. A common, unexpected feature of the data collected in each of the two geometries is the presence of a strong short life time component having a decay time of the order of half a microsecond. The data do not allow for an unambiguous identification of what causes it, but it resembles a fluorescence emission excited by the primary particle with low probability but high intensity, such that it is well

described by a single exponential proportional to the muon term. In practice, each spectrum has been divided by the associated running time and fit to a form

$f_\mu(1+k\exp(-t/T_{fast})/T_{fast})+f_{el}\exp(-t/T_{dec})/T_{dec}$ where k and T_{fast} characterize the relative amplitude and decay time of the short life component, f_μ is a threshold dependent quantity proportional to the detection efficiency of stopping muons, f_{el} is the detection efficiency of muon decay electrons and T_{dec} is the muon decay time in vacuum, fixed at its known value. The running times were allowed to vary within measurement uncertainties of 10%.

Good fits are obtained in each geometry. They are illustrated in Figures 6.8 and 6.9. In the single plate geometry, the detection efficiencies of both muons and electrons are nearly constant, displaying only a small drop at the higher threshold (4 t.u.), 10% for muons and 3% for electrons. On the contrary, in the two-plate geometry, both electron and muon detection efficiencies depend strongly on threshold, in a way well described by linear forms $f=f_0-f'V$ where V is the value of the threshold in threshold units. Normalising $f_\mu=1$ for muons at zero threshold, we obtain the following results:

Single plate geometry:

$f_\mu=1$ and $f_{el}=1.88\pm0.04$ for $V<3$ t.u., $f_\mu=0.90\pm0.14$ and $f_{el}=1.83\pm0.08$ for $V=4$ t.u.

Double plate geometry:

$f_\mu=1-(0.143\pm0.002)V$ and $f_{el}=(11.9\pm0.3)\{1-(0.097\pm0.007)V\}$

The short life component has $k=37.0\pm0.9$ in the double plate geometry and 9.39 ± 0.07 in the single plate geometry. The respective values of T_{fast} are 0.403 ± 0.006 and 0.519 ± 0.004 μs.

As noted earlier, we expect f_{el} to exceed f_μ by approximately one order of magnitude, which is the case at zero threshold in the double-plate geometry. In the single plate geometry, this number is ~6 times smaller, resulting both from the lower stopping probability (typically a factor 3 when allowing for a reasonable fiducial volume) and the lower containment of the electron shower.

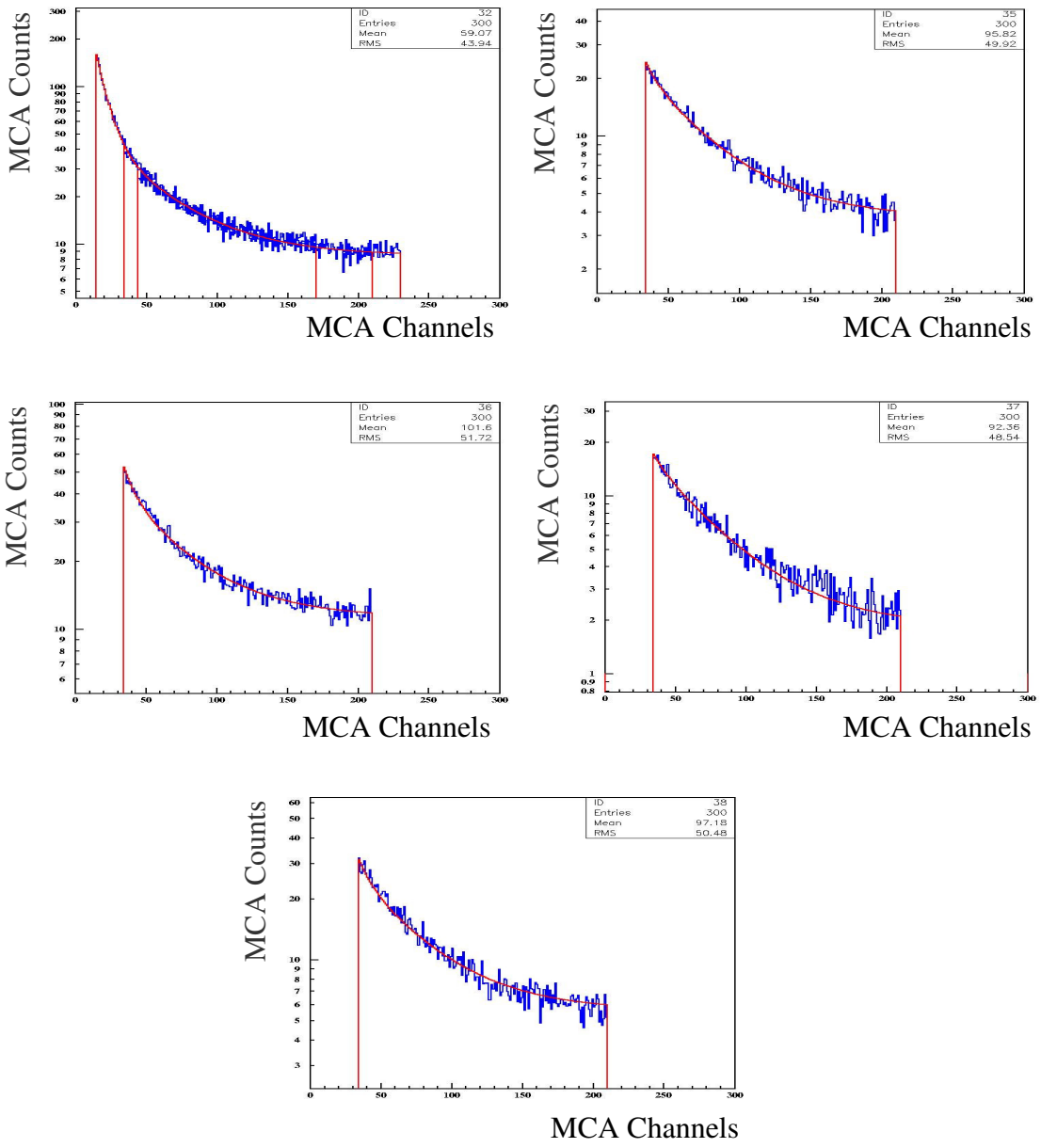

Figure 6.8 Measured scintillator spectra (double-plate) are compared with the result of the best fit for different thresholds (2.5, 5, 1, 6 and 4 t.u.)

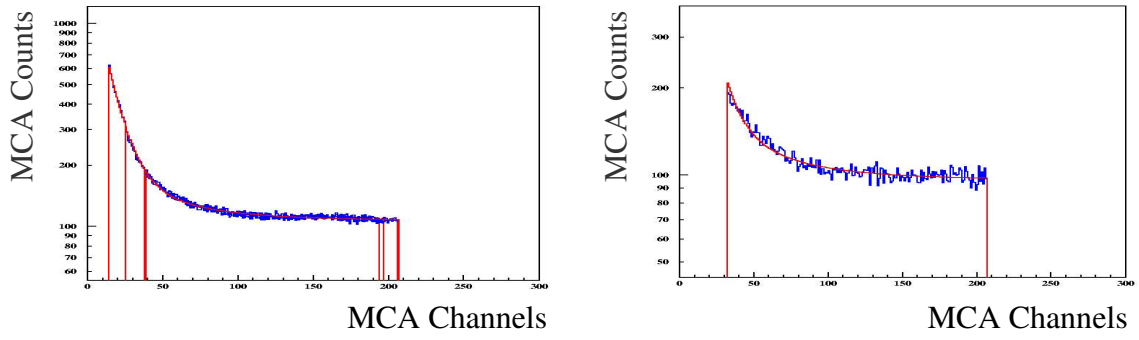

Figure 6.9 Measured scintillator spectra (single plate) are compared with the result of the best fit for different thresholds. The left figure contains 4 spectra having thresholds of 1 and 2 t.u.. The right panel corresponds to a threshold of 4 t.u..

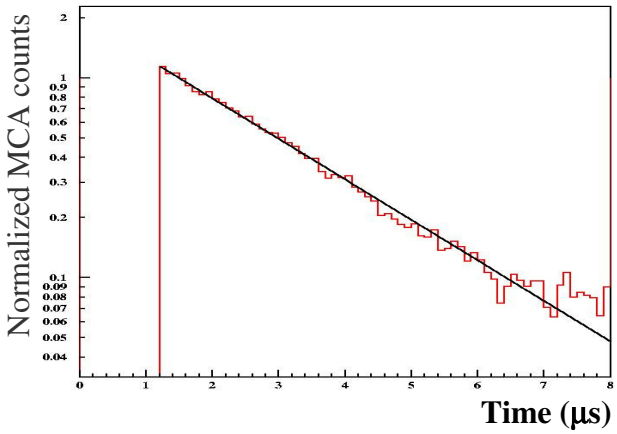

Figure 6.10 Muon decay curve for the scintillator data.

Combining all scintillator spectra together gives the muon decay curve displayed in Figure 6.10. The best fit decay time is 2.14±0.03 μs compared with 2.197 μs in vacuum: the data can accommodate a capture rate of 1/2.14 –1/2.197 $=(1.2\pm0.6)\times10^{-2}\ \mu s^{-1}$ while the capture rate in carbon [19] is $(3.79\pm0.05)\times10^{-2}\ \mu s^{-1}$; multiplied by the 44% fraction of μ^- [20], it gives a capture rate of $(1.67 \pm 0.02)\times10^{-2}\ \mu s^{-1}$, compared with $(1.2\pm0.6)\times10^{-2}\ \mu s^{-1}$ measured here.

6.2 Charge spectra

6.2.1 Introduction

The second signal of a correlated pair, of which the charge is recorded in the ADC, is either an electron (requiring that the first signal was a detected stopping muon) or a muon (minimum ionising in most cases). Both components depend in different ways on threshold and delay. Analysing data collected at different thresholds and delays should therefore allow disentangling the respective contributions of electrons and muons to the recorded charge distributions. The present section addresses this problem.

6.2.2 Cherenkov detector

A total of 57 runs have been recorded, of which three have been ignored because the Cherenkov PMT high voltage was unstable. Merging runs having same threshold and D_1 values leaves a total of 48 runs of which 5 are taken with different PMT high voltages and are discarded. Another one shows evidence for

instabilities resulting in an important smearing of the charge distribution and is also discarded.

We use the hodoscope trigger data (bracketing the Cherenkov tank) to scale the 42 remaining runs to a common VEM value of 325 ADC channels. The result is shown in Figures 6.11 and 6.12, which display the mean values, and respectively rms values, of the recorded Cherenkov spectra. The superposition of all normalised spectra is illustrated in Figure 6.13 for PMT1, PMT2 and (PMT1+PMT2)/2 separately. The rms to mean ratio for the latter is now ~26%, corresponding to 14 to 15 photoelectrons per VEM. The value obtained for three PMTs (Section 2, Figure 2.18) was 20±1, which would mean 13.3±0.7 for two PMTs. We therefore retain 14±1 photoelectrons per VEM as our best estimate for the present data.

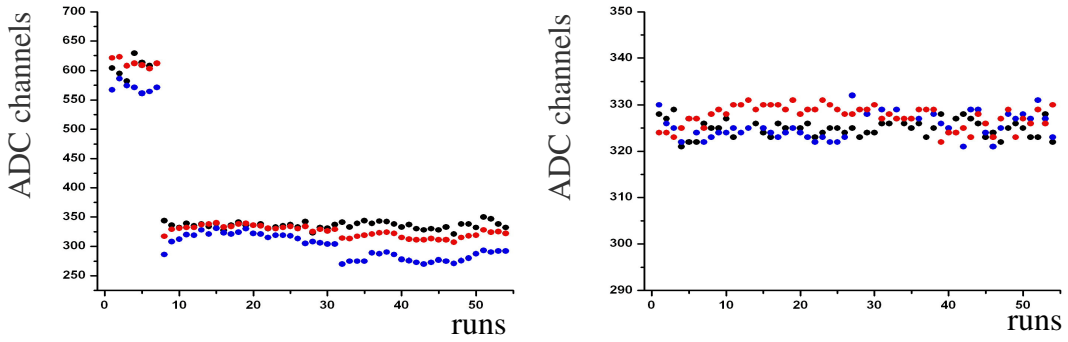

Figure 6.11 VEM calibration: distribution of the mean charge measured in PMT1 (black), PMT2 (blue) and their average (red) as a function of run number. Data are plotted before merging and include the early runs with different PMT high voltages. The left panel is before scaling and the right panel after.

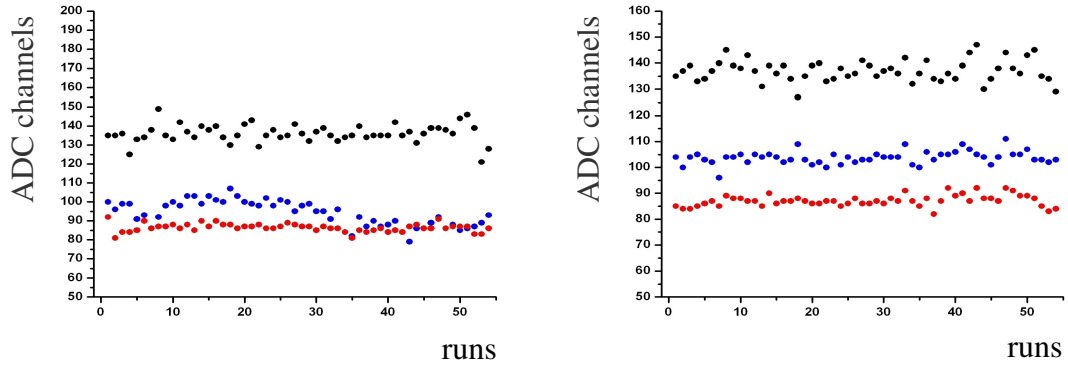

Figure 6.12 VEM calibration: distribution of the rms charge measured in PMT1 (black), PMT2 (blue) and their average (red) as a function of run number. Data are plotted before merging and include the early runs with different PMT high voltages. The left panel is before scaling and the right panel after.

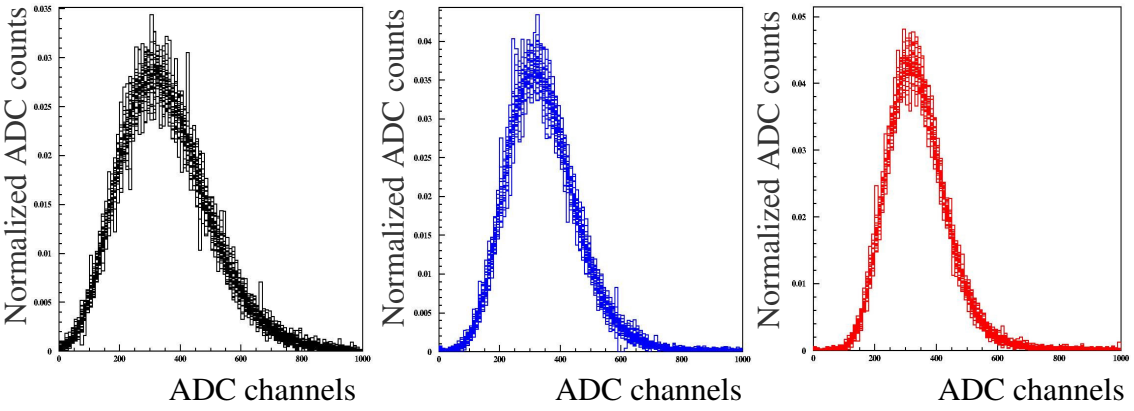

Figure 6.13 VEM calibration: superposition of all normalised spectra for PMT1 (black), PMT2 (blue) and their average (red).

Having fixed the charge scale using the VEM calibration described above we now compare the data with a dependence on threshold and delay having the following form:

$$S_{ijk} = N_{ij}\left\{F_k^{\mu} + \lambda_i \, exp(-D_j/\tau)F_k^{el}\right\} \qquad (6.1)$$

Here i labels the threshold, j the delay and k the charge bin. N_{ij} is a normalisation constant, one for each spectrum; λ_i accounts for the fact that when the threshold increases, so does the fraction of stopping muons (the threshold applies to both the start and stop signals) and therefore of possibly detected decay electrons; the exponential term accounts for the exponential decrease of the electron contribution as a function of delay (D_1, here written D_j to account for its different values and τ is taken equal to 2 μs in order to account for capture); C_i describes the cut-off at low charges due to the discriminator threshold.

Rather than fitting the normalisation constants for each independent charge distribution, we set it to unity and normalise the measured distributions in the high charge region where electrons do not contribute. The data normalised in this fashion are displayed in Figure 6.14 (left).

The cut-off function C_i is taken of the form $(1+exp[-(x-x_{ci})/\Delta_{ci}])^{-1}$ where x_{ci} and Δ_{ci} are proportional to threshold: $x_{ci}=a_c th_i$, $\Delta_{ci}=b_c th_i$, th_i being the nominal threshold value. It switches from 0 to 1 around $x=x_{ci}$ over a width measured by Δ_{ci}. We find that this form describes well the data to a precision of ~0.06 VEM. The best fit values of a_c and b_c are 0.18±0.02 VEM and 0.042±0.001 VEM respectively.

The best fit values of the λ parameters are displayed in the right panel of Figure 6.15 as a function of threshold and listed in Table 6.2. Above a threshold of 2 threshold units, electrons do no longer contribute. The sharp decrease of the λ parameters as a function of threshold illustrates the difficulty of the measurement: the evaluation of the electron charge distribution rests fully on the low threshold data; the higher threshold data are only good at fixing the muon charge distribution. The similarity of the dependence on threshold of the λ parameters and of the φ parameters (Figure 6.6, reproduced in the left panel of Figure 6.15) is remarkable.

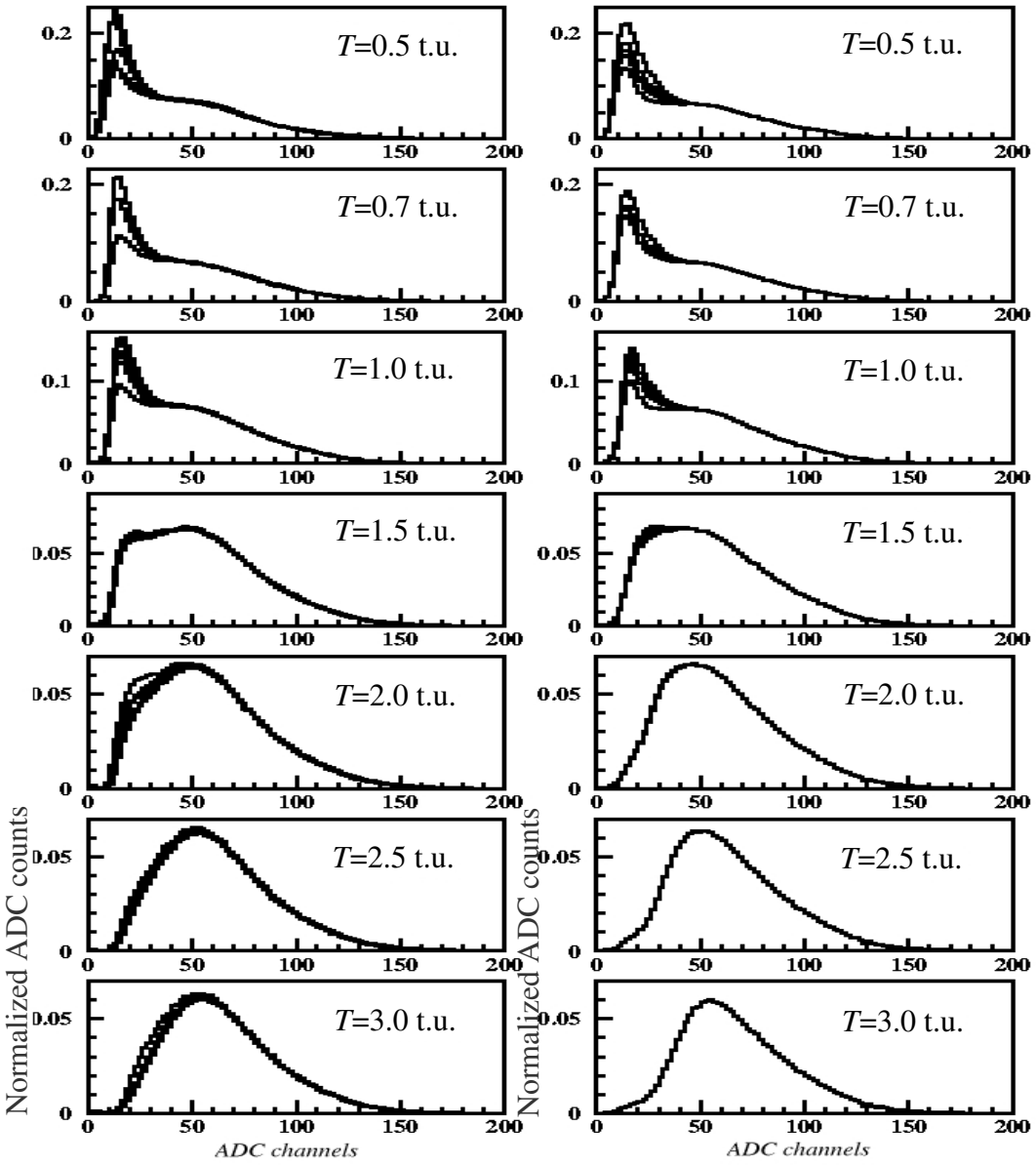

Figure 6.14 Measured charge distributions (left panels) and best fit results (right panels) displayed for each threshold value independently.

The result of the best fit of the form (6.1) to the measured spectra is displayed in Figure 6.14 (right). The quality of the fits implies typical relative uncertainties of 1% to 5% on the measured distributions. Figure 6.16 displays the muon distribution F^{μ} and compares it with the data after subtraction of the electron contribution. It agrees qualitatively with the inclusive distribution measured in PAO Cherenkov detectors [12, 15]. The electron distribution is fit to a form $x^2(3-2x)$, known to describe the energy distribution of electrons produced by a muon decaying at rest. Here, x is the ratio between the electron energy and half the muon rest mass, 53 MeV/c^2. Its value in VEM, corresponding to the upper end point of the energy distribution, is adjusted by the fit, after allowing for a smearing of the measured charges by a Gaussian having a σ equal to σ_{el}. The best fit value of σ_{el} is 34±6% and of the end point 0.42 VEM, while subtracting the muon contribution from the data gives instead an end point value of 0.50 VEM. This disagreement may be due to the inadequacy of the form 6.1 and/or to the insufficient quality of the data. Adjusting the two distributions to the average of the two values, 0.46, produces the result displayed in the left panel of Figure 6.17.

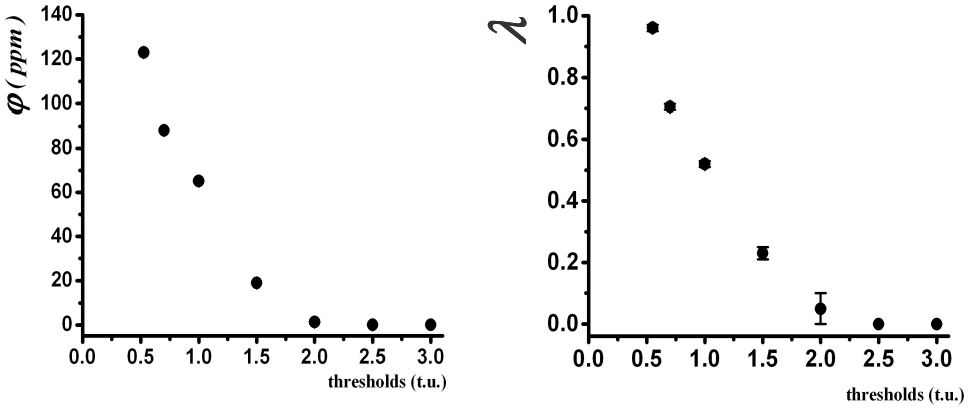

Figure 6.15 Dependence on threshold of the φ (left panel) and λ (right panel) parameters.

Another approach is to remark that the larger contributions to χ^2 are from regions where the spectrum varies rapidly with charge. Adding to the experimental uncertainty a term proportional to the derivative of the spectrum with respect to charge takes care of this anomaly and results in an end point of 0.44 VEM, this time in good agreement with the value found in the muon

subtracted data. The result is displayed in the right panel of Figure 6.17. We also tried to improve the form 6.1 by writing in the expression of the cut-off function $x_{ci}=a_c(th_i-th_0)$, $\Delta_{ci}=b_c(th_i-th_0)$, th_0 being an adjustable parameter. The best fit gives th_0=0.05, a_c=0.17 instead of 0.18 and b_c=0.038 instead of 0.042 while the end point is now 0.39 VEM.

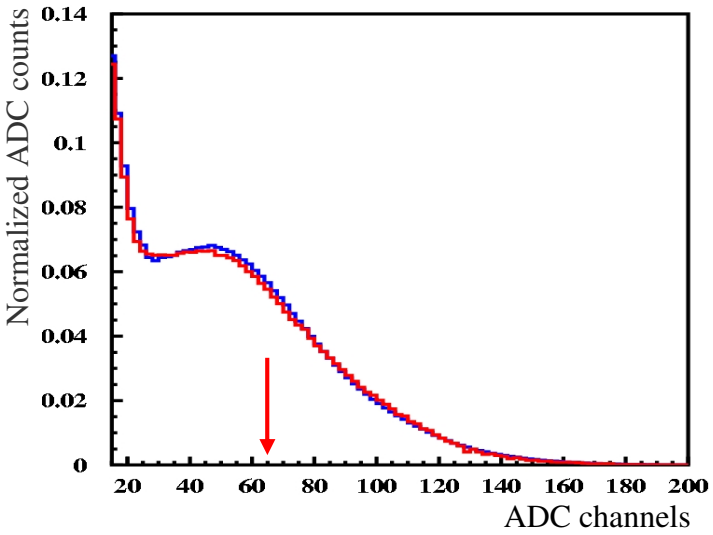

Figure 6.16 Muon charge distribution: the best fit F^{μ} is shown in red and the data, after subtraction of the electron contribution, in blue. The arrow indicates the VEM value.

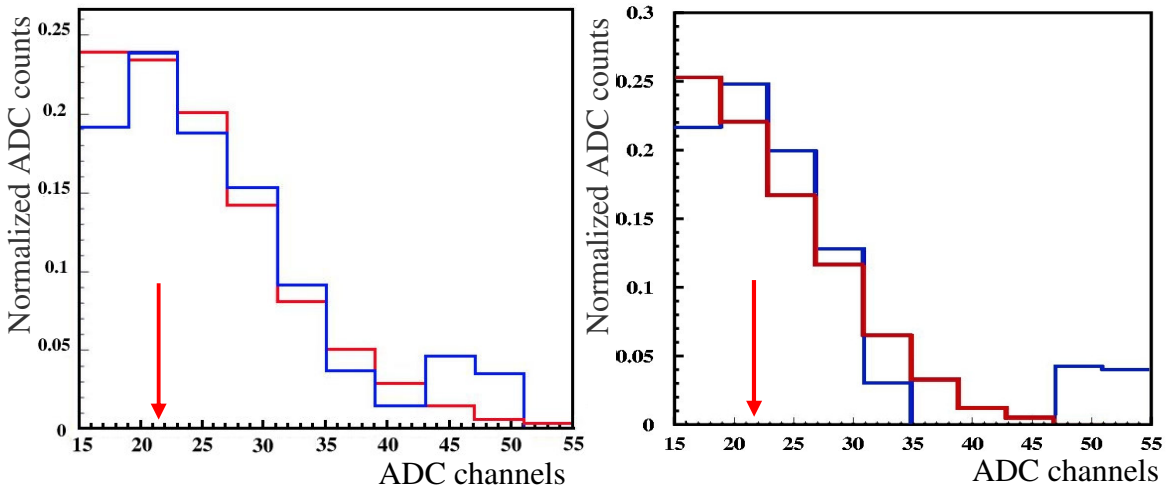

Figure 6.17 Electron charge distribution: the best fit F^{el} is shown in red and the data, after subtraction of the muon contribution, in blue. The arrow indicates a charge of ⅓VEM. Left panel: the charge scales of both distributions have been previously adjusted by ~8% as described in the text. Right panel: experimental uncertainties have been increased to account for rapid variations as a function of charge and the cut-off function has been refined as described in the text. No rescaling needs to be done in that case. The arrow indicates the ⅓VEM value.

Many other attempts at improving the fit have been made but did not produce spectacular improvements. They always gave parameters that did not much differ from those summarized above but provided a reliable estimate of the robustness of our result. Taking these in due account, we retain as final value of the end point 0.40±0.05 VEM.

The higher part normalization of the measured spectra mentioned above consists in summing these from channel 550 to 800, giving a sum Σ_0. To the extent that electrons do not contribute to the higher part of the spectrum, we expect Σ_0 to be simply related to the running time RT: the values of the ratio Σ_0/RT are listed in Table 6.2. Also listed in the table, for each threshold separately, are the mean and rms values of Σ_0/RT.

Figure 6.18 displays the dependence of $<\Sigma_0/RT>$ on threshold and on D_1 after averaging over D_1 or threshold respectively. The independence on D_1 gives evidence, as expected, for the high charge region of the spectrum to be independent from the electron fraction. As expected, values averaged over threshold are delay independent while values averaged over delay decrease with threshold. Conversely, the rms values are small for a given threshold but large for a given delay. The dependence on threshold reflects the fact that the coincidence rate is proportional to the single muon rate: it measures the integral of the muon spectrum at low charges.

We repeated the above analysis by requiring that the first signal of the pair of Cherenkov coincidences producing the trigger be associated with a signal in the upper hodoscope. As can be seen from Figure 5.13, a coincidence between such a signal and each of the scintillators of the upper hodoscope is tagged in a pattern unit (PU3). The charge distributions satisfying this condition are only a fraction f of those analysed earlier but the result of the final fit is essentially the same. Table 6.3 lists the values of the fraction f as a function of threshold and delay. On average, f is independent from delay but decreases with threshold (Figure 6.19)

Table 6.2 Main features of the Cherenkov charge spectra using the Cherenkov trigger.

Runs	*Thr*	D_1	λ	Σ_0/RT	$<\Sigma_0/RT>$	$Rms(\Sigma_0/RT)$
17	*0.50*	*1.0*	–	*2.68*	–	–
26	*0.55*	*0.5*	*0.96(1)*	*1.57*	*1.93*	*0.25*
23		*1.5*		*2.18*		
1		*2.0*		*1.92*		
39		*2.5*		*1.78*		
6		*5.0*		*2.19*		
25	*0.70*	*0.5*	*0.705(10)*	*1.65*	*1.59*	*0.05*
24		*1.5*		*1.59*		
40		*2.5*		*1.54*		
18	*1.00*	*0.5*	*0.52(1)*	*1.48*	*1.32*	*0.22*
16		*1.0*		*1.31*		
20		*1.5*		*1.41*		
22		*2.0*		*0.83*		
7		*5.0*		*1.40*		
27	*1.50*	*0.5*	*0.23(2)*	*0.79*	*1.02*	*0.13*
19		*1.0*		*0.84*		
31		*1.5*		*1.06*		
35		*2.0*		*1.13*		
42		*2.5*		*1.10*		
46		*3.0*		*1.08*		
9		*5.0*		*1.15*		
28	*2.00*	*0.5*	*0.05(5)*	*0.86*	*0.90*	*0.07*
15		*1.0*		*0.97*		
32		*1.5*		*0.87*		
36		*2.0*		*0.98*		
43		*2.5*		*0.78*		
47		*3.0*		*0.90*		
8		*5.0*		*0.97*		
29	*2.50*	*0.5*	*0*	*0.79*	*0.74*	*0.10*
30		*1.0*		*0.59*		
33		*1.5*		*0.75*		
37		*2.0*		*0.86*		
44		*2.5*		*0.83*		
48		*3.0*		*0.77*		
10		*5.0*		*0.61*		
14	*3.00*	*0.5*	*0*	*0.68*	*0.63*	*0.14*
13		*1.0*		*0.31*		
34		*1.5*		*0.61*		
38		*2.0*		*0.71*		
45		*2.5*		*0.64*		
12		*3.0*		*0.68*		
11		*5.0*		*0.80*		

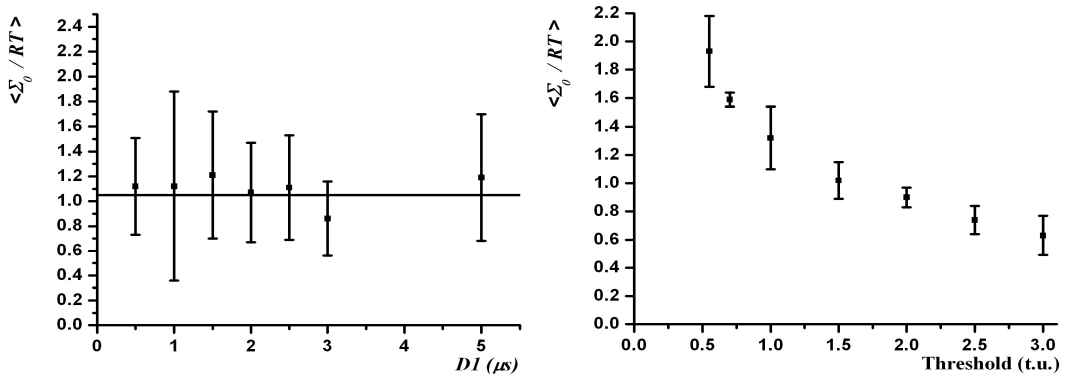

Figure 6.18 Left panel: dependence on D_1 of $<\Sigma_0/RT>$ averaged over threshold. Right panel: dependence on threshold of $<\Sigma_0/RT>$ averaged over D_1. The error bars shown are not uncertainties but rms values.

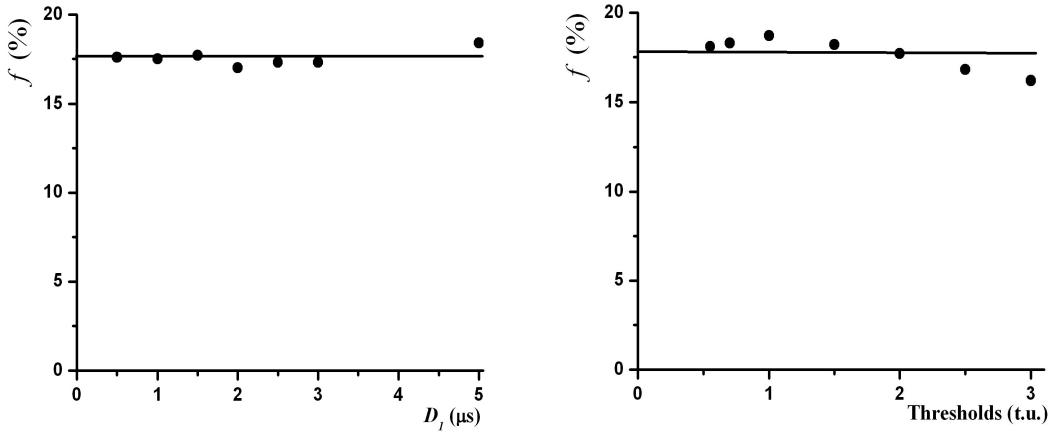

Figure 6.19 Left panel: dependence on delay of *f*, averaged over threshold; Right panel: dependence on threshold of *f*, averaged over delay. Statistical error bars are smaller than the dots.

Table 6.3 Fraction f (%) of data having the upper hodoscope on

Threshold (t.u.)	*Delay (μs)*						
	0.5	***1.0***	***1.5***	***2.0***	***2.5***	***3.0***	***5.0***
0.55	*17.7*	-	*18.3*	*17.3*	*18.5*	-	*18.5*
0.70	*17.8*	-	*18.5*	-	*18.5*	-	-
1.0	*18.5*	*18.6*	*18.6*	*18.5*	-	-	*19.2*
1.5	-	-	*18.6*	*17.2*	*18.0*	*18.1*	*19.1*
2.0	*18.1*	*18.1*	*17.7*	*16.8*	*17.2*	*17.6*	*18.7*
2.5	*16.9*	*17.0*	*16.7*	*16.0*	*16.4*	*16.9*	*17.8*
3.0	*16.5*	*16.4*	*15.5*	*16.2*	*15.4*	*16.6*	*16.8*

6.2.3 Scintillator detectors

A total of eight runs have been recorded in the double plate geometry and five in the single plate geometry.

We perform on these data an analysis similar to that performed on the Cherenkov data. However, as the number of recorded runs is now much smaller, we must limit our ambition to a less detailed study. As in the Cherenkov case, we use the form of relation 6.1 to model the data: $S_{ijk}=N_{ij}\,C_i\,\{\,F_k^{\mu}+\lambda_i\,exp(-D_j/\tau)\,F_k^{el}\,\}$. We recall that i labels the threshold, j the delay and k the charge bin. N_{ij} is a normalisation constant, one for each spectrum; λ_i accounts for the fact that the threshold acts differently on the detection efficiency of muons and on that of electrons; the exponential term accounts for the exponential decrease of the electron contribution as a function of delay (D_1, here written D_j to account for its different values and τ is taken equal to 2.2 μs as capture can be neglected); C_i describes the cut-off at low charges due to the discriminator threshold.

As in the Cherenkov case, rather than fitting the normalisation constants for each independent charge distribution, we set it to unity and normalise the measured distributions in the high charge region where electrons do not contribute.

The cut-off function C_i is taken of the same form $(1+exp[-(x-x_{ci})/\Delta_{ci}])^{-1}$ where x_{ci} and Δ_{ci} are nearly proportional to threshold: $x_{ci}=a_c(th_i-0.05)$, $\Delta_{ci}=b_c(th_i-0.05)$, th_i being the nominal threshold value. It switches from 0 to 1 around $x=x_{ci}$ over a width measured by Δ_{ci}. We use the same values of x_{ci}, Δ_{ci} as found in the Cherenkov case, 11.1 and 2.47 ADC channels respectively, but allow for an overall scale factor resulting from minor changes in the electronics, which the best fit finds equal to 0.41 (double plate geometry) and 0.38 (single plate geometry).

As the ratio between the electron and muon detection efficiencies do not depend much on threshold, at strong variance with the Cherenkov case, we approximate it by a linear form, $\lambda_i=a_\lambda th_i+b_\lambda$ with a_λ and b_λ determined by the best fit; $a_\lambda=-0.58\pm0.17$ and $b_\lambda=12.6\pm0.6$ (double plate geometry) and $a_\lambda=0.71\pm0.16$ and $b_\lambda=6.7\pm0.4$ (single plate geometry).

The resulting muon and electron distributions are displayed in Figure 6.20.

It is remarkable that reasonable fits are obtained while ignoring the short lifetime component: it shows up in a spectacular way in the time distributions but is diluted in the charge distributions and its contribution can be neglected.

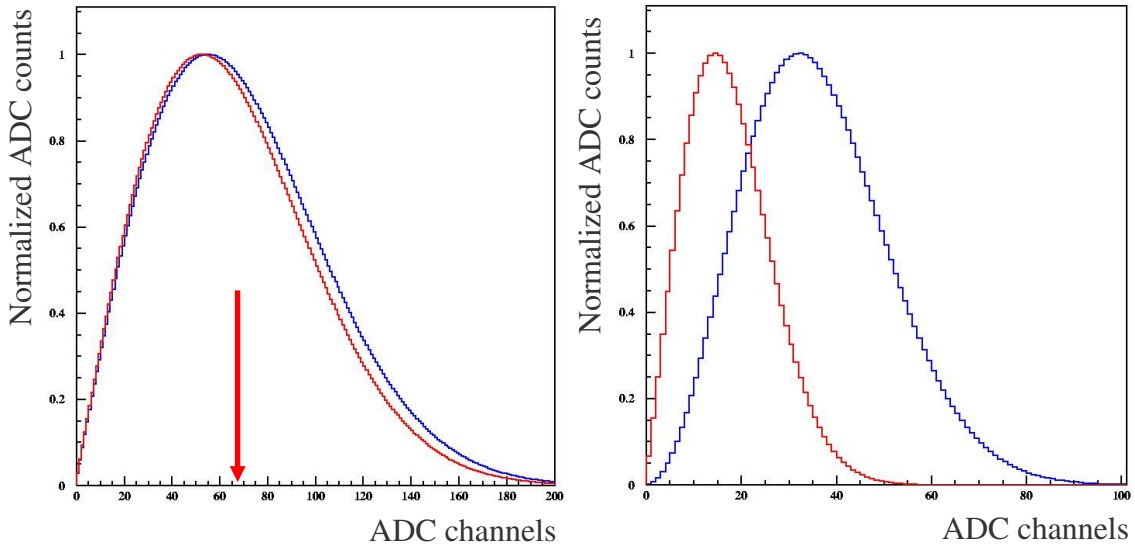

Figure 6.20 Left panel: muon charge distribution (the red arrow shows the peak position for vertical feed-through muons); Right panel: electron charge distribution. Note the different scales (given in ADC channels). The single plate results are shown in blue and the double plate results in red.

On average, with respect to muons, electrons deposit more energy in the single plate configuration than in the double plate. Indeed, the PMT high voltages were increased by ~150 V when switching from the double plate to the single plate geometry in order to keep the straight through muon mean charge (hodoscope trigger) at the same number of ADC channels. This reflects on the left panel of Figure 6.20 where the two inclusive muon distributions have the same mean in spite of being associated with different track lengths (that of the double plate geometry is twice that of the single plate geometry). As the left panel of Figure 6.20 shows, the electron mean charge increases by about a factor 2 when moving from the double plate to the single plate geometry. This means therefore that the electron signals, when referred to a same calibration, are about

the same in the double plate and single plate geometries while the muon signals are roughly in a ratio of 2.

The functions F_k^{el} and F_k^{μ} are defined in such a way that their maximum value is one; they are of the form $ck^a e^{-(k/b)^2}$ where the normalisation factor c is taken equal to 0.066 and 0.031. The integral of F_k^{el} in the single plate geometry is therefore twice what it is in the double plate geometry. The probability of having an electron as second signal compared to that of having a muon is given by the product of this integral by λ_i. As λ_i is about half for the single plate geometry than for the double plate geometry (6.7 instead of 12.6), the probability of having an electron as second particle, relative to the probability of having a muon, does not depend strongly on the geometry.

7. Results and interpretation

7.1 A simple model

In the present section, we compare the Cherenkov results obtained in the preceding sections with the predictions of simulations. As was made clear from the analyses presented in the preceding sections, the contribution of muon pairs from a same shower can be neglected. We therefore use a simple model that considers only two kinds of events: either a pair of uncorrelated muons (from two independent showers) or a stopping muon decaying in the water volume.

In both cases, muons are given a kinetic energy E having a distribution of the form $dN/dE=N_0\,exp(-E/E_{mean})$ where E_{mean} is an adjustable parameter, and a zenith angle θ having a distribution [8] $dN/d\theta=N_0\,cos^2\theta(1-0.108\,sin^2\theta)$ between 0^o and 90^o. Here, N is the muon flux per unit of solid angle, of area (normal to the trajectory) and of time. The charge is calculated in VEM using a Poisson distribution of photoelectrons, the mean number of photoelectrons per VEM being an adjustable parameter, υ. The effect of the threshold k_{thr} (measured in threshold units) on a charge q is simulated by a cut of the form $(1+exp((q-q_{thr})/\Delta q_{thr}))^{-1}$ where q_{thr} and Δq_{thr} depend linearly on k_{thr}. Muons in muon pair events are separated by a time t uniformly distributed between 0 and the width of the time window, 10 μs.

Muon decays (Figure 7.1) are simulated as described in Section 3.2. The parent muon is generated as in the case of muon pairs and its track length l is required to exceed 11 cm, below which a stopping muon does not emit any Cherenkov light. The position x_{stop} of the stop on the track is taken with a uniform distribution between the track exit and a point shifted by 11 cm from the entrance end inside the water volume, each value of x_{stop} being given a weight accounting for its likelihood, namely $dN/dx_{stop}=(dN/dE)/(dx_{stop}/dE)$ where dN/dE has the exponential form given above and dx_{stop}/dE has the form given in Section 3.2.

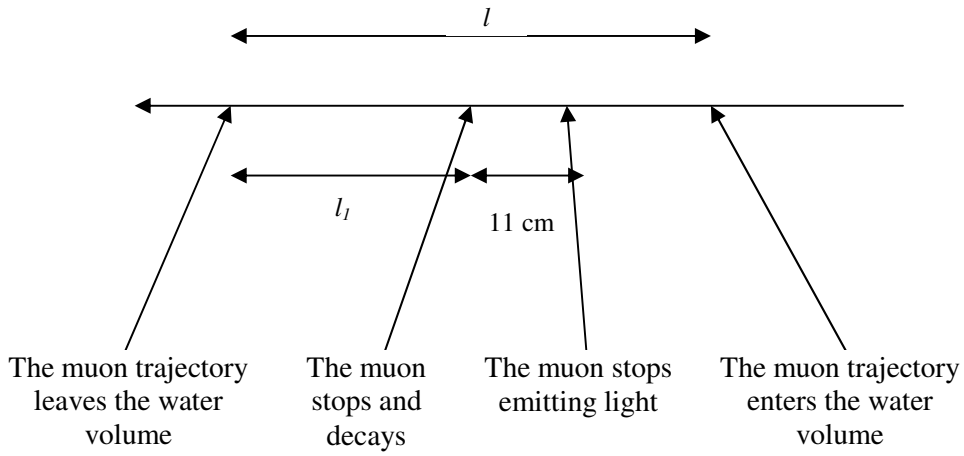

Figure 7.1 Simulation of muon decays: geometry.

The charge of the PMT signals associated with the Cherenkov light emitted by an electron shower of energy E_{decay} is averaged over the electron energy and direction and measured by an adjustable fiducial volume parameter Λ, such that it corresponds to an effective energy $E_{decay}(1-0.5l_1/\Lambda)(1-0.5(l-l_1)/\Lambda)$. Here, l_1 measures the distance between the stop position and the exit point of the muon trajectory. Similarly, $l-l_1$ measures the distance between the stop position and the entrance point of the muon trajectory. The parameter Λ is therefore a measure of the shower size and its scale is the radiation length (36 cm in water). The adjustable parameter $E_{decay}=xE_{end}$ is taken with a standard muon decay distribution ($dN/dx=6x^2-4x^3$, see Section 3.2) having its end point ($x=1$) at E_{end} and smeared by a Gaussian having a $\sigma=\sigma_{el}$, where both E_{end} and σ_{el} are adjustable parameters measured in VEM.

The muon decay time distribution is taken exponential with an effective decay time of 2 μs accounting for muon capture in water and the decay electron is required to be emitted within the accepted window (width W_1 and delay D_1).

7.2 Comparison with the data

The charge and time distributions measured using the Cherenkov detector have been fitted simultaneously to the above model. Acceptable fits could only be obtained at the price of a number of modifications:

1) It was necessary to modify the model in order to reproduce the muon distribution. Our choice has been to allow for a dependence on zenith angle θ of

the detection efficiency of Cherenkov light: the charge associated with the Cherenkov emission of the muon is measured by the track length l in water multiplied by a factor $exp(-\sigma(1-cos\theta)/cos\theta)$ where σ is an adjustable parameter.

2) It was necessary to use a cut-off function having a relatively sharp start and a much slower tail. This was achieved by dividing Δq_{thr} by 5 when q is smaller than q_{thr}. Figure 7.2 displays the modified charge dependence of the cut-off function for different values of k_{thr}.

3) The uncertainties in each bin were taken as the quadratic sum of the statistical uncertainty and a systematic uncertainty taken to be 0.7 permil (respectively 0.9 permil) of the integrated time (respectively charge) distributions in order to obtain a value of χ^2 similar to the number of degrees of freedom and to give equal weights to the time and charge data.

The results are listed in Table 7.1 and are briefly commented below.

Table 7.1 Best fit results to time and charge data using the simple model.

Parameter	E_{mean} *(GeV)*	σ	υ *(p.e./VEM)*	Λ *(cm)*	E_{end} *(VEM)*	σ_{el}
Best fit result	4.2	0.63	4.7	24	0.08	0.03

The mean value of the muon kinetic energy, E_{mean}=4.2 GeV, is in good agreement with expectation [10]. It is weakly correlated with the value of σ=0.63 that implies that at 45^o zenith angle the detection efficiency of Cherenkov photons is a factor 0.77 times that for a vertical incidence muon.

While the value of Λ, 24 cm is at the scale of the radiation length in water (36 cm) as expected, the value of υ, 4.7 photoelectrons per VEM, is unexpectedly low. It is obtained here for two photomultiplier tubes, meaning ~7 for three as in the PAO configuration or in Figure 2.19. It is a factor ~3 smaller than obtained from vertical feed-through muons (see Section 2.4.3) and would require an important deterioration of the resolution in the low charge regime, which would have probably to be blamed on electronics noise and high frequency pick up on the PMT bases and signal cables. The values of E_{end} and σ_{el} are strongly correlated, with $E_{end}+\sigma_{el}$~0.11 VEM, a result of the fact that the fit is only

sensitive to the tail of the charge distribution, as was already commented in Section 6.2.

In spite of the above modifications that were found necessary, the quality of the fit was not good, in particular at low charges. However, the comparison of the data with such a simple model has been useful at revealing its weaknesses and at suggesting improvements that are reported below.

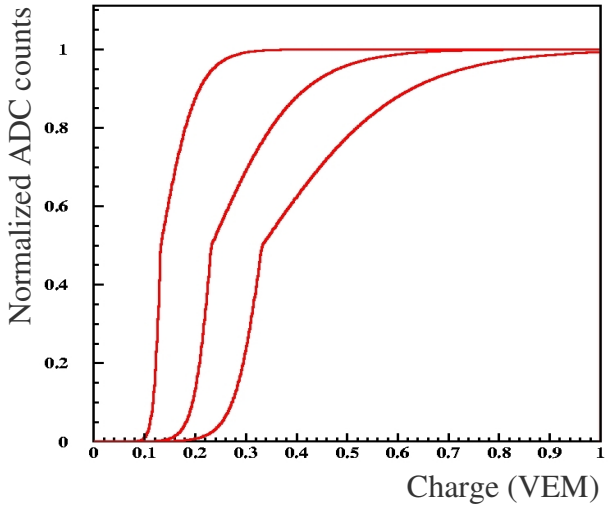

Figure 7.2 Charge dependence (VEM) of the threshold cut-off functions for threshold units of respectively 0.5, 1.5 and 2.5.

7.3 Including a soft component

A major problem of the simple model used in the previous paragraph is its inability to reproduce what was meant to be the muon contribution. We know from Figure 3.6 that the charge distribution expected for muons, including or not stopping muons, is not expected to peak at low charges while the data require a so-called muon contribution that does, as was made clear in Figure 6.16. Figure 7.3 below illustrates this discrepancy. The simulated charge distribution, even after having been smeared to account for photoelectron statistics (here using 14 photoelectrons per VEM), does not display any peaking at low charges at variance with the measured distribution.

Indeed, a low charge component, the so-called soft component, which is not taken into account in the simple model, has been known to exist for many years [21] and is essentially composed of soft electrons, positrons and photons (it is therefore an abuse of language to include it in the “muon” contribution, one

should strictly speak of a "non-decay-electron" contribution). As it is not penetrating, it does not show up whenever a coincidence between two different detectors is required; however, in the present case where the coincidence is between two PMTs looking at the same water volume, there is no such suppression. As shown in Figure 7.4, it is also present in the PAO data [15], however at a different rate because of the different altitude (1400 m rather than sea level).

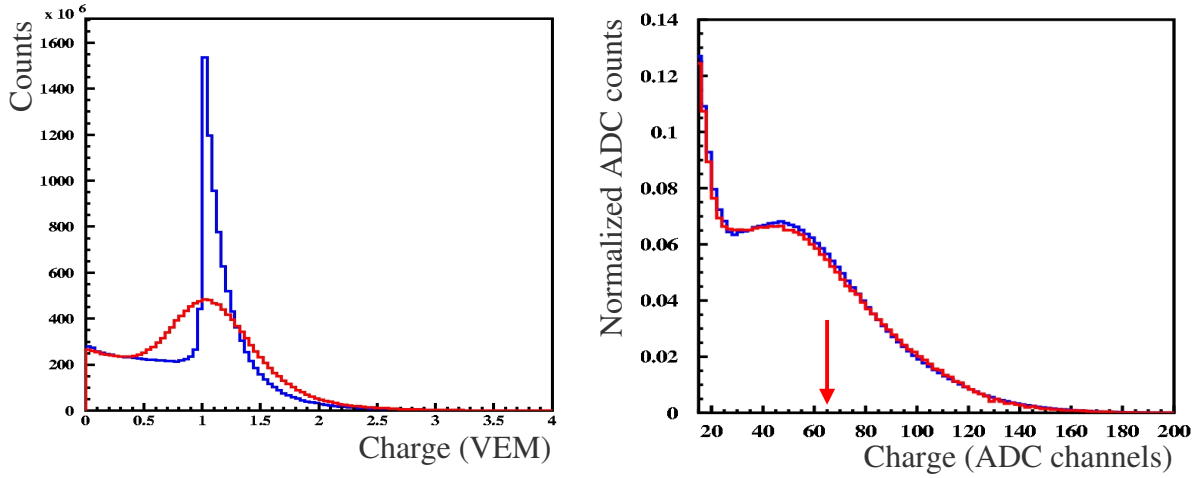

Figure 7.3 Muon charge distributions as obtained from a simple simulation (left, VEM units) and as measured (right, 1 VEM=65ADC units, see Figure 6.16). Left: blue is before Poisson smearing and red after using a value of 14 photoelectrons per VEM.

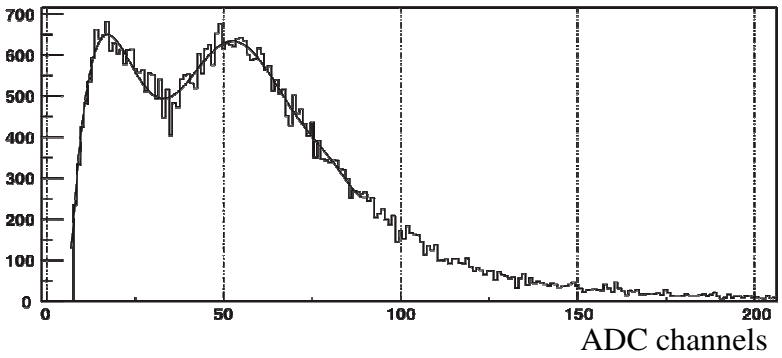

Figure 7.4 Histogram of signals from one PMT in a PAO Cherenkov detector. A threshold of 10 to 20 channels cuts off the data at low charges.

We have modified the simple model used in the preceding paragraph to include such a soft component. We use an exponential dependence on charge q of the form $dN/dq=q_{soft}^{-1}exp(-q/q_{soft})$ where q_{soft} is an adjustable parameter. We

use as a second adjustable parameter the fraction f_{soft} of the inclusive rate taken by the soft component.

7.4 Threshold cut-off functions

The simple model has revealed the inadequacy of applying a narrow threshold cut-off function to the analysed signal. The reason is obvious: the threshold does not apply to the analysed signal, which is the sum of two PMT signals, but to each of these individually. To understand the effect, one may illustrate it with a simple example as is done in Figure 7.5. Assume that each phototube looks at a same q signal, each with the same Poisson statistics in terms of photoelectrons per VEM and independently subject to a sharp cut at q_0. The resulting summed signal is affected by the threshold cuts in a way that is illustrated in Figure 7.5 by displaying cut-off functions defined as the ratios between the observed sum signal and what it would be in the absence of cut. While there is no signal surviving the cut below $2q_0$, as expected, the sum signal rises smoothly and reaches its maximum only when the threshold is low enough not to affect any of the two individual PMT signals. In general, the cut-off functions depend therefore on the shape of the signal.

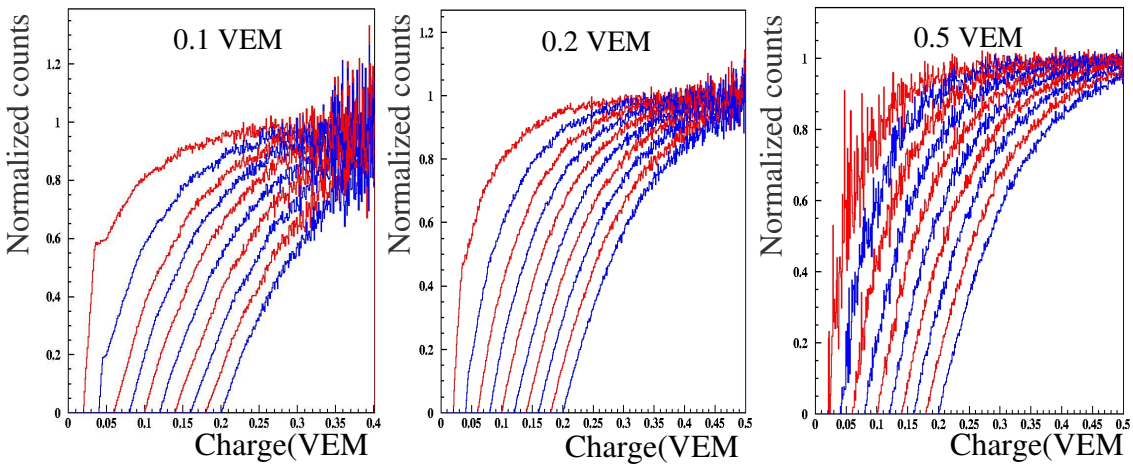

Figure 7.5 Cut-off functions for signals of respectively 0.1 (left), 0.2 (middle) and 0.5 (right) VEM detected with a photoelectron statistics of 20 photoelectrons per VEM. In each case curves have been drawn for ten sharp threshold values, from 0.01 to 0.10 VEM. Large fluctuations resulting from the finite Monte Carlo statistics are seen in regions that are not much populated by the signal, but they are irrelevant to the point being made here.

Of course, if the two signals were strictly identical, a sharp cut-off on each of them would produce a sharp cut-off on their sum. But when, as is the case here, the two signals are not strongly correlated, a slow cut-off function results on the sum. This effect, which indeed resembles that revealed by the simple model (Figure 7.2) has been implemented in the simulation by assuming that the number of Cherenkov photons reaching the PMTs is equally shared between them and applying Poisson statistics and threshold cut-off to each of them separately. The individual threshold cut-off functions have been assumed to rise linearly between $q_{thr}-\Delta q_{thr}$ and $q_{thr}+\Delta q_{thr}$. The slow effective rise of the cut-off functions on the sum signals are now largely reproduced naturally and reasonable values of Δq_{thr} are obtained although a sharp cut-off is excluded. However, the best fit requires a value of q_{thr} that does not quite cancel for zero nominal threshold; hence parameterizations as a function of k_{thr} (in threshold units) of the form $q_{thr}=a_{thr}+b_{thr}k_{thr}$ and $\Delta q_{thr}=c_{thr}k_{thr}$.

7.5 Dependence on zenith angle

Another lesson of the simple model is the need for a dependence on zenith angle of the light collection efficiency. In order to investigate what to expect in this context, we simulate the physics of light collection, which we parameterize by two parameters: a light attenuation length in water, Λ_{att} and a diffusion (or reflection) coefficient η describing the ratio between the diffused (or reflected) and incident light on wall encounters [22]. We use a reasonable guess as default values: Λ_{att}=20 m and η=0.85. We simulate both Lambertian diffusion on the tank walls (as is probably the case for the PAO where the walls are made of Tyvek) and specular reflection (that can probably no longer be neglected in the VATLY case where the walls are coated with aluminized Mylar).

It must be first remarked that in the case of a perfect optical cavity, $\Lambda_{att}=\infty$ and $\eta=1$, any Cherenkov photon emitted along a muon track ultimately escapes into one of the PMTs. If $3N$ photons are emitted and if there are 3 PMTs, each PMT receives therefore N photons. In such a case, the signal in each PMT is strictly proportional to track length and one does not expect any dependence of the light collection efficiency on zenith angle. In practice, however, Λ_{att} takes a

finite value and η is smaller than unity. The detected signal becomes $N^k \exp(-l/\Lambda_{att})$ where k is the number of wall reflections (or diffusions) and l the optical path that precede the escape into the PMT photocathode. Back to the case of a perfect optical cavity, the number of photons detected for $k<k_{max}$ and/or $l<l_{max}$ is now smaller than N and its ratio to track length may very well become zenith angle dependent. Another way to say it is that in the case of a perfect optical cavity, while the time integral of each signal is N, its duration may be time dependent: all photons are indeed ultimately collected but the optical path length and the number of reflections/diffusions per track length that it takes to achieve it may well be zenith angle dependent.

An effect that produces a dependence of the light collection efficiency over zenith angle is the existence of direct light (Figure 7.6). It results from the fact that it becomes possible for Cherenkov light to reach the PMTs without any diffusion or reflection when the zenith angle exceeds 41^o ($\cos\theta$=0.75). Figure 7.7 displays the distribution of the number of diffusions or reflections that occur before reaching the PMTs for different intervals of $\cos\theta$. It shows clearly how for small zenith angles direct light (no preceding diffusion or reflection) is relatively suppressed, while it becomes more and more important when the zenith angle increases.

In general, in the case of a non-perfect optical cavity, one may then expect a zenith angle dependence of the light collection efficiency. However, to the extent that the number of photons effectively collected in the PMTs is much smaller than the total number of Cherenkov photons produced, this dependence cannot be very important. Indeed, in such a case, each Cherenkov photon has a small probability P, in principle dependent on $\cos\theta$, to be detected after a given optical length l_{max} and a given number of reflections/diffusions k_{max}. But the average values of l and k will be only slightly smaller than $l_{max}/2$ and $k_{max}/2$ respectively to the extent that only few photons have been collected before reaching l_{max} or k_{max}. As the effective values of l_{max} and k_{max} are defined soleley by Λ_{att} and η, they do not depend on $\cos\theta$. Moreover, as the light collection efficiency is completely defined by the average values taken by l and k, it will not depend on $\cos\theta$ either. This is indeed what the simulation predicts: Figure

7.8 displays the dependence on zenith angle of the mean number of photoelectrons per VEM for Λ_{att} =2000 cm and η=0.85. In such a case, the light is attenuated by 1% after ~28 reflections/diffusions or after ~9200 cm optical path. The dependence on $cos\theta$ is indeed quite small, particularly in the case of Lambertian diffusion, the main effect being that of direct light in the case of specular reflection.

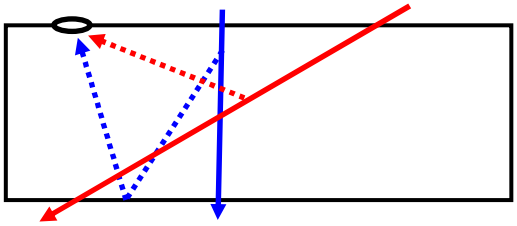

Figure 7.6 Direct light: illustration of the zenith angle dependence of the light collection efficiency. For muons (full lines) having a zenith angle in excess of the Cherenkov angle (41°, red) photons (dotted lines) can reach the PMT directly. Otherwise (blue) a minimum of one reflection or diffusion is required.

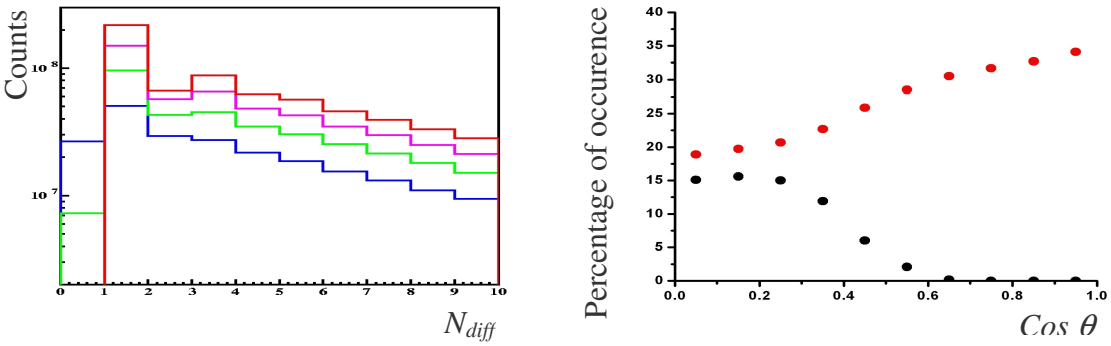

Figure 7.7 Left: distribution of the number of diffusions preceding detection by the PMTs for $cos\theta$= 0.3 to 0.4 (blue), 0.5 to 0.6 (green), 0.7 to 0.8 (magenta) and 0.9 to 1 (red). Right: Relative occurrence (%) of respectively zero (black) and one (red) diffusions preceding detection by the PMTs as a function of $cos\theta$.

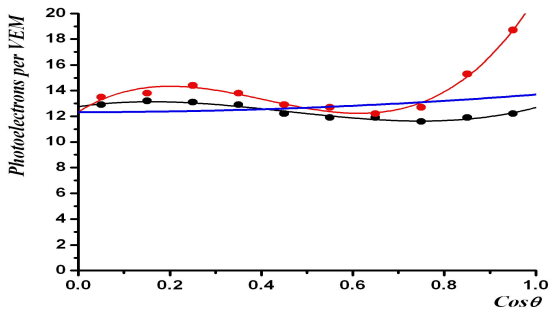

Figure 7.8 Dependence on $cos\theta$ of the mean number of photoelectrons per VEM for Λ_{att} =2000 cm and η=0.85. The black curve is for Lambertian diffusion and the red curve for specular reflection. A zenith angle dependence of the form 1–0.10$sin^2\theta$, as required by the best fit, is shown as a blue curve.

7.6 Comparison between data and simulation

Figures 7.9 and 7.10 compare the data with the best fit result of the simulation. While the fit is globally very good, one notes that some disagreements subsist in a few cases of charge distributions near threshold.

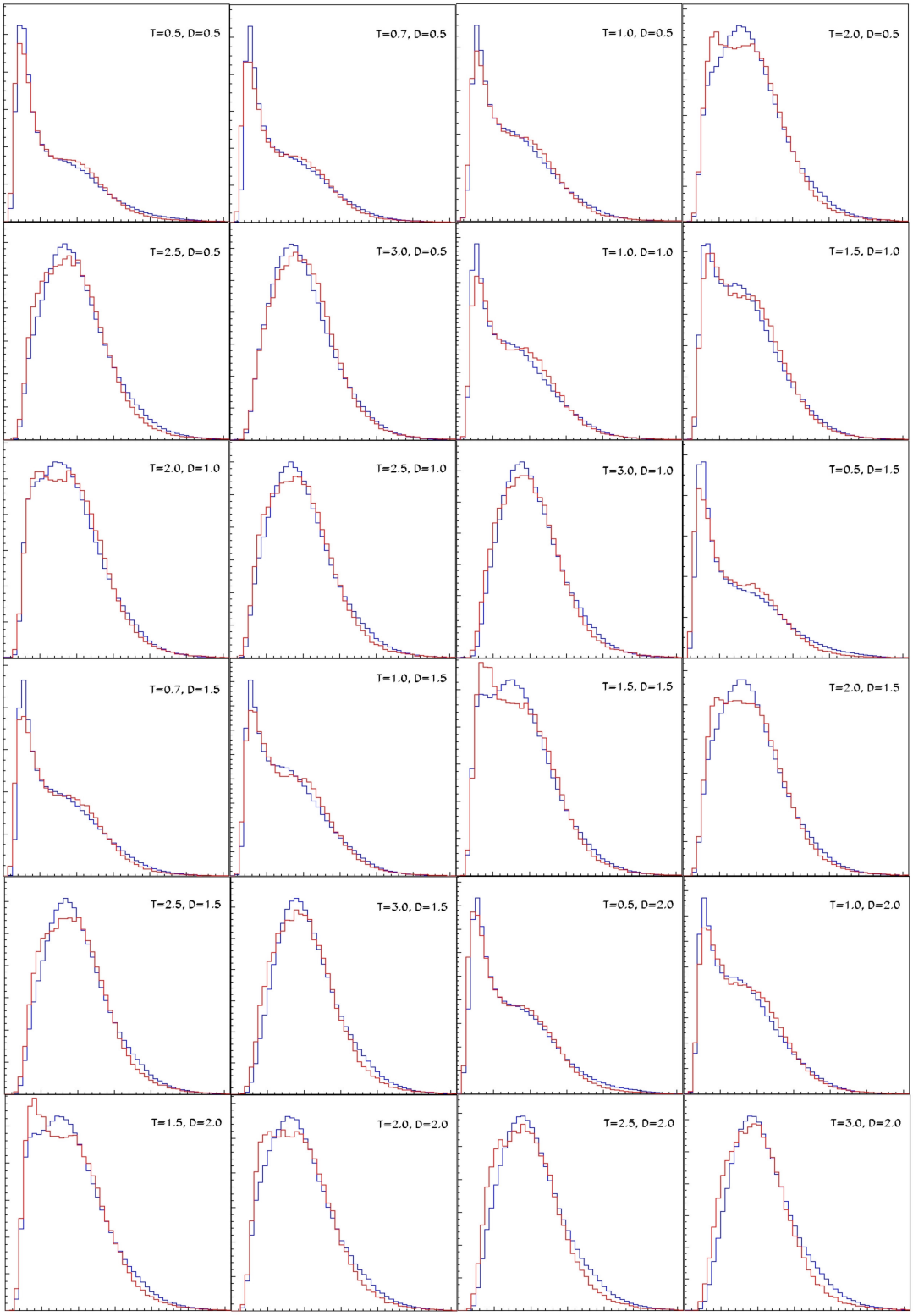

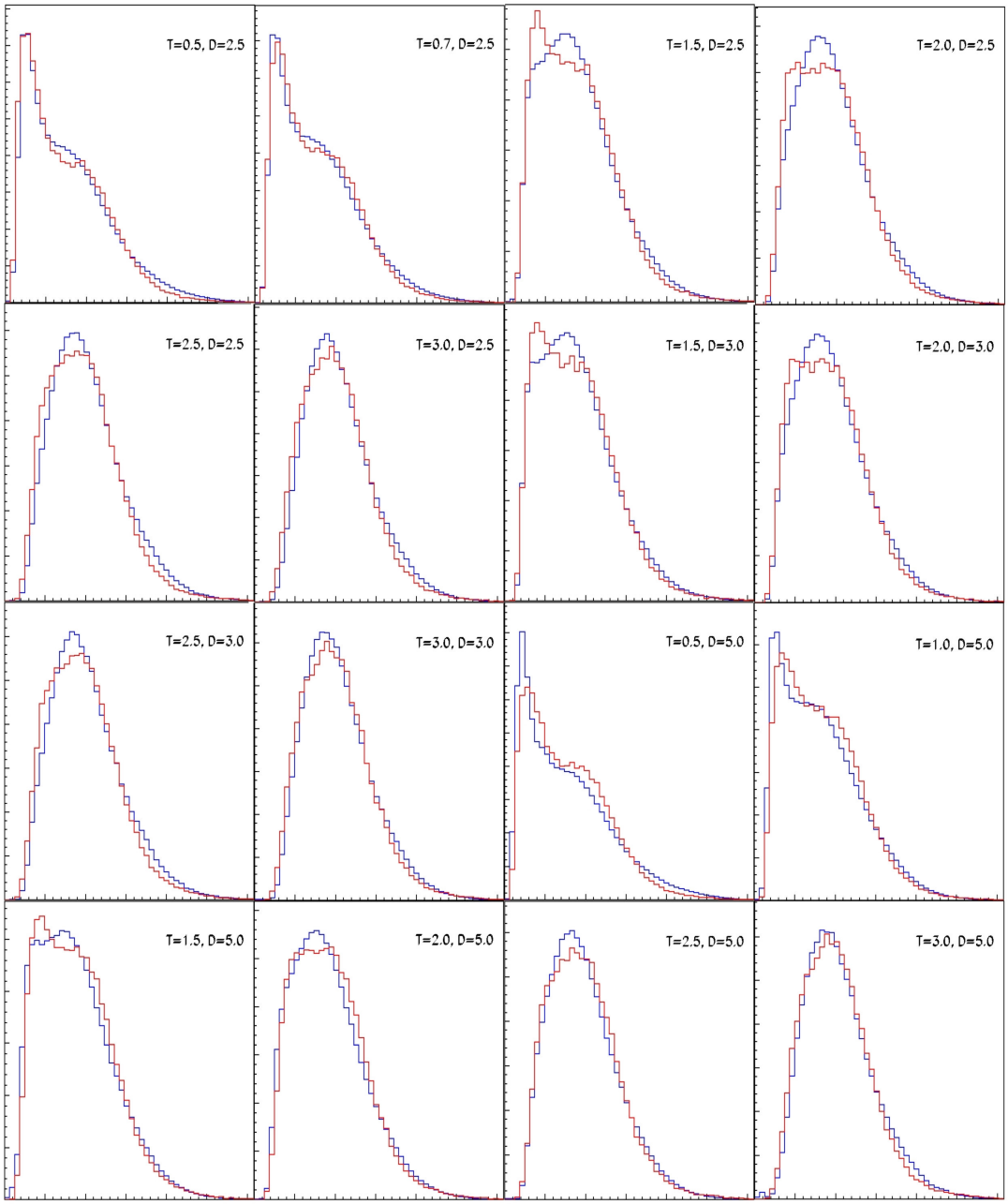

Figure 7.9 Charge distributions measured (blue) and predicted (red) for different delays and thresholds. Each panel is labeled by its threshold T (in threshold units) and its delay D (in microseconds).

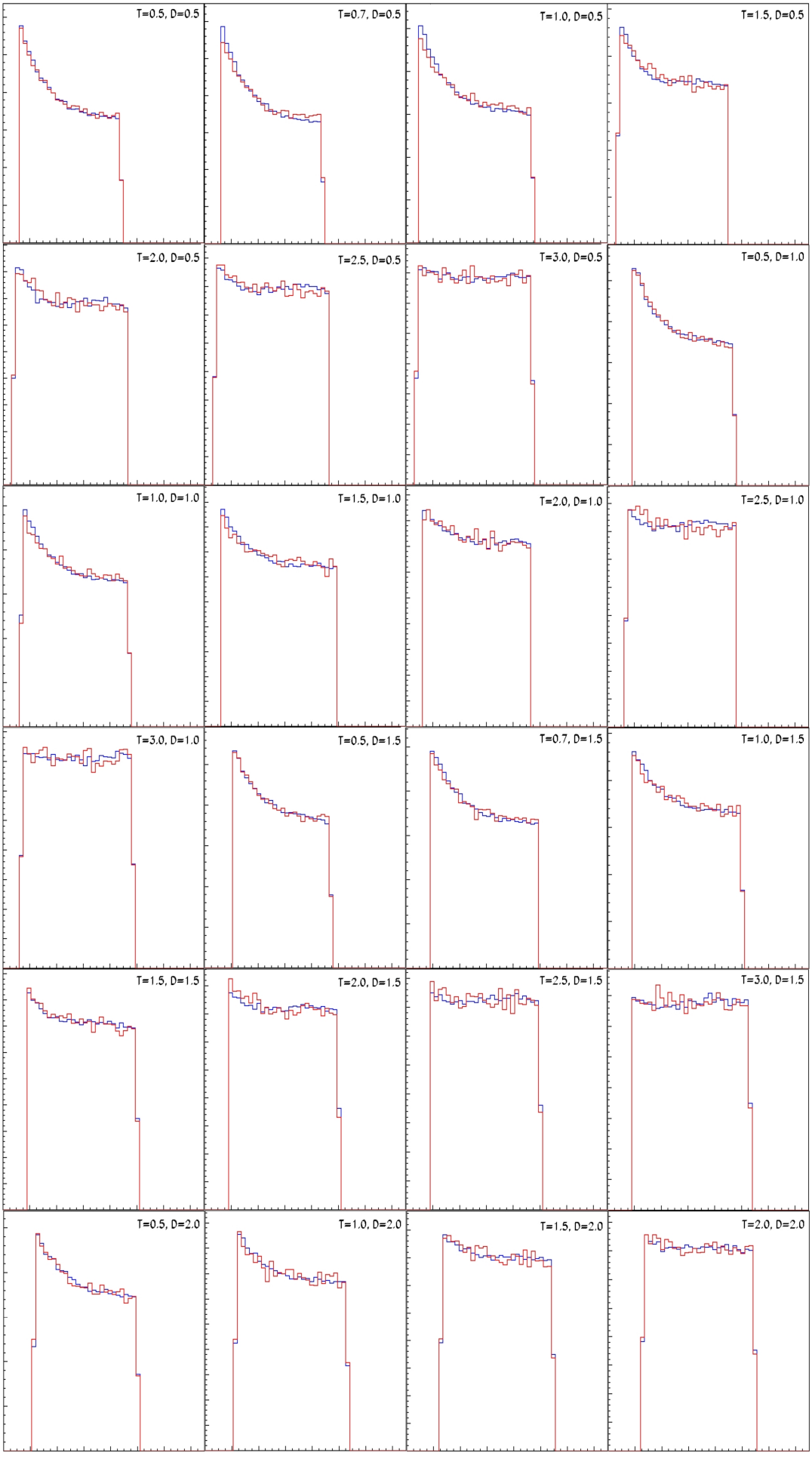
T=0.5, D=0.5
T=0.7, D=0.5
T=1.0, D=0.5
T=1.5, D=0.5
T=2.0, D=0.5
T=2.5, D=0.5
T=3.0, D=0.5
T=0.5, D=1.0
T=1.0, D=1.0
T=1.5, D=1.0
T=2.0, D=1.0
T=2.5, D=1.0
T=3.0, D=1.0
T=0.5, D=1.5
T=0.7, D=1.5
T=1.0, D=1.5
T=1.5, D=1.5
T=2.0, D=1.5
T=2.5, D=1.5
T=3.0, D=1.5
T=0.5, D=2.0
T=1.0, D=2.0
T=1.5, D=2.0
T=2.0, D=2.0

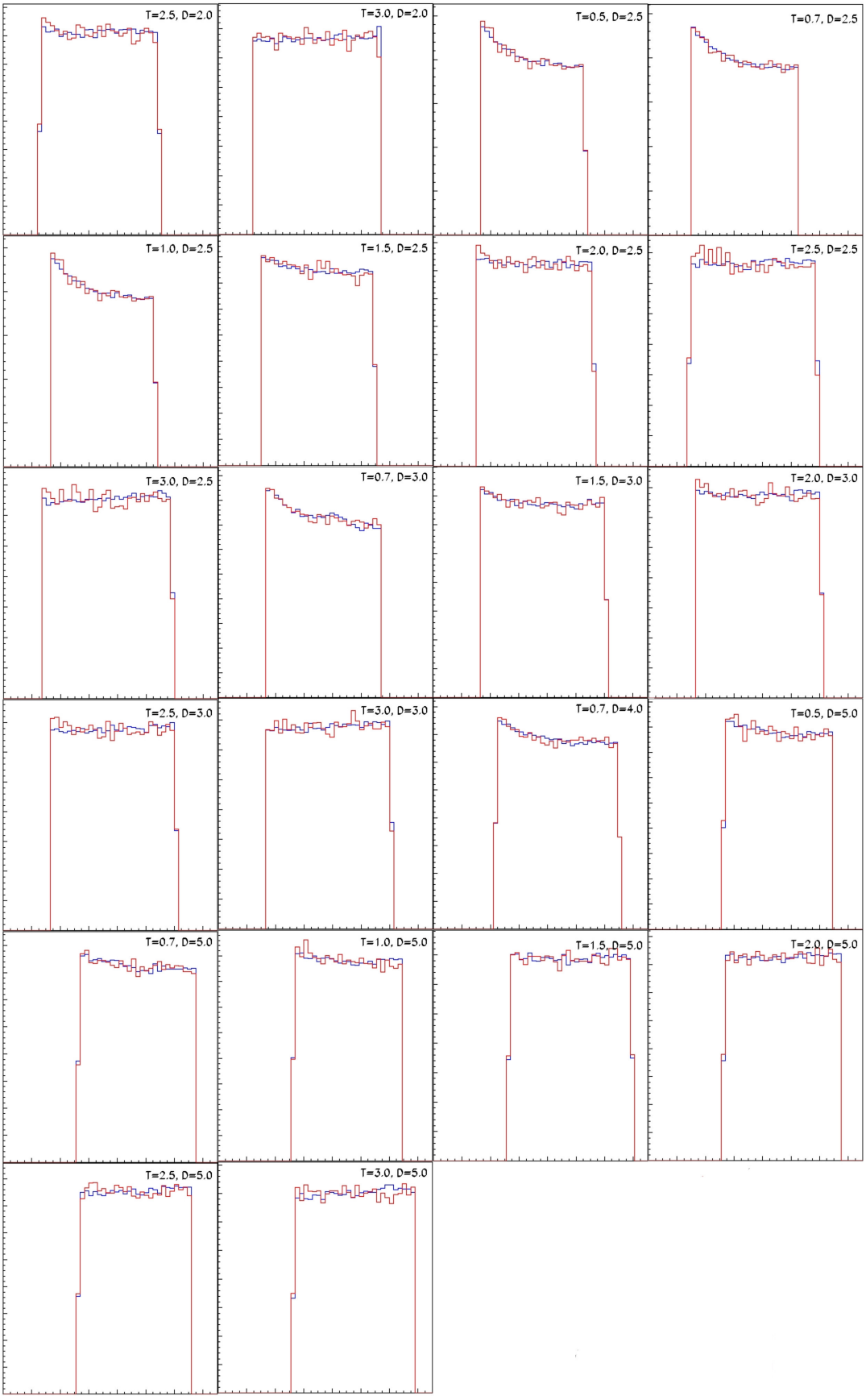

Figure 7.10 Time distributions measured (blue) and predicted (red). Each panel is labeled by its threshold T (in threshold units) and its delay D (in microseconds).

The crudeness of the model used to simulate the effect of threshold, and the sensitivity of the quality of the fit to a precise description of the cut-off functions, are one reason. Another reason is the crudeness of the description of the soft component by a simple exponential. However, rather than restricting the fits to a charge range sufficiently above threshold to guarantee a perfect fit, we prefer to extend the fit to the whole charge range and accept some small disagreements near threshold. The values obtained for the parameters that have been adjusted are listed in Table 7.2. The uncertainties that are quoted neglect correlations between the parameters: they simply correspond to the shift of the parameter with respect to the best fit value such that the χ^2 per degree of freedom (of which there are 10199) increases by 1%. Properly speaking, they are therefore rather indicators of the sensitivity of each particular parameter to the quality of the fit. We now comment each of these in turn:

– The number of photoelectrons per VEM is now υ=13.0±0.9 in very good agreement with our earlier estimate of 14 obtained from the width of the calibration curves. This number is really an effective number of photoelectrons per VEM, including other effects that might cause a smearing of the charge measurement. It is rewarding to find that the effect is consistently described by a single value in both the VEM region and in the low charge regime (stopping muons and decay electrons).

– The value of the end point of the charge distribution of decay electrons is E_{end}=0.275±0.018 VEM. We note that it is no longer necessary to smear this distribution beyond the natural smearing resulting from photoelectron statistics. The resulting smeared distribution is displayed in Figure 7.11. This result is consistent with the value obtained in PAO data, where the mean decay electron charge is 0.12 VEM.

– The soft component is described by f_{soft}=0.795±0.012 and q_{soft}=0.32±0.02 VEM. The high value of f_{soft} is somewhat misleading to the extent that charges smaller than ~0.1 VEM are cut by the threshold. Indeed, Figure 7.11 displays the soft component in the range where it is observed and where it can be compared with the electron and muon contributions. It must be remarked that we have no way to tell the difference between a real and a fake soft

component contribution. The requirement of a coincidence between two photomultiplier tubes is a protection against electronic noise, of which the contribution to the soft component cannot exceed ~10%. However, a small light leak is an ideal candidate to fake such a soft component: the requirement of a coincidence does not protect against it. The argument against a significant light leak contribution is the independence of the trigger rate on ambient light, a large fraction of the data having been collected during the night. But this example illustrates the weakness of the trigger for discriminating against very low signals, the large water volume implying a high detection efficiency. Another point of relevance is the sensitivity to soft electrons: they have significant mean free paths in water and their very low mass allows for Cherenkov radiation emission down to MeV kinetic energies. While both the value of the trigger rate and the comparison with similar data taken with PAO tanks indicate that the soft component detected here is not too heavily contaminated by spurious sources, we must keep these arguments in mind and refrain from quoting a value for the soft component rate. Such a measurement would require a different set-up, better adapted to the task.

– The value taken by Λ, 36±6 cm, is (by chance) precisely equal to the value of the radiation length in water, however with a large error; indeed, this parameter is only an ad hoc way to simulate the fiducial volume effect and there is no reason for it to be precisely equal to the radiation length although it is expected to be of the same order of magnitude.

– The parameters describing the dependence of the cut-off function on k_{thr} are a_{thr}=0.022±0.002 VEM, b_{thr}=0.0495±0.0013 VEM and c_{thr}=0.035±0.006 VEM per threshold unit. The value of c_{thr} deviates significantly from zero, although much of the smearing effect is naturally produced by the mechanism described in sub-section 7.4.

– The fit was performed by neglecting a possible dependence of the light collection efficiency on zenith angle (see subsection 7.5 and Figure 7.8). Assuming that the optical properties of the tank are better described by a Lambertian diffusion than by a specular reflection (although, as already mentioned, we expect an intermediate situation) and including a dependence on

zenith angle of the form $1-\xi \sin^2\theta$ predicts a value ξ=0.10±0.04, in good agreement with the analysis performed earlier and suggesting that Λ_{att}=20 m and η=0.85 are indeed sensible estimates of the optical quality of the tank cavity.

– The mean muon kinetic energy is $E_{mean}= 4.0^{+0.4}_{-0.3}$ GeV, in excellent agreement with the expected value [10]. It is remarkable that the data are able to measure it properly in such an indirect way.

Table 7.2 Best fit values of the model parameters

Parameter	Symbol	Value (error)
Soft component probability	f_{soft}	0.795 (0.012)
Soft component width (VEM)	q_{soft}	0.32 (0.02)
Decay electron end point (VEM)	E_{end}	0.275 (0.018)
Shower size (cm)	Λ	36 (6)
Mean muon kinetic energy (GeV)	E_{mean}	$4.0^{+0.4}_{-0.3}$
Number of photoelectrons per VEM	υ	13.0 (0.9)
Threshold offset (VEM)	a_{thr}	0.022 (0.002)
Cut-off slope (per threshold unit)	b_{thr}	0.0495 (0.0013)
Cut-off width (per threshold unit)	c_{thr}	0.035 (0.006)
Light collection efficiency parameter	ξ	0.10 (0.04)

Figure 7.11 displays the respective contributions of the soft component, muons and decay electrons to the charge distribution at low threshold and for both a small and a large value of the delay. It illustrates the difficulty of the measurement, the decay electron component becoming negligible for charges in excess of ~0.5 VEM, and being largely hidden behind the soft component. Figure 7.12 displays the charge distribution associated with Cherenkov photons emitted by stopping muons that produce detected decay electrons. The figure is drawn for the lowest threshold value and a delay D_1=0.5 μs. Its shape is nearly the same for a delay of 5 μs (but its amplitude is of course much smaller). The mean value of the charge distribution displayed in Figure 7.12 is 0.54 VEM. Such a small value, although larger than that of the electron distribution, adds to the difficulty to detect electrons from muon decays when using a Cherenkov detector.

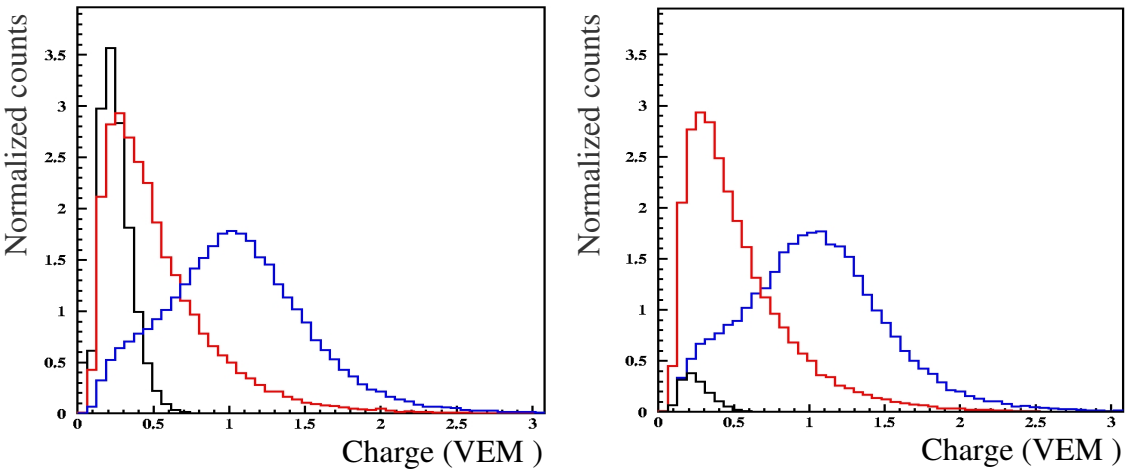

Figure 7.11 Respective contributions of the soft component (red), decay electrons (black) and cosmic muons (blue) for the smallest threshold value (0.5 t.u.) and respective delays of 0.5 μs (left) and 5.0 μs (right).

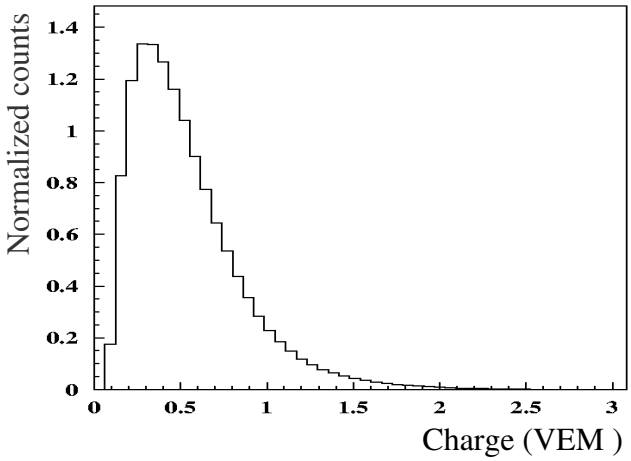

Figure 7.12 Charge distribution (VEM) associated with stopping muons that produce a detected decay electron for a threshold of 0.5 t.u. and a delay D_1 of 0.5 μs.

7.7 Decoherence and shower size

In Section 6.1.2 we established that the best fit to the time distributions measured in the Cherenkov detector to a form

$$R\exp(-R\delta t)+g_0 R_{sh} \exp(-R_{sh}\delta t)+\varphi\rho_+ R_+ \exp(-R_+ \delta t)+\varphi\rho_- R_+ \exp(-R_- \delta t).$$

gives a value of parameter g_0 of $(0.79\pm0.05)\times10^{-5}$ for a decline time of 1.13±0.04 μs, meaning a rate of 7.0±0.5 Hz compared with an inclusive muon rate of ~2kHz. It implies that the probability to have a second muon from the same shower detected in the Cherenkov tank when one has already been detected is 3.5 permil. This can be translated in an estimate of the product of the shower

multiplicity by the shower radial size. The low energy showers that produce the detected muons have kinetic energies larger than the rigidity cut-off (17 GV), say 20 to 50 GeV typically. Their hadron multiplicity is therefore quite low. The use of a lateral distribution function to describe the radial shower size is not appropriate in such a case and one rather uses a decoherence function describing the dependence of the coincidence rate of two small counters on their separation. A crude estimate can be obtained by assuming that the mean shower has m muons uniformly distributed on ground in a circle of radius R_{sh} and that the Cherenkov detector is circular of radius R_0. Then, For $R_{sh}>>R_0$, the probability of detecting a second muon from the same shower is simply $(m-1)(R_0/R_{sh})^2$. For $m=2$, this corresponds to R_0/R_{sh} ~6%, namely a shower radial size of ~30 m.

Figure 7.13 illustrates a slightly better procedure using the distribution of the separation between two points on ground for a shower density depending exponentially on the distance to the shower core; convolving it with the distribution of the separation between two points in the detector gives a very similar dependence to that obtained before. For $m>2$, we obtain larger estimates of R_{sh}, at variance with higher energies [23] where the shower size is governed by the Molière radius, ~80 m at sea level.

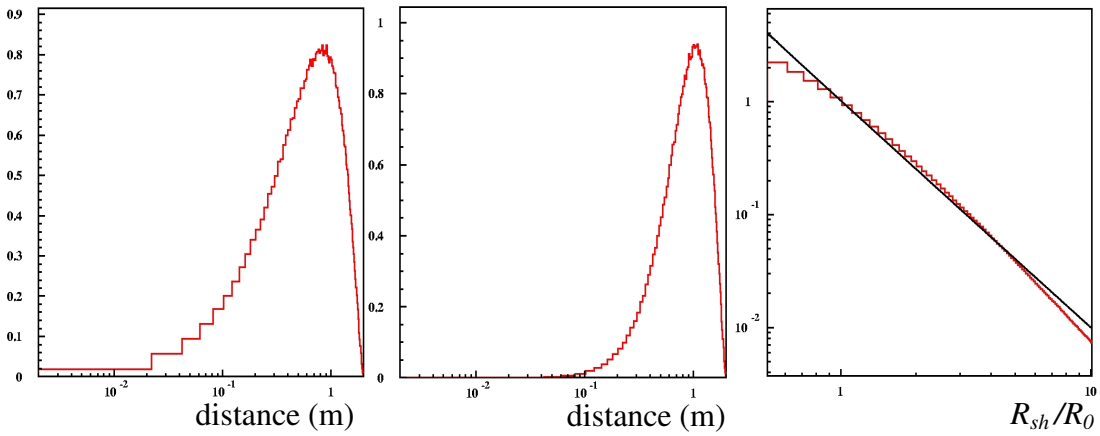

Figure 7.13 Left: distribution of the separation between two points on ground for a shower density distribution of the form $exp(-r)$; Middle: distribution of the separation between two points in the Cherenkov tank for a uniform density distribution; Right: dependence on R_{sh}/R_0 of the probability to detect a second muon from the same shower ($m=2$); the straight line is for $(m-1)(R_0/R_{sh})^2$.

8. Summary and conclusions

For now nine years, the Pierre Auger Collaboration, with which our laboratory, VATLY, is associated, has been operating a giant ground array of Cherenkov detectors covering 50×60 km^2 in the Argentinean Pampas [2, 12]. Its aim is the study of extragalactic Ultra High Energy Cosmic Rays, with energies in the 10^{20} eV range. It has already given first evidences for a cut-off of the energy spectrum [24] corresponding to the photoproduction threshold on the Cosmic Microwave Background (GZK cut-off) and for a positive, but weak, correlation with nearby galaxies – in particular Centaurus A – as potential sources [25].

As a contribution to the work of the Pierre Auger Collaboration, we have assembled on the roof of our Hanoi laboratory a replica of one of the 1'660 Cherenkov detectors of the Pierre Auger Observatory (PAO) with the aim of training and gaining familiarity with the tools and methods used at the PAO. Together with other equipment, including scintillator detectors and additional smaller Cherenkov detectors, it has given us an opportunity to explore some features of the cosmic ray flux in Hanoi where the rigidity cut-off reaches its world maximum of 17 GV.

The present work covers detailed studies that have been made of the performance of the VATLY Cherenkov detector with emphasis on its response to low signals. The detector is a water cylinder, 10 m^2 in area and 1.2 m in height, equipped with three down-looking 9" Photo Multiplier Tubes (PMT). In the PAO regime, where the detectors sample ~5 ppm of the PAO area, one deals with signal reaching 10^3 VEM (Figure 1.7), a VEM – Vertical Equivalent Muon – being the signal produced by a vertical relativistic muon impacting a detector in its centre. Here, we explore the response down to a tenth of a VEM, implying a dynamical range in excess of 10^4. Such a large dynamical range is important to obtain accurate measurements of the Lateral Distribution Function (LDF) and, consequently, of the shower energy. It is limited by saturation at high signal amplitudes, which is taken care of by recording the raw anode signal together

with the amplified dynode signal of each PMT. Its behaviour at low signal amplitudes is one of the main objectives of the present study.

The method that we have been using to study low amplitude signals is to look for decays of muons stopping in the water volume of the Cherenkov detector. Only a small fraction of cosmic muons, typically 6 to 7 %, do stop in there and of these, an even smaller fraction produces sufficient Cherenkov light to be detected before stopping (typically a quarter of a VEM). The subsequent muon decays occur on average some two microseconds afterward, producing an electron (or positron) and a neutrino-antineutrino pair that leaves the water volume undetected. The electron carries an average energy of only ~35 MeV, producing a signal of only a fraction of a VEM in ideal detecting conditions. Our experimental set-up has been designed to study such decays by detecting the signals produced by both the stopping muon and the decay electron. Such pairs have been detected under various experimental conditions and the amplitude of the electron signal has been recorded together with the time separating the two signals. Such data make it possible, using the different time dependences, to disentangle the contribution of muon decays from that of random muon coincidences.

In addition to the main Cherenkov detector, we have assembled a scintillator hodoscope that provides a trigger on central relativistic feed-through muons for calibration purpose and a scintillator detector used as a reference in which to observe muon decays in standard experimental conditions.

We have collected a large sample of data that provide very clear evidence for muon decays with the expected time dependence including a small contribution from muon capture in oxygen (Figure 6.5). The amplitude of the electron signal (Figures 6.17 and 7.11) is observed at the level of a fraction of VEM, and only the upper part of its distribution can be detected. The muon distribution (Figure 6.16 and 7.11) provides evidence for peaking at low amplitudes that cannot be explained as having a muonic origin. A detailed comparison with simulations has shown that it must be assigned to a soft component (Sections 7.2 and 7.3), known to be essentially made of electrons, positrons and photons, which appears particularly important in the present

experimental set-up due to the large sensitive volume of the Cherenkov detector. The possibility of a significant contamination by spurious sources prevents us from quoting a precise value for its rate. Good fits of the model to the measured data have been obtained for both the charge and time distributions (Figures 6.4, 6.14, 7.10 and 7.11). They allow for obtaining useful evaluations of the number of photoelectrons per VEM, 13.0±0.9, and of the mean muon energy, $4.0^{+0.4}_{-0.3}$ GeV. The detection efficiency of electrons has been modelled using an estimate of the effective electron shower size, ~36±6 cm, which is found at the scale of the radiation length in water as expected. The end point of the electron charge distribution, corresponding to a kinetic energy of 53 MeV, has been measured to be E_{end}=0.275±0.018 *VEM* in agreement with expectation. The occurrence of muon pairs from a same shower has been measured with a rate of 7.0±0.5 Hz, implying a decoherence function of the order of 30 m for a sea level multiplicity of two muons per shower.

The scintillator hodoscope has been successfully used to calibrate the Cherenkov detector and has given evidence for a resolution of 22.5% compared with ~15% for PAO detectors. The scintillator reference detectors have validated the interpretation of the Cherenkov data as expected and have provided an evaluation of the capture rate in carbon, $(1.2\pm0.6)\times10^{-2}$ μs^{-1}, in good agreement with expectation.

Simulations have been extensively used to compare our measurements with expectations and evaluate parameters of relevance. They turned out to be very useful to provide deeper insight into the mechanisms at play. Their results have been presented at various stages of the present study, including in particular Chapters 3 and 7. The measured event rates are found in good agreement with their predictions. Simulation has revealed the inadequacy of describing the effect of the discriminator thresholds on the sum Cherenkov signal by a sharp cut-off function and has allowed for a more faithful description. A simulation of the light collection mechanism has suggested the presence of a small zenith angle dependence of its efficiency, which has been found consistent with observation.

The availability of a replica of a PAO Cherenkov detector in our laboratory has proven to be useful not only for training purposes but also for

contributing a better understanding of the response of such a detector, in particular to low amplitude signals at the level of a fraction of a VEM. It will continue to be used as a training tool for students, not only at the scale of the VATLY team but at a broader scale.

References

[1]. P. Darriulat, Lectures on *Cosmic Rays, an Introduction*, Kathmandu 2010 and Ho Chi Minh City 2011, and references therein.

[2]. The Pierre Auger Collaboration, Contributions to the 32nd International Cosmic Ray Conference, Beijing 2011, and references therein.

[3]. D.K. The *et al.*, *Fluctuations in Diffusive Shock Acceleration*, Comm. Phys. Vietnam, Vol 21, Num 3 (2011) 199;

D.K. The, *Diffusive Shock Acceleration of Cosmic Rays,* Master thesis defended at Hanoi University of Education, 2010, and references therein.

[4]. K. Greisen, *End to the Cosmic-Ray Spectrum?*, Phys. Rev. Lett. 16 (1966) 748; G.T. Zatsepin and V.A. Kuzmin, *Upper limit of the spectrum of cosmic rays*, Pisma Zh. Eksp. Teor. Fiz. 4 (1966) 114.

[5]. P.N. Diep, *Contribution to the identification of primary ultra high energy cosmic rays using the Pierre Auger Observatory*, PhD thesis, 2010, and references therein.

[6]. D.T. Hoai *et al.*, *Simulation of proton-induced and iron extensive air showers at extreme energies,* Astropart. Phys. 36 (2012) 137-145, and references therein.

[7]. P.N. Dinh *et al.*, *Measurement of the vertical cosmic muon flux in a region of large rigidity cut-off*, Nucl. Phys. B627 (2002) 29-42.

[8]. P.N. Dinh *et al.*, *Measurement of the zenith angle distribution of the cosmic muon flux in Hanoi*, Nucl. Phys. B661 (2003)) 3-16.

[9]. P. N. Diep *et al.*, *Measurement of the east-west asymmetry of the cosmic muon flux in Hanoi*, Nucl. Phys. B 678 (2004) 3-15.

[10]. M. Honda et al., *Calculation of the Flux of Atmospheric Neutrinos*, Phys. Rev. D52 (1995) 4985 and Proc. 2001 Int. Cosmic Ray Conf., Copernicus Gesellschaft, Hamburg, p1162.

[11]. N.T. Thao, *The detection of extensive air showers in Hanoi,* Master thesis presented to the Hanoi University of Sciences, Vietnam National University, 2007.

[12]. The Auger Collaboration, *Properties and performance of the prototype instrument for the Pierre Auger Observatory*, Nucl. Instr. Meth. A523 (2004) 50 and references therein.

[13]. P.T.T. Nhung, *Performance studies of water Cherenkov counters,* Master thesis presented to the Hanoi University of Sciences, Vietnam National University, 2006.

[14]. P.N. Dông, *The Cherenkov counters of the VATLY Laboratory*, Master thesis presented to the Hanoi University of Technology, Vietnam National University, 2006.

[15]. X. Bertou, Proceedings of the 28th ICRC (Tsukuba), 2003;

X. Bertou, *Calibration of the surface array of the Pierre Auger Observatory*, NIMPRA 568, 2006, p839.

[16]. N.T. Thao, VATLY Internal note 30, *Design, installation and running-in of a muon trigger hodoscope bracketing the Cherenkov Auger tank of VATLY,* Jun, 2009.

[17]. P.T. Nhung and P. Billoir, *On the decay of muons stopping in the SD tanks*, Auger GAP2009-055;

P.T. Nhung, C*ontribution to the study of ultra high energy showers using the surface detector of the Pierre Auger Observatory*, PhD thesis presented at the Université Paris VI-UPMC, 2009.

[18]. The PDG Group, *Particle physics booklet*, 2008, p220.

[19]. D. F. Measday, *The Nuclear Physics of Muon Capture,* Phys/ Rep. 354 (2001) 243.

[20]. M. P. de Pascale et al., *Absolute spectrum and charge ratio of cosmic ray muons in the energy region from 0.2 GeV to 100 GeV from 600 m above sea level,* J. Geophys. Res., 98A3 (1993) 3501.

[21]. Y. Nishina, M. Takeuchi and T.Ichimiya, *On the Nature of Cosmic-Ray Particles*, Phys. Rev. 52 (1937) 1198.

[22]. For an early simpler version, see: D.T. The, *Optical properties of a Cherenkov counter,* Diploma in Astrophysics, Hanoi University of Education, Hanoi, May 2007.

[23]. K. Greisen, *Cosmic Ray Showers*, Ann. Rev. Nucl. Sci.10 (1960) 63.

[24]. J. Abraham *et al.* (Auger Collaboration), *Measurement of the energy spectrum of cosmic rays above 10^{18} eV using the Pierre Auger Observatory*, Physics Letters B 685 (2010) 239–246;

M. Settimo *et al.* (Auger Collaboration), *Measurement of the cosmic ray energy spectrum using hybrid events of the Pierre Auger Observatory*, Eur. Phys. J. Plus 127 (2012) 87.

[25]. J. Abraham *et al.* (Auger Collaboration), *A search for anisotropy in the arrival directions of ultra high energy cosmic rays recorded at the Pierre Auger Observatory,* JCAP 04 (2012) 040;

J. Abraham *et al.* (Auger Collaboration), *Constraints on the origin of cosmic rays above 10^{18} eV from large scale anisotropy searches in data of the Pierre Auger observatory*, ApJL, 762 (2012) L13.